BIOINSPIRED MECHANICAL DEVICE GENERATES PLASMA IN WATER VIA CAVITATION

A Dissertation

by

XIN TANG

Submitted to the Office of Graduate and Professional Studies of
Texas A&M University
in partial fulfillment of the requirements for the degree of

DOCTOR OF PHILOSOPHY

Chair of Committee,	David Staack
Committee Members,	Yassin A. Hassan
	Kentaro Hara
	Astrid Layton
	Richard Miles
Head of Department,	Andreas A. Polycarpou

August 2020

Major Subject: Mechanical Engineering

ABSTRACT

Laboratory and industrial plasmas in liquid are conventionally generated by electric fields. In nature, one verified plasma generation method is the hydrodynamic flow induced cavitation by snapping shrimp. Collapsing cavitation is an effective energy focusing process to generate high-temperature and high-pressure energy states inside the cavitation, indicating of plasmas formation. The shrimp's method of plasma generation has potential to be a high efficient technique due to the species evolution. Therefore a bioinspired mechanical device mimicking snapping shrimp snapper claw was designed to explore the possibility of producing plasma mechanically.

Due to the complex fluid flow during the shrimp snapping process, a morphologically accurate claw is essential for hydrodynamic flow induced cavitation. Based on micro X-ray computed tomography (μ-CT) of a shrimp claw molt, a device was designed with torsion springs to actuate the snap. The major parts of the bioinspired device inherited claw morphology were only rendered feasible using additive manufacturing. Spring fixtures were designed to reliably actuate the claw with appropriate force and velocity to produce a high-speed water jet for inducing the cavitation. Different parameters such as torsion spring constants and releasing angles are explored to search for suitable parameters for larger cavitation size. And the underwater shock wave propagation and light emission during the cavitation collapse were recorded with an intensified charge-coupled device (ICCD) camera. The images of the luminescing cavitation at their first

singularities were the direct proof of the “shrimpoluminescence” phenomenon which is similar to the sonoluminescence.

Light emission evidences were verified in argon or air doped distilled water and saline water doped with air (the shrimp living condition), demonstrating the mechanical device can reproduce the plasma generation technique of the shrimp. The scale of the plasma ranges from 10 μm to 242 μm, and the time duration detected by the photomultiplier tube is ~15 ns. For this type of thermal plasmas, the plasma generation efficiency is directly coupled with the cavitation conversion efficiency. After comparing to other cavitation generation techniques, the cavitation conversion efficiency of the bioinspired mechanical device is ~3-2000 times more efficient. In order to characterize the plasma, a customized optical system is established for spectroscopy analysis. With the blackbody radiation assumption, the estimated plasma temperature was around 12,000 K for argon doped distilled water. Based on scaling laws such as matching the cavitation number, the 5 times scale-up device can operate in different liquids and a 25 times scale-up device was designed and generated cavitation in water successfully under different pressures to show the cavitation behavior difference.

For future work, an automatic snapping shrimp robot can be used for plasma characterization and other practical applications. More distilled design can be explored with the aid of simulation. Additionally, hydrodynamics instabilities for jet-induced cavitation collapse could also lead to new research directions.

ACKNOWLEDGEMENTS

I would like to thank my mentor and advisor, Dr. David Staack, who provided invaluable advices and discussions on this challenging multi-disciplinary research topic and his continuous support and guidance through my PhD program. His encyclopedic knowledge, passion for high quality research, work ethic, and work-life balance has been a constant source of inspiration for me. I am also very grateful to my committee members, Dr. Kentaro Hara, Dr. Yassin Hassan, Dr. Astrid Layton, and Dr. Richard Miles, for their guidance and support throughout the course of this research. Beyond the scope of this research, I really appreciate the discussion of future career development with Dr. Hara and his continuing support.

The five years research and work experience at Plasma Engineering and Non-equilibrium Laboratory is a lifetime treasure that I truly enjoyed. Special thanks to my colleagues for their generous help and fruitful discussions related to this dissertation research: Kunpeng Wang, Matthew Burnette, John Lasselle, Chris Campbell, Nicolas Gawloski, and Peng Xiao. It is a great pleasure to work with my other lab mates on plasma research though not related to the scope of this dissertation, they are William Pollard, Abismael Diaz, Harika Damarla, Josef Sebastian, Jacob Mallams, Min Huang, Mirza Riyaz, Ruilian Gao and other members in Plasma Lab. I also want to thank undergraduate students Benjamin Swain, Cameron Adkins, Tyler Barnes, Dylan Baldwin, and REU student Gaurav Aggarwal for their assistance and help on conducting experiments.

Most importantly, I want to express my deep appreciation to my family, my mother and father for their unconditional love and encouragement. I feel grateful to my fiancée, the love of my life. Her love, support and patience during my long time PhD grinding means a lot to me.

CONTRIBUTORS AND FUNDING SOURCES

Contributors

This work was supervised by a dissertation committee consisting of Professor David Staack of the Department of Mechanical Engineering, Professor Astrid Layton of the Department of Mechanical Engineering, Professor Yassin Hassan of the Department of Nuclear Engineering, Professor Richard Miles and Professor Kentaro Hara of the Department of Aerospace Engineering.

All work conducted for the dissertation was completed independently by the student.

Funding Sources

Graduate study was supported by Graduate Assistantships from J. Mike Walker ‘66 Department of Mechanical Engineering, Texas A&M University.

This work was made possible in part by National Science Foundation under Grant Number PHY-1057175, Robertson-Finley Foundation, and Graduate Summer Research Grant from Department of Mechanical Engineering.

TABLE OF CONTENTS

Page

LIST OF FIGURES

Page

LIST OF TABLES

Page

1. INTRODUCTION

> Plasma, the Greek verb πλάσσειν means: to form, to mould, to shape. The noun πλάσμα means figure, shape, effigy.
>
> --- Alexander Piel (*1*)

1.1. Background

This section will focus on a brief background introduction on plasmas and how to generate plasma mechanically to place the motivation of this research.

1.1.1. Plasmas

The term ‘plasmas’ in physics refer to the “fourth state of matter”, the other three states are solid, liquid, and gas. Plasma is an ionized gas consists of electrons and ions with collective behavior. It is generated by adding energy to a neutral gas, which separates electrons from gas atoms or molecules. Irving Langmuir (*2*) introduced this word 90 years ago describing the charge-neutral or quasi-neutral part of a gas discharge. The way the ‘equilibrium’ part of the discharge carrying particles reminded him of the way blood plasma carries around red and white corpuscles and germs.

Plasmas can be categorized into two major types, thermal plasmas and non-thermal plasmas (*3*). Thermal plasmas are thermodynamic equilibrium systems with temperatures over 10,000 K (1 eV = 11,605 K). On the contrary, the non-thermal types are in a

thermodynamic and chemical non-equilibrium with the temperature of the electrons (>10,000 K) greatly in excess of the gas temperature (~300 K).

The plasmas generated by inertia compression via collapsing cavitations are the focus of this research. It is quite an interesting question whether these plasmas are thermal or non-thermal and whether these plasmas have reached local thermodynamic equilibrium (LTE) or not since their duration are at the time scale of nanoseconds. It is certain that the plasma generated is an inertially confined plasma in an imploding bubble or collapsing cavitation (*4*) and the particle densities (n~10^{22} cm^{-3}) and high temperatures (T~10,000 K) at bubble collapse create a high energy density states in which collisions between particles are very frequent, and the collision times are way below a picosecond according to Brenner et al (*5*). Therefore, the plasmas inside the cavitation during singularity are highly probable in the state of local thermodynamic equilibrium.

1.1.2. Mechanically generated plasmas

Laboratory plasmas are generated by electric discharges (*6*). However, there are plasmas in nature which are generated mechanically by energy focusing method such as the snapping shrimp which can shoot out flashing bubbles (*7*). The snap shut of a snapping shrimp's giant claw can induce cavitation by shooting out high speed water jet out from the claw socket, forming cavitation bubbles. The collapsing cavitation is an effective energy focusing method which can compress the gas mixture inside the cavitation to reach high temperatures and high pressures at minimum volumes (singularities) during its

collapsing behavior. It forms high energy density states at singularities with shock waves and photon emission, indicating of plasma generation.

This cavitation luminescence phenomenon has been studied for decades, however, the temperatures and pressures inside the cavitation at singularities still remains unclear due to no appropriate non-intrusive methods for temperature and pressure measurement. Another issue is that the spectrum of the light emission generated in cavitation luminescence is sensitive to the dissolved gases, and the air dissolved in snapping shrimp living conditions resulted a limited number of photon emission induced by the shrimp's cavitation. The dim light which cannot be detected by human eyes is the major challenge for the temperature measurement of the shrimp cavitation luminescence.

1.2. Dissertation Statement

This dissertation details a project that focuses on generating plasma in water mechanically via cavitation. To be more specific, this dissertation states that "bioinspired mechanical device can generate plasma via collapsing cavitation." The demonstrative approach of this engineering thesis includes a bioinspired mechanical device design mimicking snapping shrimp, cavitation luminescence of the shrimp-inspired device indicating of plasma generation, and plasma temperatures measurement using the spectrum recorded at cavitation luminescence.

The present study has three parts: the first is bioinspired design of a mechanical device to generate large cavitation bubbles with hydrodynamic flow in the form of high-speed water jet and the cavitation-induced shock waves and plasma formation in the form

of light emission; and second is the temperature measurement of these kind of plasmas utilizing optical emission spectroscopy; the third is exploring bioinspired device operation in other liquids and further scaled-up device. For the purpose of this dissertation, more emphasis is placed on the first part and the second part due to there is no similar device for plasma generation has been reported before and the plasma characteristics like the plasma temperatures are essential for potential applications.

1.3. Motivation

This research was performed under the support by a NSF grant "Micro- and Nano-Scale Plasma Discharge in High Density Fluids" and was also patronized by donation from the Robertson-Finley Foundation on high pressure plasma research. This study has two main aspects with regard to general motivations and impact, the first aspect is to design a plasma source which can generate plasma in water mechanically via energy focusing, and the second is the investigation of the microscale plasma characteristics.

As mentioned in the previous text, laboratory plasmas are usually generated by electric discharges. The single bubble sonoluminescence (SBSL) research in the last two decades provided proofs (*4*, *8*, *9*) of plasma formation inside the core of sonoluminescing bubbles even though the first report of cavitation luminescence in the form of Multi-bubble sonoluminescence (MBSL) phenomenon dated back to the 1930s. Similar to SBSL, the snapping shrimp can shoot out flashing bubbles with a much larger maximum radius up to 3.6 mm (*10*) compared to the SBSL case which ranged from 50~80 μm (*11*). The major difference is the shrimp induces the cavitation with hydrodynamic flow instead of

ultrasonic sound as in the sonoluminescence. With the order of magnitude estimation, the volume compression ratio for SBSL and the snapping shrimp are both at the order of 10^5, which indicates the potential plasma generation in the shrimp induced cavitation. Due to the evolutionary pressure, shrimp's cavitation generation method is a high efficient technique on converting mechanical energy which induces the snapper claw snap shut into cavitation bubble mechanical energy. And the plasma formation in collapsing cavitation bubble is directly related to the cavitation conversion efficiency. Thus, the shrimp plasma generation method could be a high efficient technique for these kind of plasmas. With the bioinspired engineering design mimicking the snapping shrimp, the same method of cavitation generation technique can result in a synthetic mechanical device as a plasma source which inherits the shrimp's potential of high efficiency. Another important part is that the bioinspired device facilitates repetitive and consistent experiments on collapsing cavitation processes and plasma formation. With the bioinspired mechanical device, we can accumulate authoritative evidence of mechanically generated plasma in cavitation luminescence and, in the meantime, learn more about the snapping shrimp, energy focusing, and underwater plasmas.

The characteristics of the plasma generated with the bioinspired mechanical device is vital for future applications. The high temperatures and high pressures at cavitation singularities could lead to a large scope of potential applications like water treatment, rock disintegration, biomedical application, material synthesis (nanoparticles and other kinematically-stable and thermodynamically-unstable materials), and liquid hydrocarbon cracking. With modification of the bioinspired device which enables the automatic

snapping process in a higher frequency compared to the living shrimp, the shrimp-inspired plasma source can be easily scaled up in numbers forming large batch of plasma reactors for different industrial applications.

1.4. Dissertation Overview

Chapter 1 introduces the topic and explain the motivations of this research. Chapter 2 covers introductory information and background of plasma knowledge, cavitation luminescence, and a little bit of bioinspired engineering design.

Start from Chapter 3, research related results are presented. From Chapter 3 to Chapter 6, these are largely from published journal article (*12*) as part of the research. Chapter 7 and Chapter 8 are partly from conference presentations and manuscripts are prepared for submission to journals. Chapter 3 addresses the details of the bioinspired design and the guiding principles. Chapter 4 and 5 focus on the cavitation bubble dynamics, underwater shock waves, and light emissions, which is a proof of plasma generation based on the similarities related to other cavitation luminescence methods. The parametric study of the shrimp-inspired device under water in Chapter 4 provides key parameters to fulfill the design purpose and reveal the shrimp cavitation generation mechanism to a new level. Chapter 5 presented the world's first direct recorded 'photos' of the shrimp generated cavitation luminescence phenomenon and discusses the stochastic behavior of the light emission intensities resulted from non-spherical collapses, hydrodynamic instabilities and turbulence. The cavitation conversion efficiency for different methods are discussed in Chapter 6 for this type of local thermodynamic

equilibrium. This efficiency is not plasma generation efficiency, however, it is directly related to the plasma generation process and coupled with the plasma generation efficiency via energy focusing. In Chapter 7 spectroscopic technique is employed to probe the temperature inside the luminescing cavitation and at the same time pushes the limit of optical emission spectroscopy to the challenge of dim light. In Chapter 8, the further scale-up design is explored to extend the parameter space of scaling laws in bioinspired design, covering experimental examples under ambient pressure and lower pressure of the 25 times large claw.

Each chapters focuses on a self-contained aspect of the research, experimental setup, and conclusions to each experiment are given along with the results. A paragraph at the beginning of each chapter summarizes each aspect of the research gives context to the results presented within the framework of the dissertation.

2. LITERATURE REVIEW

If I have seen a little further it is by standing on the shoulders of Giants.

--- Isaac Newton

2.1. Summary

This chapter introduces plasmas, cavitation luminescence, bioinspired engineering design, and summarizes some prior research in the fields of plasmas generation via collapsing cavitation, a typical energy focusing process.

2.2. Introduction to Plasmas

Plasma, known as the fourth state of matter, is ionized gas consist of a large number of electrons and ionized atoms and molecules, in addition to neutral atoms and molecules as are presented in a normal (non-ionized) gas. Those electrons and ions make plasma conduct electricity. Generally speaking, solid material can become liquid phase with the addition of energy, and liquid will transfer to gas in the same manner. If sufficient energy is added to a gas, the atoms and molecules of the gas may become ionized, forming charged particles such as free electrons, negative and positive ions which respond to external electric and magnetic fields. The Coulomb force of the charged particles interaction is a long-range force, decaying slowly as r^{-2}. Therefore, plasma show a simultaneous response of many particles to an external stimulus, demonstrating a *collective behavior*. This is the distinctive difference between plasma and a neutral gas.

2.2.1. A Brief History

Most of the Universe is in a plasma state, including stars, galaxies, and nebula etc. On our home earth plasmas generation need special processes and require specific conditions. We human beings live in our atmosphere on earth where neutral gas in the midst of an otherwise ionized environment, examples of partially ionized gases or plasmas, including lightning, fire, and the aurora (polar light) have long been part of our natural environment. The early natural philosophers, at least dates back to Empedocles (c. 490-430 BC), thought the Universe is built of four classical elements or 'roots' like: Earth, Water, Wind and Fire (a weakly ionized plasma), curiously resembling the modern terminology of solid, liquid, gas, and plasma states of matter. One of the most common transient plasmas exist in the Earth's atmosphere is lightning, which has been striking the Earth long before the human existence, and may even have played a vital role in the origin of life on our planet as demonstrated in the famous Miller-Urey experiment (*13*).

Plasma physics was deeply rooted with the history of electricity (*1*, *14*). Otto von Guericke (1602-1686) generated electricity successfully with a sulfur globe, and observed the corona discharge at sharp and pointy geometry part of electrodes. Ewald Georg von Kleist (1700-1748) and Pieter van Musschenbrock (1692-1686) invented a high-voltage capacitor independently which was called the Leyden jar. When a charged Leyden jar produces a spark discharge in air, the noise sounds like a gun shot, from which the terminology gas discharge arose. With the development of high-current electric batteries, the electric arc was discovered by Vasily V. Petrov (1761-1834) in 1803 and

independently by Humphrey Davy (1778-1829). In 1831, Michael Faraday discovered electric glow discharges in noble gases and made systematic investigations during the following years. In 1857, Werner von Siemens patented his ozonizer, which is the first technological use of plasma. Nicola Tesla (1856-1943) started his research on electric discharges driven by high frequency electric and magnetic fields in 1891.

With series of important discoveries on gas discharges before 1900s, the nascent idea involving the motion of free electrons and positive ions with gas discharges emerged. The text book "Electricity in Gases" published in 1902 by Johannes Starks is considered to be the first account of gas discharge physics. The modern concept of a plasma with the collective behavior in gas discharges started in the 20^{th} century. The advancement of atomic physics around the turn of the 20^{th} century progressed together with gas discharge physics. During the 1920s, two groups of scientist, Irving Langmuir who was the first describing gas discharge phenomenon as "plasma", and his co-workers as well as Walter Schottky conducted systematic investigations of the plasma state and the formulation of general laws. After 1950s, plasma research has been established on controlled nuclear fusion and space plasma physics.

Today plasmas are widely used in a large scope of industries. The trillion-dollar semiconductor industry employs plasma enhanced chemical vapor deposition (PECVD) and plasma etching processing in the integrated circuit (IC) manufacturing. Due to the luminescence nature of plasma, plasma is also used in lighting industry, decorating modern life with lamps, fluorescent tubes and noble gas filled bulbs, and plasma TVs. Thermal plasmas with temperature over 10,000 K are used to melt rocks in drilling process,

melt metals in refining and welding applications. Low temperature plasmas like coronas and dielectric barrier discharges (DBD) are also widely used in ozonizer, medical treatment, waste water treatment (killing germs and breaking the strong artificial C-F bond in C8, like the infamous Perfluorooctanoic acid, as known as PFAS), surface property modification, sterilization, carbon dioxide reduction, and even the newly developed additive manufacturing (3D printing) applications. Transient pulsed plasma discharges (streamers) are playing a major role in electronics and concrete recycling, rock disintegration in drilling and mining, ore pre-treatment, and ice cracking. In addition to the aforementioned industrial applications, controlled nuclear fusion, astrophysical research, space propulsion, and some environmental related plasma research are the most significant university and governmental research funded areas.

2.2.2. Definition of a Plasma State

According to Saha equation which describes the ionization state of a gas in thermal equilibrium as a function of temperature, pressure and ionization energy, all gases have some small fraction of ionized particles and free electrons to certain degree. However, not all gases are plasmas. The distinctive difference between neutral gas and a plasma is the collective behavior. The collective behavior is called the plasma approximation and is legitimate when the number of charged particles within the sphere of influence of a specific particle is large.

This sphere of influence radius is known as the Debye length (or Debye shielding length), a measure of the distance over which the mobile charge carriers (free electrons

and ions) screen out electric fields in plasmas. Similarly, Debye length concept is also used in electrolytes and colloids describing how far the charge carrier's electrostatic effect persists. In plasma physics, Debye length is defined as

$$\lambda_d = \sqrt{\frac{\varepsilon_o k T_e}{n_e e^2}}, \tag{1}$$

where ε_o is the vacuum permittivity, k is the Boltzmann constant, T_e and n_e are the electron temperature and electron number density, and e is elementary charge. The average number of particles in the Debye sphere (Debye volume) is predicted by the plasma parameter, $\Lambda = 4\pi n_e \lambda_d^3 = 3N_d$, where $N_d = \frac{4}{3}\pi\lambda_d^3 n_e$ is a more frequent and appropriate definition of plasma parameter which is also termed as Debye Number. Due to only a factor of three difference, these two definitions are generally used interchangeably.

In order to be qualified as a plasma state, the Debye length need to be smaller than the plasma characteristic size, and the number of charged particles in a Debye sphere should be sufficient, which obeys the condition $\Lambda \gg 1$. When $\Lambda \ll 1$, the plasma is a Strongly Coupled Plasma (SCP). Additionally, the plasma can be considered *quasineutral* on length scales larger than the Debye length. In other words, the plasma is charge neutral overall, while at smaller scales below Debye length, the positive and negative charges of the plasma may be interfered by charged regions and electric fields. The formula representing *quasineutrality* on length scales larger than the Debye length is defined below

$$\left|\sum_j Z_j e n_{i,j} - n_e e\right| \ll n_e e. \tag{2}$$

Here the left hand side includes all (positive) ion species j of charge number Z_j. For a single positive ion species of charge number $Z = 1$, the criteria can be simplified to $n_i = n_e$.

2.2.3. The Saha Equation

For a gas at a sufficient high temperature or density, the thermal collisions of the atoms will ionize some fraction of the gas. The Saha equation depicts the degree of ionization for any gas in thermal equilibrium as a function of the temperature, number density and ionization energies of the atoms. For a gas consists of a single atomic species, the Saha equation is in the following form

$$\frac{n_{i+1} n_e}{n_i} = \frac{g_e G_{i+1}}{\lambda_{th}^3 G_i} \exp\left[-\frac{(\epsilon_{i+1} - \epsilon_i)}{T}\right], \tag{3}$$

in which n_i and n_{i+1} are the number density of atoms in the ionization state i and the ionization state $i + 1$ of a given atom species, g_e is the degeneracy of the free electrons (electrons have two distinguishable spin states, $g_e = 2$), G_i is the degeneracy of states for the i state ions, $\lambda_{th} = \sqrt{h^2/(2\pi m_e T)}$ is the thermal de Brogile wavelength of an electron, h is the Planck constant, ϵ_i is the energy required to remove electrons from a neutral atom, creating i level ion, and T is the temperature of the gas.

In order to further understand the ionization degree predicted by Saha equation, we can take a look at the stellar hydrogen. For hydrogen, $G_0 = 2$ since the ground state

statistical weight is a good approximation, $G_1 = 1$ because the protons has no bond electrons in the ionized state. Assuming stellar hydrogen as ideal gas with pressure $P \approx$ 20 Pa, and the hydrogen ionization energy is 13.6 eV, the number densities of ions, electrons, and the neutral gas atoms are expressed as $n_i = n_e = n - n_0$, where n is total number density of all species, subscript i, e, 0 refer to ions, electrons and neutrals (atoms or molecules). Thus the ionization degree of stellar hydrogen can be estimated with the following equation

$$\frac{\alpha^2}{1-\alpha} = \frac{2kT}{P}\frac{G_1}{G_0}\left(\frac{2\pi m_e kT}{h^2}\right)^{3/2} exp\left(-\frac{E_i}{kT}\right). \quad (4)$$

Assuming ideal gas, pressure $P = nkT$, the ionization degree or excitation fraction $\alpha = n_i/n = n_e/n$ for stellar hydrogen with varying gas temperature is demonstrated in Figure 1. At temperature around 9,200 K, 50% ionization is achieved, while at approximately 12,500 K, 99% of hydrogen atoms are ionized for this stellar hydrogen example case.

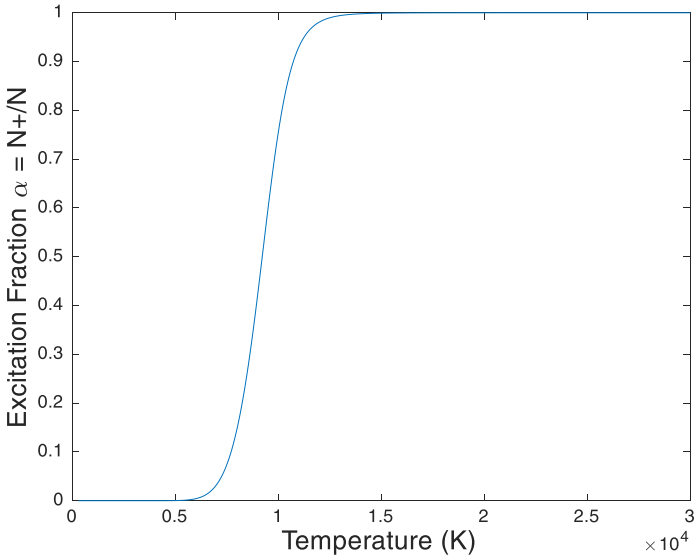

Figure 1 Saha equation excitation fraction for stellar hydrogen at $P \approx 20$ Pa

According to the supplementary material of Bradt's book (*15*), in the photosphere of the sun, the mass density is $\sim 3 \times 10^{-4}$ kg/m^3 which results in proton number density $\sim 2 \times 10^{23}$ m^{-3}. As demonstrated in Figure 2, for T = 6400 K, the degree of ionization (ionization fraction) is $n_{r+1}/n_r = 4 \times 10^{-4}$, which indicates that the photosphere is mostly neutral. Generally speaking, these temperatures for reaching an ionized state are much less than the ball park estimate just based on hydrogen ionization energy 13.6 eV, which is T = 13.6* 11605 K = 157,828 K. In most astrophysics low pressure condition, the temperature required for ionization of dilute gases is relatively low. Figure 2 demonstrates a wide range of total number densities range from n = 10^5 m^{-3} (about the average number density of visible matter in the universe) to 10^{25} m^{-3} (when the physical spacing between the atoms begins to approach the size of the atoms). In the center of the sun, the number density is ~ 10^{32} m^{-3}, the spacing is smaller than the scale of the ground-state orbital of the electron. The electrons can no longer be associated with the given atom and the Saha equation is not valid any more.

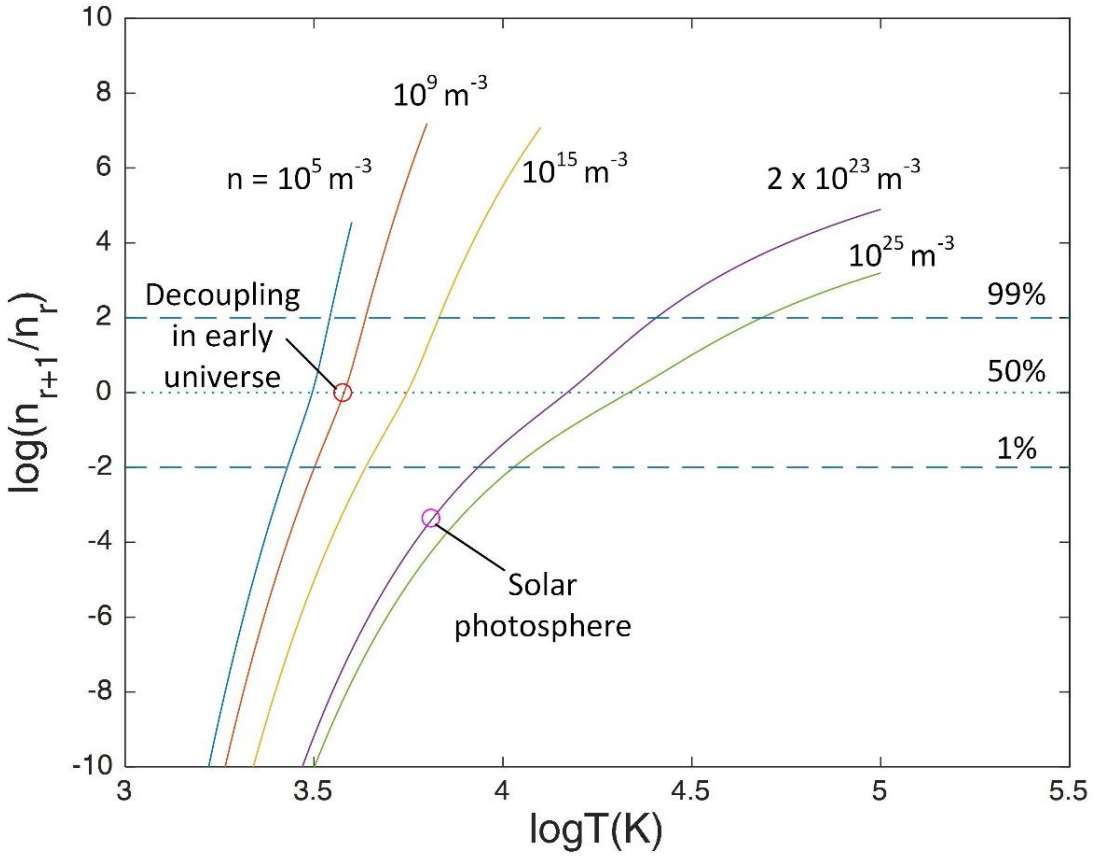

Figure 2 Log scale ionization fraction n_{r+1}/n_r for various fixed total number densities, $n = n_{r+1} + n_r$ as a function of temperature (*15*)

The Saha equation can also shed light on the state of ionization of hydrogen in the early phase of the universe. Physical models suggest that when the expanding universe cools, the hydrogen plasma recombines to neutral hydrogen, making it transparent to photons. At this time, the density is $n \approx 10^9$ m^{-3}. When the curve of this number density reaches 50% degree of ionization, the corresponding temperature is ~ 4000 K. Therefore the hydrogen becomes neutral under this temperature. The relatively low intensity photons can no longer ionize the hydrogen so they are free to travel around the universe. The

microwave background radiation of the universe is consist of those photons, which have cooled from 4000 K to 3 K due to the expansion of the universe (*15*).

2.2.4. Plasma in Nature

Over 99% of the visible Universe consists of plasmas, however, there are fewer we can see on earth. The two most common plasmas in nature are lightning and aurora. Lightning is a high-current electric transient discharge (arc discharge) in air, releasing most of its energy in pulses at time scales of microsecond to millisecond. It is formed due to collisions of different moving clouds in troposphere with charge accumulation until the electric potential reaches sufficient level to cause the air to breakdown, inducing a lightning bolt. This discharge may produce a wide range of electromagnetic radiation, from thermal plasma generated by the rapid moving electrons to flashes of visible light in the form of blackbody radiation. A typical lightning bolt carries current peaked at 10,000 amperes and has peak temperature in exceeding of 50,000 K. Different from the lightning, the auroras take place at the upper atmosphere (thermosphere/exosphere). Auroras are the result of disturbances in the magnetosphere caused by solar wind. They are generated by charged particles with kinetic energy ranged from 0.5 eV to 10 keV in the solar wind which are directed by the Earth's magnetic field to the polar area where they collide with atoms and molecules in the Earth's upper atmosphere with a typical temperature around 3,000 K. These two natural phenomena are two typical examples of thermal (lightning) and non-thermal (aurora) plasma.

Asides from the two common plasma discharges, marine animals like the snapping shrimp can shoot out flashing bubbles which emits light and shock waves. The collapsing cavitation, a form of energy focusing, is the snapping shrimp's lethal weapon for hunting. Due to the millisecond time scale of the cavitation duration and dim light emission, this cavitation luminescence example was only revealed by scientist two decades ago. Similar to one single cycle of SBSL but with larger maximum bubble volume, the collapsing cavitation light emission indicates an inertia confined plasma formation just like the SBSL. Using the similar energy focusing technique, mantis shrimp and Thresher shark are also potential candidates which can generate plasma under the sea.

2.2.5. Plasma in Laboratory

Laboratory plasmas are usually generated by externally applied electric fields, acoustic device with oscillating bubbles, high power lasers, and microwave. Due to the high temperature requirement (over 10,000 K) for generating thermal plasmas is very impractical and only generate equilibrium plasmas, another alternative approach is using electric fields.

The basic example is DC plasma generated between two parallel plates with applied electric field as illustrated in Figure 3. This approach is based on the already existed ionized particles and free electrons which is only consisted of a tiny fraction in all gases, either due to thermal equilibrium excitation (Saha equation) or induced by cosmic rays, those electrons are called primary electrons. In the applied electric field, an electron will gain kinetic energy much easier during acceleration in electric field due to its smaller

mass compared to ion particle. Owing to the dense gas during travel, the accelerated electron will collide with a particle when moving towards the plate with positive polarity. When the electron has sufficient energy it will ionize the atom or molecule producing a positive ion and another electron. These two electrons are then accelerated again and ionize more particles. If the multiplication of electron as an electron source is larger than losses, the plasma density will geometrically increases, this process is called the electron avalanche.

The increase in electron density during avalanche growth is defined as $dn_e/dx = \alpha n_e$, after integration we have $n_e(x) = n_{e0}\exp(\alpha x)$. Here x is the distance and α is the first Townsend coefficient or the gas multiplication factor. Electrical discharges which rely on preexisting electrons are termed alpha mode discharge or Townsend discharge, it is named after the first Townsend coefficient. This coefficient can be interpreted as the probability of an ionization event per unit path length of an electron. The energy gained between collisions is $\varepsilon = \lambda_e \mathrm{E} = \mathrm{E}/(\sqrt{2}\sigma \mathrm{n})$, where λ_e is the mean free path of the electron and n is the number density of the gas between the plates. One can see the energy gained between collisions is proportional to the reduced electric field $\varepsilon \sim E/n$, the reduced electric field is an important parameter in gas discharge physics and many scaling laws. For ideal gas, pressure can be written in $p = nkT$, thus another form of E/p is also popular in plasma textbooks. The condition for using this form of reduced electric field is the temperature, which is assumed to be room temperature. Therefore, the temperature variation need to be included based on equation of state.

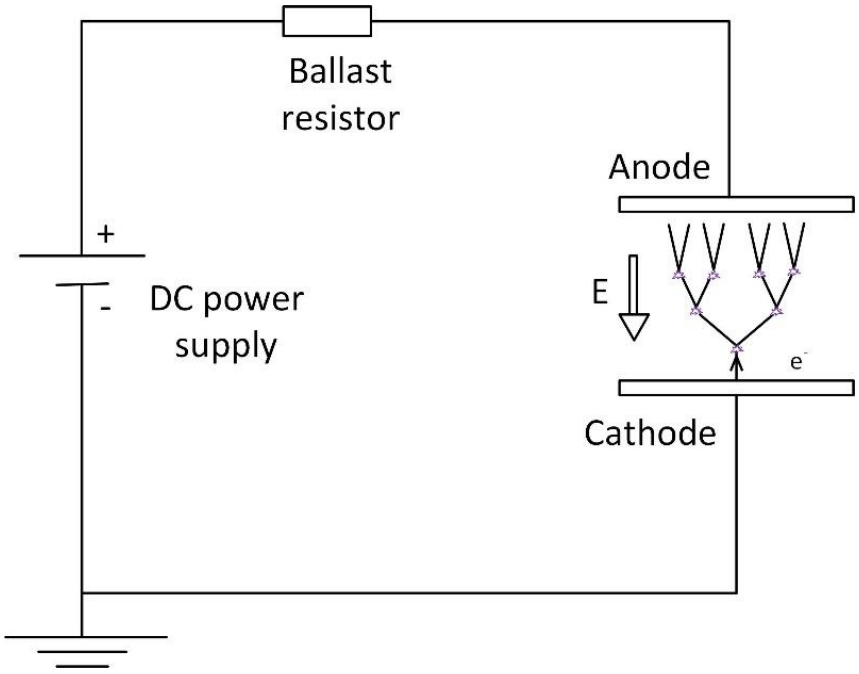

Figure 3 Electron avalanche in an applied electric field between two parallel plates

The probability to release an electron from the cathode by ion impact is represented by a coefficient γ, which is defined as the ratio of emitted electron flux to incoming ion flux. In practice, this coefficient describes the sum of secondary electron emission (SEE) by ions, metastable atoms, and the photon emission by UV radiation in the cathode fall. SEE is not a very probable process typically about 1 in 1000 ions produce one secondary electron. Generally there are three mechanisms by which the discharge can generate electron and become self-sustained, the first is SEE, the second is thermionic emission (TE), and the third is field emission (FE). TE occurs when the electrode become sufficiently hot that electrons are thermally liberated from the surface. TE is a function of the electrode temperature and the work function of the electrode material. FE requires very high electric field (E ~ 10^{10} V/m) to "push" electron off the electrode surface. Discharges

sustained by SEE are termed gamma mode discharge. γ is a function of the electrode material, ion energy, and is weakly dependent on the surface temperature. Electrical breakdown is interpreted as the transition of a medium from poor electric conductor to a good electric conductor. Electric breakdown of gas occurs when the avalanche process can maintain itself, the condition is given by the Townsend formula

$$i = \frac{i_0 e^{\alpha d}}{1 - \gamma(e^{\alpha d} - 1)}, \tag{5}$$

where i is the total current in the discharge and i_0 is the current of primary electrons. When the avalanche become self-sustained, the balance equation fulfills, which is $\gamma(e^{\alpha d} - 1) = 1$. This can be described Townsend used an empirical law for the dependence of α on the electric field,

$$\frac{\alpha}{p} = Aexp\left(-\frac{B}{E/p}\right), \tag{6}$$

where constants A and B are characteristic for each gas. The reduced field required for breakdown can be interpreted as a function of similarity parameter pd (d is the discharge gap length). This parameter is proportional to ratio of the discharge gap to the mean free path or the inverse of Knudsen number ($Kn = \lambda_{mfp}/L$, where L is the physical length scale). When we plot the breakdown voltage vs. pd, the Paschen curve is obtained.

$$V_B = \frac{Bpd}{\ln(Apd) - \ln[\ln(1 + \frac{1}{\gamma})]}. \tag{7}$$

Different gas Paschen curves with coefficient γ = 0.01 are demonstrated in Figure 4. For specific gas, there is a minimum breakdown voltage on its Paschen curve. To the left of the minimum breakdown voltage, the discharge gap is so small that there is no sufficient

number of mean free paths in the discharge gap to trigger a discharge. To the right side, the required breakdown voltage is higher since the electrode gap is larger, although the required E/p is lower.

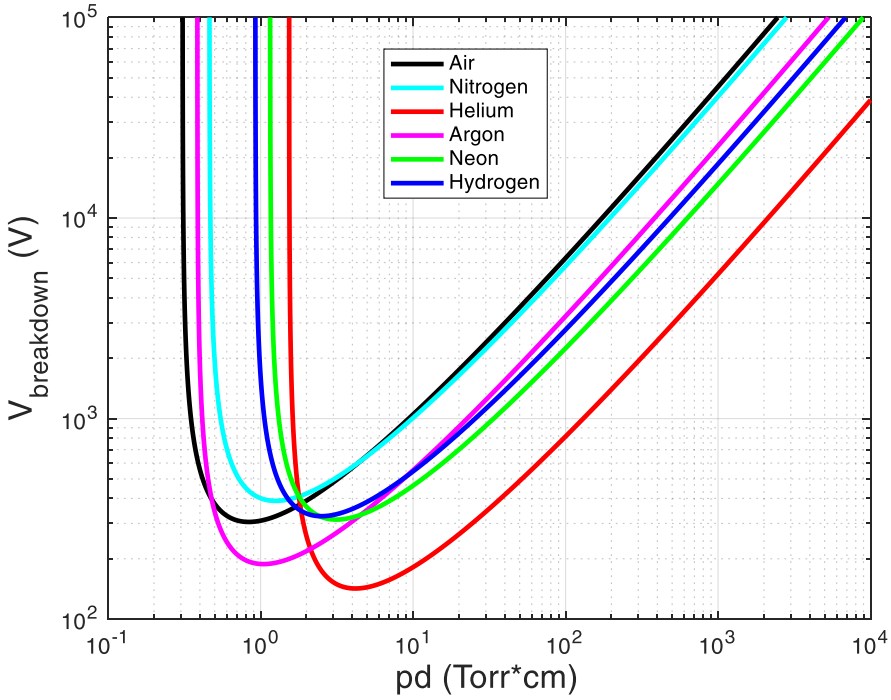

Figure 4 Typical Paschen curves: Breakdown voltage in different gases for $\gamma = 0.01$ as a function of the product pd.

In practice, there are physical limitations for the electric breakdown, such as the power supply which can only provide a finite current. The current in the breakdown is either limited by the power supply or electric circuit in conjunction with the power supply. One way to overcome this is making the power supply pulsed at certain frequency. Other methods to limit the current is using dielectric barriers on the electrode as dielectric barrier discharges (DBD).

2.2.5.1. Low-pressure discharge

Glow discharge: This gamma mode glow discharge is formed by the passage of electric current (DC or AC) through a low pressure gas. This is probably the most common plasma we can see in daily life, such as the plasma in the fluorescent tubes and neon lights. It is widely employed in lighting industry and material processing and manufacturing in semiconductor industry.

Capacitively coupled plasma (CCP): this type of plasma between (typically) parallel plane electrodes is driven by a single radio-frequency (RF) electric fields, typically 13.56 MHz. The electrodes may be in contact with the discharge, or they may be insulated from it by solid dielectrics (*6*). These high frequency discharges operate continuously in alpha mode. These are widely used in semiconductor industry and plasma enhanced chemical vapor deposition.

Inductively coupled plasma (ICP): a type of plasma source in which the energy is supplied by electric currents which are produced by electromagnetic induction (time varying magnetic fields). ICP discharges have relatively high electron density, on the order of 10^{15} cm^{-3}. ICP discharges are widely used in situations where a high-density plasma (HDP) is needed. For example, ICP can be seen in scientific instruments such as atomic emission spectroscopy and mass spectrometry, the other important application is reactive-ion etching in integrated circuits (IC) manufacturing in conjunction with CCP.

Wave heated plasma: similar to CCP and ICP, it is typically RF (or microwave), however, it is heated by both electrostatic and electromagnetic means. For example, the helicon discharge and electron cyclotron resonance are all wave heated plasma.

2.2.5.2. Atmospheric pressure discharges

Arc discharge: arc is a high current thermal discharge at temperature in exceeds of~10,000 K. It is commonly used in metallurgical processes and plasma welding. For example, it is used to melt rocks containing Al_2O_3 to produce aluminum, or melt granite for drilling in hard rocks.

Corona discharge: this is a non-equilibrium plasma discharge formed by imposing high voltage to sharp electrode geometry. The sharp tip generates an electric field sufficient for breakdown only in the vicinity of the tip. Coronas discharges are widely used in ozone generators and particle precipitators.

Dielectric barrier discharge: this is a non-thermal plasma transient discharge generated by the application of high voltages across small gaps where a dielectric coatings or dielectric layer keeps the plasma discharge from transferring into a self-sustained glow or arc. Breakdown occurs in the form of streamers and charges accumulate on the electrodes during the discharge. It is often interpreted wrongly as ‘corona’ discharge in the industry and has similar applications to corona discharges. The application of the discharge to synthetic fabrics and plastics functionalizes the surface and allows for paints, glues, and

similar material to adhere. Potential applications of DBD in our lab includes water treatment, 3D printing layer binding, space laundry (DBD treatment of the clothes of astronauts), and electroporation on plant cells (to delivery drugs or modify genes with CRISPR).

Novel atmospheric pressure discharge: Some of our lab plasmas operated at ambient pressure which do not have industrial application yet. For example, 3D printing of PMMA or copper layers on pig skin using the atmospheric pressure plasma jet (PECVD), and nano-second dielectric barrier discharges. Spark discharge in crude oil with different gases for upgrading oil. E-beam treated medical plastic for sterilization, oil contaminated soil remediation, PFAS removal in water, etc.

2.2.5.3. High pressure plasma

Cavitation luminescence: it is an inertially confined plasma inside a collapsing cavitation bubble. The temperatures (typically ranges from 6000 K to 20,000 K) of the plasma depend on a lot of ingredients: gas mixture contents, liquid solutions, liquid temperature and pressure, and acoustical driving pressure of ultrasonic waves for sonoluminescence. It can be used for water treatment, medical device for disintegrating kidney stones, material processing, etc.

Spark discharge in high pressure liquids: this type of plasma use pulsed streamer such as spark discharge to initiate shock waves on the surface of solid materials immersed in

liquids. Those pulsed plasma breakdown in solids are termed electrodynamic or internal electric breakdown inside solid dielectrics. Other pulsed spark discharges in liquids are termed electrohydraulic process. The strong shock waves generated in liquids or plastic waves in solids can be used for recycling, drilling, and demolition.

2.2.6. Energy transfer in plasmas

For equilibrium plasma or thermal plasma, the Saha equation, as discussed in section 2.2.3, depicts the energy transfer pathways from heat to ionization. In general all of the species of the plasma are in thermal equilibrium having the same value for all characteristic temperatures and energy are equally partitioned among the internal energy levels.

For non-equilibrium plasmas, the energy is not equally partitioned between the various kinetic and microstates or internal degree of freedom of the system. Typical non-equilibrium plasmas are characterized by their effective electron kinetic temperature (T_e), and neutral gas electronic excitation temperature (T_{elex}), vibrational temperature (T_{vib}), rotational temperature (T_{rot}) and translational temperature (T_{trans}). In non-thermal plasmas created by externally applied electric fields typically there are $T_e > T_{elex} > T_{vib} > T_{rot} = T_{trans}$. This is a direct demonstration that energy is not equally distributed among the various internal degree of freedom and kinetic energies of the system. Another important reason is the mobility difference between electron and ion due to their mass difference ($m_{proton} = 1836.15 m_e$). The mobility of particles μ are defined below

$$\mu = \frac{q}{m\upsilon_m}, \tag{8}$$

where q is the electric charge of the particle, m is the mass of the particle, and υ_m is the momentum transfer collision frequency.

It is due to the applied electric field that the non-equilibrium nature of the non-thermal plasma is maintained. The electric energy imposed on the system is only applied to the electrons and ions instead of all particles. In Figure 5, the energy pathway illustrating the flow of energy in a plasma sustained by an electric field is demonstrated. This flow diagram describes the relative rates of these energy flows and reverse energy flows among different internal energy modes and the overall summation of them determine whether the non-equilibrium can be maintained.

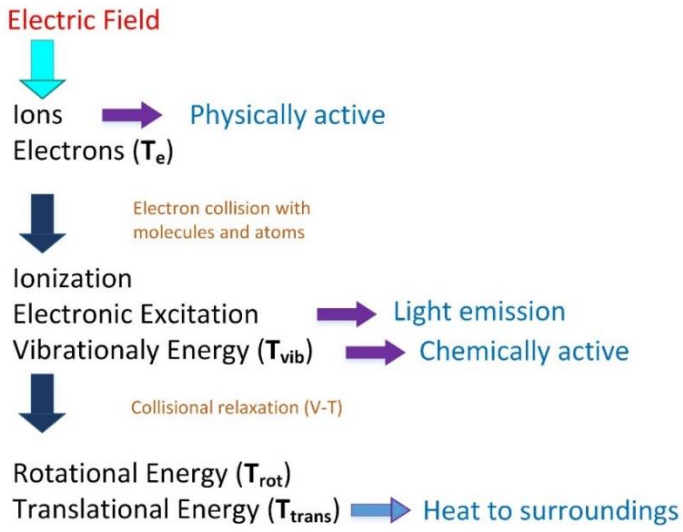

Figure 5 Energy flow diagram for non-thermal plasmas.

The electric field only directly couple with charged particles such as ions and electrons in the form of Lorentz Force, $F = qE$, where F is the force on the particle, q is

the charge, and E is the local electric field. Due to the enormous mass difference between electrons and ions, the majority of energy is directed to the electrons. The electrons in turn collide with the neutral molecules and atoms. Various type of collisions occur to direct the flow of energy transfer, for example in molecules: momentum transfer, rotational excitation, vibrational excitation, electronic excitation, dissociation, and attachment. Whereas for atoms, they do not have internal degrees of freedom so they do not experience rotational excitation, vibrational excitation, or dissociation. The prominent parameter in the energy transfer process is E/n. For typical range of electric fields of 0.1 to 1 times the breakdown E/n, each type of the electron collision is discussed below.

Momentum transfer: The momentum transfer is a very inefficiency energy transfer process. Due to the large disparity in mass between electron and heavy neutral particles, very little momentum and energy can be transferred. This process is mainly for scattering the electrons thermalizing their energies.

Ionization (10-20 eV): It is a very important process for generating plasma, but not a significant method of energy transfer. There is only small fraction of high energy electrons participate in the ionization process.

Electronic excitation (5-15 eV): Electronic excitation is responsible for light emission from plasma discharges and also stepwise ionization process. It is very important for spectral analysis and understanding the light emitted by the discharge. The plasma temperature measurement techniques or pyrometers are based on the spectroscopic analysis.

Vibrational excitation (0.5-4 eV): In molecular gases the main energy transfer pathway from electron to neutral atom occurs through vibrational excitation. Compared to the momentum transfer, the vibrational energy transfer is less probable. However, vibrational excitation can be resonant and results into a significant amount of energy transfer. Typically about 80% of the energy may flow from the electrons to vibrational excitation. Vibrational modes relax through chemical process (i.e. stepwise dissociation, or lowering of activation energies in endothermic reactions) or through collisions with neutral particles, leading to effective vibrational-translational (V-T) energy transfer. Vibrational relaxation is a fundamental process via which non-equilibrium states thermalize.

Rotational excitation (10^{-4} eV): Rotational excitation is an insignificant portion of the energy flow as the characteristic energy of rotational modes is only about 5 K and therefore will not transfer significant energy per collision.

Dissociation (2-10 eV): The amount of dissociation caused by electron impact collision depends on the bond strength of the molecule. For example, nitrogen has a dissociation energy of 9.756 eV, and it only experience a small degree of dissociation.

Attachment: It is not significant for energy transfer, however, attachment is very essential for charge balance, ionization rates and charge mobility.

2.2.7. Plasma in Liquids

For plasma generation in liquids and plasma liquid interactions, there are a huge number of publications out there. Here, we introduce some comprehensive literature review papers to lay fundamental background introduction to this field. These are

introduced by the different plasma generation methods in liquid: electric discharges, laser-induced plasma, sonoluminescence, and hydrodynamic flow induced luminescence. Some of the laser-induced plasma, sonoluminescence, and hydrodynamic flow induced luminescence are discussed in more detail in the cavitation luminescence section.

The 2012 plasma road map (*16*) listed the state-of-art plasma in and in contact with liquids and also pointed out the challenges. For electric discharges in liquids, the main focus was on glow discharge electrolysis and breakdown of dielectric liquids for high voltage pulsed discharge. The glow discharge electrolysis part and the plasma liquid interactions was thoroughly introduced by Bruggeman et al. (*17*).

The breakdown of dielectric liquids with high voltage switching includes spark discharges (streamers) with more than one electrodes and corona type discharges with single electrodes and liquid itself as grounding. Electric pulse technology has been utilized in a variety of industrial applications like drilling, recycling, and demolition for decades. The methods of electric pulsed technologies are electrohydraulic (*18*) in liquids, electrodynamic or internal electric breakdown inside solid dielectrics (*19*), plasma blasting or the use of dielectric material surface flashover (*20*), and electric explosion of wires on the surface of a dielectric (*21*).

Laser-induced plasma inside liquids contains two types of plasma generation mechanisms, the first is the laser induced breakdown (LIB) in liquid and the second is the luminescence generated during the collapsing bubbles near their first singularities. For details of LIB, one recent comprehensive review by Lazic and Jovićević (*22*) is a good guidance to the field. And research on the second type plasma, laser-induced cavitation

luminescence, is relatively new and corresponding literature is reviewed in later section as a subtopic of cavitation luminescence.

Sonoluminescence generates inertially confined plasma (*4*) inside imploding single bubble or multi-bubbles driven by ultrasonic sound field. This research branch has a significant overlap on the topic of this dissertation, and thus detailed reviews are carried out in the later section.

2.3. Introduction to Cavitation Luminescence

2.3.1. What is Cavitation?

Cavitation is a vapor phase formation process of a liquid due to reduction of pressures at constant ambient temperature. It is a boiling process in a liquid because of the pressure reduction instead of heat addition. For hydrodynamic flows, the cavitation occurs when the static pressure is lower than the liquid vapor pressure, where liquid vaporizes into gas and generates a cavitation. Due to the inertia of the cavitation bubble, the radius continues increasing past the liquid vapor pressure, so that the collapse occurs within a few microseconds, followed by a number of rebounds. There several theories describing the cavitation collapse and the resulted light emission, the two most possible theories are the imploding shock theory and the “hot spot” theory.

At the collapsing process of a standalone cavitation, as demonstrated in Figure 6, the interface or the wall of the cavitation collapse rapidly, whose wall velocity exceeds the local speed of sound, generates focused shock waves propagating inwards, creating a high-pressure and high-temperature inside the cavitation gas core. The high-pressure and

high-temperature gas at the minimum volume of the collapsing cavitation, usually termed as singularity, reaches high energy density states which are intense enough to generate reactive species, increase chemical reactivity, melt metal particles, and emit light in certain conditions. After the pressure and temperature burst in a short time scale, the cavitation will rebound outwards followed with expanding shock waves. This is the simple explanation of the imploding shock or microshock theory.

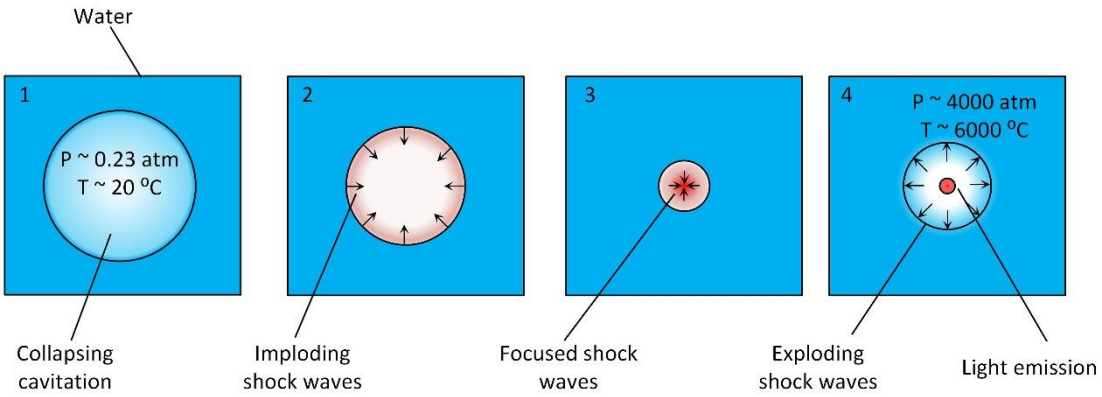

Figure 6 Spherical collapsing cavitation heat up in stages described by the imploding shock or microshock theory

On the other hand, the cavitation wall velocity may not in exceed of the local speed of sound during cavitation collapse due to the increasing temperature and density alongside with the collapsing cavitation. The energy for the light emission is supplied by thermal energy resulting from an adiabatic or polytropic compression, this is the thermal molecular-emission or “hot spot” theory, demonstrated in Figure 7, which is so far the most probable one for explaining the phenomenon of cavitation luminescence.

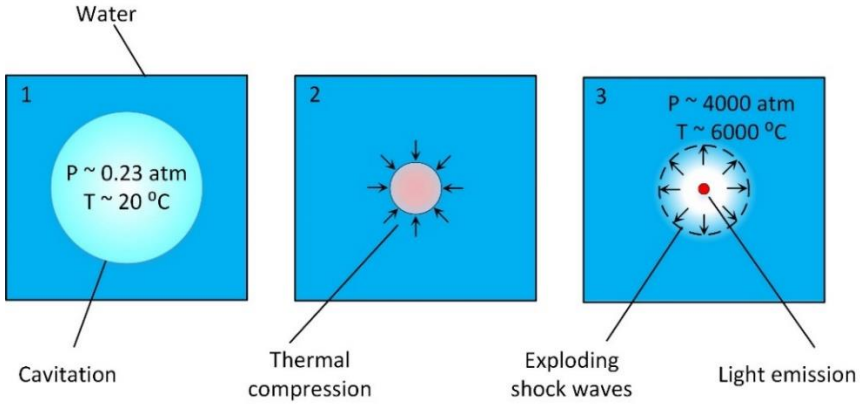

Figure 7 Spherical collapsing cavitation described by the "hot spot" theory with thermal compression

Cavitation was first reported as a contribution to the corrosion of metal propeller blades in the late 19th century (*23*). The first mathematical model analysis of this form of cavitation collapse was given by Lord Rayleigh in 1917 (*24*). Rayleigh considered the ideal case of a spherical bubble collapse limited solely by the inertia of the liquid, which resulted in infinite wall velocity and pressure near the wall at the end of the collapse. In reality, the presence of a finite mass of gas and uncondensed vapor inside the cavitation halts the collapse as the pressure within the cavitation bubble increases. The extreme conditions of high pressure and high temperature within the cavitation singularity verified with experimental observations that the collapse of cavitation bubbles is accompanied by chemical reactions, shock waves, and light emission.

2.3.2. Energy Focusing

An energy focusing (or energy concentration) process can focus the diffuse energy (sound field, flow field, electric charge, laser light) by many orders of magnitude. The

cavitation collapsing process is a typical example of energy focusing, in which the energy of collapse or the bubble mechanical energy is delivered to a small number of molecules. Flow energy injected at low energy densities forms cavitation bubbles whose subsequent collapse focuses the gas mixture energy inside the cavitation by many orders of magnitude.

The phenomenon of SL involves an extraordinary degree of energy focusing (*25*). According to Barber's paper, the energy density of the sound field with a pressure swing of ~ 1 atm is 17.3 $\mathrm{erg/cm^3}$ (1.076*10^{-10} eV per atom). As a blue photon has an energy of ~ 3 eV, the SL phenomenon involves an energy focusing or amplification of about 10 orders of magnitude. For hydrodynamic flow in water at ambient pressure of 1 atm, the velocity when cavitation occurs is approximately $v \approx \sqrt{2\rho(P_\infty - P_v)} = 14.08$ m/s, and the energy density of the flow field is ~6.17*10^{-6} eV per atom, this hydrodynamic cavitation collapsing involves an energy focusing of about 5 orders of magnitude with the same standard.

2.3.3. Hydrodynamic flow induced cavitation luminescence

Hydrodynamic flow induced cavitation is the most fundamental cavitation generation method. According to Bernoulli's principal in basic fluid dynamics, pressure decreases as a function of increasing speed. It was Leonhard Euler who derived Bernoulli's equation in its general form in 1752 (*26*). Assuming no change in the elevation of a point in a liquid, for example in water, the total pressure is constant at low Mach number $P_{total} = P_{static} + P_{dynamic} = p + 1/2\rho v^2$. If the fluid flow velocity increases high enough, causing the static pressure drop down below the vapor pressure of water in

this case, there will be a cavitation generated at this point. Simply put, sufficient high speed flow (~14 m/s near water surface at room temperature and pressure) will induce cavitation.

Looking back to the literature, there was a unique report of luminescence in the high-speed flow around an obstacle by Kostantinov and Akad in 1947, however, some experiments of the author with a highly sensitive photomultiplier tube (PMT) failed to detect any significant luminous emission from similar blade and tip vortex cavitation (*27*).

Luminescence by hydrodynamic cavitation was then identified in 1964 by Jarman and Taylor in a Venturi tube experiment (*28*). In 1967, Peterson and Anderson (*29*) investigated the characteristics of light emission from hydrodynamic cavitation in a Venturi tube with small variation of water temperature, pressure and gas content. It was eventually discovered that the addition of a small quantity of xenon gas to the liquid being cavitated by flow, enabled the luminescence from the cavitation bubbles to be detected much easier. The intensity of cavitation luminescence appeared to have a very strong dependence on the dissolved gases in the liquid. Later in 1999, Weninger et al. (*30*) reported the air-saturated water produced luminescence in Venturi experiments was approximately 100 times weaker than water saturated with 50 Torr Argon and at least 5000 times weaker than 50 Torr xenon. For single flashes detected with a PMT from seeded (0.3 mm radius) bubble upstream from the constriction part xenon were 1.5 times larger than krypton, and 200 times larger than argon, and no light flashes observed for helium bubble. In the same series of experiments, temperature was found to play an

important role in agreement with MBSL results, cavitation luminescence strongly decreasing with increasing temperature.

For examples of hydrodynamic induced cavitation in nature, in the year 2000, Versluis et al. (*10*) unveiled how snapping shrimp produce the noisy snap sound, through cavitating bubbles induced by high-speed water jet shoot from the snapper claw socket. And then in a letter to Nature published in 2001, Lohse et al. (*7*) presented direct light emission evidence from the snapping shrimp cavitation bubble collapsing, this interesting cavitation luminescence phenomenon was named "shrimpoluminescence". These research in Dr. Lohse group demonstrated a verified case of cavitation luminescence in nature.

The flow over a hydrofoil within a cavitation tunnel can also generate cavitation luminescence. van der Meulen conducted a few studies (*31*, *32*) of this phenomenon inside a high-speed flow tunnel with a NACA 16-022 hydrofoil set at various angles. In all his studies, no luminescence was detected from 'undoped' water, however, with the addition of xenon, the luminescence was detectable by the unaided eye. He claimed those research results established some link between erosion, noise generation, and luminescence. The details of van der Meulen's studies were summarized in the paper by Leighton et al. (*33*). Leighton et al. made the first attempt to obtain information on the absolute intensity, and temporal properties of the cavitation luminescence from flow over a hydrofoil in the École Polytechnique Fédérale de Lausanne (EPFL) high-speed cavitation tunnel using a NACA 009 blade. Farhat et al. (*34*) investigated the cavitation luminescence at the same facility with intensified charge coupled device (ICCD) video camera and a PMT. Over long time scales, the analysis of bursts of light emitted at the Strouhal frequency (the shedding of

transient cavities), which reflect global hydrodynamic behavior. Due to the contradiction of the imploding jet formation near solid surface and dramatic reduction of energy focusing within the cavitation bubble at the same time, the relationship between the luminescence with cavitation erosion was hard to determine, as erosion was caused by the bubble collapse near the surface of hydrofoil. The complexity of hydrodynamic cavitation make it hard to probe the individual cavitation event. However, this did propose a need of hydrodynamic induced standalone cavitation for future research.

Water hammer phenomenon with light emission is also a type of hydrodynamic induced cavitation luminescence. When the motion of a liquid in a pipe is abruptly forced to stop or change of direction (sudden momentum change), for example by a sudden closing of a valve, a pressure pulse propagates through the liquid. The Joukowsky pressure, which depicts the maximum pressure of the shock generated by the water hammer (~10 MPa), is defined as $P_J = \rho c v$, where ρ and c are the density and speed of sound of the fluid respectively, v is the fluid velocity. The shock wave is generally accompanied with collapsing cavitation that emits a more intense shock wave (*35*, *36*). A cavitation luminescence from water hammer was first noticed by Schmit (*37*) in 1959 when he conducted water hammer tube experiment with glycerin, he reported the observation of light emission in weak red color without any further investigation. In 2003, Su et al. (*38*) from Dr. Putterman's group investigated the sub-nanosecond light flashes from collapsing cavitations inside a water hammer tube. There were over 10^8 photons observed in a single collapsing event with a peak flash power greater than 0.4 W. The spectrum recorded was broadband similar to other cavitation luminescence cases. The next year, Chakaravarty et

al. demonstrated stable cavitation light emission in various fluids within a rotating water hammer tube. By applying a rotation platform to confine bubbles to the axis of the tube, the reproducibility of the phenomenon was improved significantly. With the xenon bubble in phosphoric acid, they find the brightest luminescence (six order of magnitude higher compared to water with xenon) in all the experimental conditions, and there were discrete emission lines of 825 nm, 895 nm, and 940 nm were spotted with a diffraction grating.

In 2012, Khalid et al. (*39*) conducted experiments on interaction between a nanosecond pulsed laser (3 ns, 532 nm) and a 70 μm radius luminescing cavitation bubble plasma (induced by rotating water hammer device). The images of the interaction reveal that light energy is absorbed and trapped in a region smaller than the luminescing region of the bubble for over 100 ns. They interpreted this opacity and transport measurement as a demonstration of the luminescing bubbles can be 1000 times more opaque than what the Saha equation predicted in the ideal plasma limit. The dehydrated phosphoric acid and xenon gas were mixed with 20 torr overhead pressure in their water hammer tube. If the opacity and emissivity of SL systems is resulted from the high levels of ionization degree then a complete theory must include Coulomb interactions, indicating that there was a strongly coupled plasma (non-ideal plasma) generated during the cavitation luminescence induced by the rotating water hammer device.

2.3.4. Sonoluminescence

Sonoluminescence, abbreviated as SL, is defined as the emission of short bursts of light from oscillating bubbles induced by imposed sound field in a liquid. It is a sonically

induced cavitation luminescence phenomenon. There are two major types of sonoluminescence: Single Bubble Sonoluminescence (SBSL) and Multibubble Sonoluminescence (MBSL). Due to the fact that there are a huge number of scientific research publications in this field and several comprehensive reviews (*5*, *40–42*) of SL already covered the whole scope of this field, only certain major papers are discussed and reviewed in this section.

2.3.4.1. Multibubble Sonoluminescence (MBSL)

Initially, the SL studies focused on MBSL formed by sound field imposed with ultrasonic device at frequency from 20 kHz to 2 MHz. According to the review by Suslick and Flannigan (*42*), the first indirect observation of such phenomenon was in 1933 by Marinesco and Trillat. The first direct observed sonically induced luminescence was recorded by Frenzel and Schultes in 1934 (*43*), and is then generally termed sonoluminescence. It was discovered after exposing photographic plates for several hours to water with cavitations generated by piezoelectric quartz crystals.

The review by Jarman (*27*) in 1960 summarized the early publications on MBSL in aqueous solutions and proposed the imploding shock theory of SL: the collapsing cavitation induces imploding shock wave that compresses and heats the gas mixture inside the bubble to high-temperature and high-pressure states. He linked the converging shock induced argon luminescence experiments in a shock tube by Perry and Kantrowitz (*44*) with the microshocks occurred within the cavitation during the final stage of cavitation bubble collapse. The spectral analysis of MBSL in aqueous solutions consisted mainly of

a broadband and featureless continuum spectrum stretching across the visible region (*45*). The chemical reaction of water vapor inside such as the disassociation of water molecules was verified by the observation of hydroxyl radical (OH*) emission bands. Alongside with the spectroscopic analysis, correlational studies were also carried out on MBSL as summarized by Young in 1976 (*46*). Those studies explored light emission intensity with various external parameters such as properties of the imposed ultrasonic field, gas dissolved into the liquid (i.e. thermal conductivity), and bulk liquid temperature. The results of these studies revealed that the SL was depend on the thermodynamic properties of gas mixture inside the cavitation, indicating that the light emission was caused by thermodynamic compressional heating of the gas mixture content (*42*). Quantify the conditions inside the collapsing cavitation during SL was also the major goal of researchers, the first studies attempted to quantify the conditions inside conditions by assuming SL as blackbody radiation was summarized by Walton and Reynolds (*47*). In aqueous solvent used in these MBSL experiments, water vapor inside the cavitation increased heat capacity of gas mixture due to the extra water molecules and their dissociation. Since water molecule has more internal degrees of freedom such as vibrational modes and rotational modes than inert gases, the degeneracy in the vibrational and rotational states is lifted which results in many allowed transitions (vibrational modes to electronica excitation modes or ionization). This result in almost featureless spectra with little or no discernable structure.

Nonaqueous solvent Suslick and Flint (*48*) reported the spectral analysis of MBSL observed in 1987, revealing the “spectral richness” not observable in aqueous solution SL

experiments. Later in 1989, Flint and Suslick (*49*) claimed the bands and lines in organic solvents revealed a lot of information on the mechanism: (a) the principal source of MBSL was not blackbody radiation, instead, it was a form of chemiluminescence since the high-energy species formed during cavitation collapse; (b) the transient temperature inside the cavitation during SL determined the rate of chemical reactions; (c) the chemistry highly depended on the contents of the gas mixture inside the cavitation. Retrospectively, it is a sign of potential plasma generation inside the collapsing cavitation. Observation of discrete and easily identified emission lines and bands provided methods for quantitative analysis of the SL from the relative intensities of vibrational spectra and atomic bands (*50*, *51*). Analysis of peak shift and broadening of atomic emission lines established an effective method to estimate the pressures and number densities during collapsing cavitation with SL (*52*). The determination of cavitation parameters such as bubble radius, driving pressure, intracavity temperatures and pressures during MBSL was difficult due to the fact that a collapsing bubble behavior always affected by neighboring bubbles. Scientists had to describe the cavitation systems in terms of ensemble average quantities. A stable single cavitation bubble would be better to explore those unknowns.

Conditions (Temperature, Pressure) during MBSL

There are two major temperature measurement methods for MBSL, kinetic measurement and spectroscopic measurement. The sonication of a composition-known liquid, analysis of the chemical products, and rate constants for specific kinetic reactions can be employed to estimate temperature through the Arrhenius relation. Suslick et al. (*53*)

utilized comparative rate thermometry to estimate the temperature based on the intensity of different emission lines. There were two major sites of sonochemical reactions were found in their experiments: gas-phase site and liquid-phase site between which the gas-phase site was the majority. The effective temperature of the gas-phase zone was 5200 $\pm$ 650 K, and the liquid phase was ~1900 K. These results suggested that the role of the cavitation interface is minimal relative to micro-jet agreed with SBSL experimental evidence (*54*) and previous numerical simulations (*55*). Other kinetic studies employed the methyl radical recombination method, the estimated effective temperature range was 2000 to 5000 K (*56*, *57*).

The other type of temperature measurement method is the spectroscopic method. With the comparison of the relative intensities of emission lines from electronically excited atoms and molecules, an effective emission temperature can be deduced. This is the so-called plasma thermometry technique quantifying the characteristic temperatures of plasmas and flames based on the internal distribution of energy levels on temperature for thermally equilibrated systems.

The intensity of an emission line occurring from relaxation of an electronically excited atom is expressed by

$$I_{nm} = \frac{hc}{4\pi} l N_0 \frac{g_n}{Q} \frac{A_{nm}}{\lambda_n} exp\left(-\frac{E_n}{kT}\right), \quad (9)$$

where n stands for the upper state or excited energy state, and m represents the lower energy state or ground state, h is the Planck's constant, c is the speed of light, k is the Boltzmann constant, l is the path length of the confining region, N_0 is the atom number

density, g_n is the degeneracy of the upper state n, Q is the partition function $\sum_n g_n \exp(-E_n/kT)$, A_{nm} is the Einstein coefficient or Einstein transition probability between states n and m, E_n is the energy of the excited state n, and T is the absolute temperature of gas. Technically, temperatures can be deduced by comparing the calculated calibration curves (I_{nm} vs. T) and experimental spectral measurements of absolute line intensity for a specific transition. Besides the requirement of absolute intensity measurement, this method of effective temperature determination is also limited by the species studied. For specific emission lines there is a temperature threshold, over which the radiance of the line will not increase because of the ionization induced counteracting of the population of the excited state. Theoretically, there is a the temperature limit of approximately 16,000 K for the 415.8 nm emission line in argon atomic emission spectrum (*58*).

There is a simpler method called two-line radiance ratio method, in which the atom number density and the path length is not required. The only required parameter need to know is the relative Einstein transition probabilities or the relative Einstein coefficients. This is the advantage of two-line method since only ~20% of the absolute Einstein coefficients are known. In order to apply this method, the system should follow a Maxwell-Boltzmann distribution. Plasma temperature can be estimated by comparing the relative radiance intensity of two or more states via fitting the data. Several other methods also utilize this principle, for example the iso-intensity method and the atomic and molecular Boltzmann plots. Applying the two-line method, the ratio of the intensities of two emission lines (I_1 and I_2) is

$$\frac{I_1}{I_2} = \frac{g_1 A_1 \lambda_2}{g_2 A_2 \lambda_1} exp\left(\frac{E_2 - E_1}{kT}\right). \quad (10)$$

If those constants in the equation for specific atom are known, then the absolute temperature can be determined by comparing the relative intensities of transitions from different excited states. If the two emission lines utilized are originated from a neutral atom, the measured emission temperature reflects the atomic excitation temperature.

With the aforementioned two-line spectroscopic method, Kenneth Suslick and his group (*50*, *51*, *59*, *60*) conducted the MBSL temperature measurements, the typical maximum effective temperature in MBSL ranges from ~3000 K to 6000 K, depending on experimental parameters.

For acoustic driven cavitation, the collapsing process not only making the cavitation reach high temperature but also high pressures. The extreme pressures inside the 'flashing' cavitation during MBSL can also be determined based on relative intensity of emission lines from electronically excited atoms (*52*). However, the peak shifts is needed rather than relative intensities. Various factors can contribute to changes in line positions and shapes, such as Doppler effects, pressure broadening, Stark effects and ion broadening, and instrument contributions (slit function). There are two major sources of peak position shifts and line broadening, one is perturbations of the internal energy levels of radiating species and the other is reductions in the excited-state lifetimes owing to an increase in the collisional frequency with other species (*61–63*).

In 2003, McNamara et al. (*52*) measured the high pressures inside the cavitation bubbles during MBSL by estimating the peak shifts in the emission lines from Cr* for SL of helium or argon in silicone oil containing $Cr(CO)_6$. However, due to the intrinsic

characteristics of MBSL, the interference from neighboring bubbles contributed up to 50% to the line width via scattering. The peak shifts and the scattering effects of the bubble cloud are independent of each other. Compared to Cr* emission lines in literature with extra calibration and extrapolation to temperature observed during cavitation, the pressure lower limit was 300 ± 30 bar.

2.3.4.2. Single Bubble Sonoluminescence (SBSL)

At the beginning of 1990s, a second type SL was widely reported (*25*, *64*) to generate and stabilize a single acoustically driven cavitation bubble with light emission. This type of SL is most suitable for experimental measurement since it is a single gas bubble trapped at the antinode of a standing wave. In SBSL, the cavitation bubble can be tuned so that the light bursts are generated with a clocklike synchronicity. Similar to MBSL, the SBSL spectra in aqueous solutions were broadband featureless (*25*, *40*, *65*, *66*), and the emission spectra from aprotic organic liquids (*67*), concentrated mineral acids (*68*) contained discrete emission lines and bands, allowing the experimental quantification of temperatures and pressures.

The first thorough investigation of SBSL was conducted in 1989 by Dr. Felipe Gaitan at University of Mississippi working with Professor Larry Crum. Based on Crum's previous SL experience from a single bubble in 1985 (*69*), Gaitan searched for the stable SBSL systematically as his objective of his thesis (*70*). In his search, he found a regime that the sound field was reducing the number of oscillating bubbles, resulting into only one single bubble remained. With Mie scattering tracking the seeding bubble with neutral

radius R_0 ~5 μm, the cavitation collapsed from maximum radius R_{max} ~50 μm to a minimum radius R_{min} ~0.5 μm, indicating a volume compression ratio by 6 order of magnitude. The bubble expansion induced by the negative pressure of sound field was followed subsequently by a strong collapsing behavior, during which light is emitted.

In the 1991 Nature paper, Barber and Putterman (*25*) measured the light pulse using PMT, concluded that the duration of the pulse was less than 50 ps. Hiller et al. (*65*) measured the spectrum a SL air bubble in water and demonstrated that the spectral density increased toward ultraviolet. The apparent peak in some of the spectrum was due to the water cut-off of UV around 200 nm, absorption from flask and quantum efficiency variation of the diagnostic system. By fitting the spectra with blackbody radiation, the temperature of the intracavity plasma was ~25,000 K. And later, Hiller et al. (*66*) investigated the light emission intensity with different type of gases inside the cavitation: when the nitrogen was dissolved into the liquid instead of air, the stable SBSL phenomenon disappeared. With a gas mixture composed of 80% nitrogen and 20% oxygen, there was still no SL. Only when noble gas such as argon was doped into the liquid, the stable SBSL appeared again. For both argon and xenon, the SBSL intensity reaches maximum around 1% concentration, which is close to the concentration of argon in air. The spectrum for helium is steeper than other noble gases can be accounted for by thermal Bremsstrahlung from hot gases. The water vapor inside the cavitation gas mixture was not discussed in detail.

Barber et al. (*71*) reported that the aging of water (higher gas concentration with increasing time) can lead to the increase of the rise time, but no quantitative data for the

pulse width. In 1997, Gompf et al. measured the time duration of the light pulse in SBSL to be 60 ps at low gas concentration and low driving pressures to over 250 ps at high gas concentration and high driving pressures, using the time-correlated single-photon counting (TC-SPC) technique. It has a much higher resolution for measuring flash widths than PMT due to the fact that the time delays in arrivals of single photons are measured. This upper bound increase of the light pulse restored hope of some of the previous simple theories for the light emission and undermined all the theories which required ultrashort flash widths such as the strong imploding shocks (*72*). Thus the predicted maximum intracavity temperatures were much lower ~10^4 K (*73*), compared to the previously estimated value ~10^8 K by Wu and Roberts in 1994 (*74*).

Water vapor presence inside the cavitation bubble played a vital role on the characteristics of SBSL. During the expanding phase of the seeded bubble, water vapor will enter the bubble, while at collapse it cannot escape due to the time scale of diffusion is much slower than that of the collapse. Due to the trapped water vapor (*75*), the maximum temperature of the collapsing cavitation bubble is limited because of smaller polytropic index (compared to noble gases) as well as the endothermic chemical reaction ($H_2O \rightarrow OH + H$), which consumes most of the focused energy. Taking the water vapor dissociation into account, the calculated maximum temperatures inside the bubble was only ~6000 K. This seems to contradict experimental results conducted before, and indicated that the numerical model overestimated the amount of water vapor inside cavitation.

The featureless SBSL in aqueous solutions were finally updated by two important experiments in which the characteristic emission lines of the liquid or vapor were spotted in the SL spectrum. Young et al. (*76*) observed spectral lines (OH* at 310 nm and 337 nm, 386 nm and 431 nm source unknown at lower water temperature) for SBSL in water by setting the driving pressure very close to the threshold, under which the emission is so weak that they had to collect the photons over several days. As the driving pressure increases, the OH* emission line might be suppressed or simply overwhelmed by the enhanced continuum emission. Didenko et al. (*67*) reported spectral lines of SBSL in organic liquids similar to MBSL almost one decade ago. The required driving pressures were larger due to the vapor molecules have more vibrational and rotational degrees of freedom to distribute internal energy levels, leading to a weaker temperature increase during collapse. These discoveries eventually close the gap between MBSL and SBSL. The observation of spectral lines will make internal characteristics measurement possible for chemical reactions and plasma characteristics such as temperatures and pressures. As mentioned in the MBSL part, such studies have long been conducted for MBSL, and Suslick and collaborators (*48, 50–52*) have used width and intensities of spectral lines recorded in nonaqueous solution MBSL to measure the temperature and pressure of the collapsing cavitation bubble. Compared to MBSL, the mechanism and bubble dynamics of SBSL is well understood and characterized.

Conditions (Temperature, Pressure) during SBSL

Generally speaking, the light emission in SBSL is thought to be caused by some combination of plasma process, blackbody radiation, and pressure-broadening (*67, 76–*

80). The solitary stable single cavitation bubble provides better conditions for cavitation bubble dynamics study, and theoretical investigations on SL phenomenon with the SBSL flash. The temperature and pressure measurements employed in MBSL is not suitable in the SBSL case. The main reason is the small volume of the single bubble makes it hard for kinetic measurement and the low light intensity with featureless spectra makes spectroscopic analysis difficult. Even though some SBSL experiments demonstrated molecular emission, these spectra were not amenable for further quantitative analysis (*67*, *76*, *81*).

In 2005, Flannigan and Suslick (*68*) discovered the SBSL from concentrated aqueous H_2SO_4 solution is several-thousandfold stronger than the previous SBSL from other liquids. The light flash from a single bubble in a shake tube of H_3PO_4 was discovered to generate up to 10^{12} photons, which was a factor of 10^6 larger than SBSL in water (*82*). Spectrum analysis of SBSL in H_2SO_4 demonstrated emission lines from atoms, molecules, and ions. The emission lines originated from ions was the first authoritative experimental proof of a plasma formation during SBSL. And the discrete emission lines make it feasible to measure the temperature using the spectroscopic two-line measurement method as used in MBSL. Atomic emission lines from electronically excited noble gas were observed (*68*, *83*), which suggested that there was a plasma formed inside SBSL and was the source of light emission. The temperatures of 15,000 K inside the SBSL were estimated by comparing the relative intensities of the Ar* emission lines. This temperature may not reflect the core temperature within the collapsing bubble since there is experimental evidence of the formation of an optically opaque core (*8*, *68*, *84*) inside. By finding the

electron density can be controlled over four orders of magnitude and exceed 10^{21} cm^{-3} (effective plasma temperature 7,000 K to 16,000 K) which is comparable to the densities produced in laser-driven fusion experiments, they claimed their SBSL is inertially confined plasma in an imploding bubble (*4*).

For pressure measurement inside SBSL, the standard techniques of plasma diagnostics implement a complimentary method for probing the pressure from Ar* emission line profiles. The significantly broadened and red shifted emission lines indicated the generation of high densities during the collapsing cavitation. Pressure broadening leads to a Lorentzian profile shape, and the broadening due to the instrument response (instrument function broadening) leads to a Gaussian profile. After applying Whiting's deconvolution derivation

$$w_v = \frac{w_l}{2} + \sqrt{\frac{w_l^2}{4} + w_g^2}, \tag{11}$$

where w_v, w_l, and w_g represent the Voigt, Lorentzian, and Gaussian emission line widths respectively. The total line width (Voigt) and the instrumentation line width (Gaussian) are known, thus the Lorentzian component consisted of pressure broadening and Stark broadening can be solved. In order to extract the pressure broadening, the Stark effects can be subtracted from the remaining line width (*63*). The Stark effect can be estimated using an empirical correlation proposed by Jones et al. (*85*, *86*). Based on the empirical estimation, one can estimate the electron density and then determine the contribution from the Stark effect.

Once the pressure broadening profile is extracted, the number density inside the collapsing single cavitation bubble can be evaluated using the following equation

$$\Delta\upsilon = \sigma_{Ar} n_{Ar} \sqrt{\frac{8k_B T}{\pi^3 \mu_{Ar}}}, \tag{12}$$

in which $\Delta\upsilon$ is the line width, k_B is the Boltzmann constant, T is temperature during SBSL, μ_{Ar} is the reduced mass of the Ar atom and its collision partners, σ_{Ar} is the cross section for Ar defined as $\pi(2r_{Ar})^2$, where r_{Ar} is the van der Waals radius, and n_{Ar} is the number density of Ar atom. With the van der Waals equation of state, the Ar density and temperature revealed the intracavity pressure matched well with adiabatic compression model using the bubble dynamics measured during the experiments. The pressure estimated inside the SBSL ranges from ~1400 bar to 4000 bar for Ar (*11*).

2.3.5. Cavitation Bubble Dynamics

The theory of classic bubble dynamics as known as the collapse of the void was first proposed by Lord Rayleigh (*24*) in 1917 during his investigation of cavitation damage of ship propellers. The form was later refined and developed by Plesset, Prosperetti, and many others scientists over the past century. A review of early work is carried out by Plesset and Prosperetti (*87*), and a later overview was summarized by Prosperetti (*88*). This theoretic section summary is mainly based on the comprehensive SBSL review by Brenner et al (*5*).

2.3.5.1. The Rayleigh-Plesset Equation of The Liquid

For SBSL, the equation governing the sound waves in the liquid are the Navier-Stokes equations in compressible form, as shown in the following symbolic notation form

$$\rho(\partial_t \boldsymbol{u} + \boldsymbol{u} \cdot \nabla \boldsymbol{u}) = -\nabla p + \eta \nabla^2 \boldsymbol{u} + \varsigma \nabla \nabla \cdot \boldsymbol{u}, \tag{13}$$

$$\partial_t \rho + \nabla \cdot (\rho \boldsymbol{u}) = 0, \tag{14}$$

in which $\boldsymbol{u}$ is the fluid velocity, ρ the liquid density, p the pressure, η the shear viscosity, and ς the bulk viscosity of the liquid. The assumptions here is that the liquid is isothermal, thus the equation for the liquid temperature is neglected. The expansion of the flask is orders of magnitude smaller compared to the bubble, thus it is also neglected.

The volumetric oscillation of the sound field around the bubble can be represented with spherical coordinates with radial direction only. The velocity can then be correlated to a velocity potential, $\boldsymbol{u} = \nabla \phi$. The previous two equations then become

$$\rho \left(\partial_t \phi + \tfrac{1}{2} (\partial_r \phi)^2 \right) = -p, \tag{15}$$

$$\partial_t \rho + \partial_r \phi \partial_r \rho + \nabla^2 \phi = 0. \tag{16}$$

Defining the enthalpy $dH = dp/\rho$, and using the transform of $dp = (dp/d\rho)d\rho = c^2 d\rho$ (where c is the speed of sound in the liquid) we have

$$\nabla^2 \phi = \left[\frac{u_r}{c^2} (\partial_t u_r - \partial_r H) \right] + \frac{1}{c^2} \partial_t^2 \phi, \tag{17}$$

where $u_r = \partial_r \phi$ is the radial velocity field. Inasmuch as the liquid velocity is less than local speed of sound c, the first term on the right hand side (RHS) of the equation is negligible. The second term can only be omitted close to the cavitation interface, whereas

this term is significant within the zone containing the cavitation interface near the scale of the sound wavelength.

To solve the above equation for the velocity of the bubble interface dR/dt, the velocity potential near the bubble obey the Laplace equation, $\nabla^2\phi = 0$. With the boundary condition at the bubble interface $\partial_r\phi(r = R) = \dot{R}$, the solution to equation 17 is

$$\phi = -\frac{\dot{R}R^2}{r} + A(t), \tag{18}$$

where $A(t)$ is a constant determined by matching the solution to the ambient pressure (60). In SBSL case, the velocity potential far from the bubble is a standing wave, and the sound field is independent of r, $\phi = \phi_\infty(t)$, since the size of the bubble is way smaller than the imposed sound wavelength. Accounting for the background static pressure P_0 = 1 bar and the driving pressure $P(t) = -P_a sin\omega t$, the total pressure around the bubble is then $p = -\rho\partial_t\phi_\infty = P_0 + P(t)$. Then the velocity field in the liquid around the bubble is

$$u_r = -\frac{\dot{R}R^2}{r^2}. \tag{19}$$

On the bubble interface the force balance provides

$$P_g(t) + \Sigma_{rr}[r = R(t)] = P_g(t) - p[R(t)] + 2\eta\partial_r u_r(r = R) \tag{20}$$

$$= P_g(t) - p[R(t)] - 4\eta\frac{\dot{R}}{R} = 2\frac{\sigma}{R},$$

where Σ_{rr} is the radial component of the stress tensor in the liquid, σ is the surface tension of on the bubble interface, and P_g is the intracavity gas mixture pressure with spatial uniform assumption. Take this equation into equation (15) for the pressure in the liquid, then we have the famous Rayleigh-Plesset equation (RPE):

$$R\ddot{R} + \frac{3}{2}\dot{R}^2 = \frac{1}{\rho}\left(P_g - P_0 - P(t) - 4\eta\frac{\dot{R}}{R} - \frac{2\sigma}{R}\right). \quad (21)$$

Assuming the pressure in the gas within the cavitation bubble is uniform and the bubble wall moves slower compared to gas-phase speed of sound, the pressure-volume relation is given by

$$P_g(t) = \left(P_0 + \frac{2\sigma}{R_0}\right)\frac{(R_0^3 - h_o^3)^\Gamma}{[R(t)^3 - h_o^3]^\Gamma}, \quad (22)$$

where R_0 is or the seeding bubble neutral radius (the radius of the bubble at ambient pressure without external force), Γ is the polytropic index, and h_o is the van der Waals hard-core radius.

The heat transfer between the liquid phase and the gas phase need to be considered for the energy balance. At the cavitation bubble's interface, the boundary condition requires equal heat flux,

$$K_g \partial_r T = K_l \partial_r T_l, \quad (23)$$

in which the K_g and K_l are the thermal conductivities of gas liquid. The temperature gradient can be estimated using the thermal boundary layer thickness δ_g and δ_l in and around the bubble interface,

$$\partial_r T = \frac{T_g - T_s}{\delta_g}, \partial_r T_l = \frac{T_s - T_l}{\delta_l}, \quad (24)$$

in which, T_s is the temperature at the bubble interface, T_g is the temperature inside the bubble thermal boundary layer. The diffusion lengths δ can be deduced from the respective thermal diffusivity χ and the relevant time scale Δt of the bubble oscillation,

$\delta \sim \sqrt{\chi \Delta t}$. Since $K = \chi \rho C_p$, where C_p is the specific heat, and the final result of the temperature distribution is

$$\frac{T_s - T_l}{T_g - T_s} = \sqrt{\frac{\chi_g \rho_g C_{p,g}}{\chi_l \rho C_{p,l}}}. \tag{25}$$

Due to the fact that the density and the specific heat of liquid water are much larger than that of gas mixture, the RHS is typically 10^{-3}~10^{-2} (*5*). The largest temperature gradient occurs inside the bubble, and the temperature at the bubble surface approximately equals the liquid side temperature.

If the heat flux near the cavitation interface is fast compared to the time scale of the bubble motion, then the gas inside the bubble is approximately at the liquid temperature, and the pressure can be determined by an isothermal equation of state with polytropic index $\Gamma = 1$. On the other hand, if the bubble wall motion time scale is larger than that of the heat transfer, then the bubble will undergo adiabatically heating or cooling during collapse or expansion. For monatomic gas such as the noble gas, the heat capacity ratio $\Gamma = 5/3$. If the process is between the two extreme cases, then the process is a polytropic. There is a dimensionless parameter depicting these regimes called the Pélect number, $Pe = \left|\dot{R}\right| R/\chi_g$. The standard procedure to estimate the high energy density states during SL requires solving the heat transfer process through the bubble oscillating cycle and applying the numerically predicted temperature value within the bubble to estimate the pressure based on equation of state. This is a complicated process, despite neglecting the mass transfer on the interface. Different methods (*55*, *87*, *88*) have been proposed to adjust polytropic index continuously between the isothermal and adiabatic values

depending on the Pélect number. Prosperetti and Hao (*89*) demonstrated that this method can still show incorrect results due to the negligence of energy dissipation from thermal processes.

2.3.5.2. Extensions of the Rayleigh-Plesset Equation

If considering the damping effects due to the sound radiation from the collapsing bubble, the radially expanding sound wave emitted from the cavitation will change the velocity potential into

$$\phi = \phi_\infty(t) - \frac{1}{r}F\left(t - \frac{r}{c}\right) \approx \phi_\infty(t) - \frac{1}{r}F(t) + \frac{\dot{F(t)}}{c}. \tag{26}$$

By matching the near-field velocity potential in equation (18), it yields $F(t) = \dot{R}R^2$ and $A(t) = \phi_\infty + \dot{F}/c$. Substitute this into the pressure jump condition, the RPE becomes

$$\rho\left(R\ddot{R} + \frac{3}{2}\dot{R}^2\right) = \left[p_g - P_0 - P(t)\right] - 4\eta\frac{\dot{R}}{R} - \frac{2\sigma}{R} + \frac{\rho}{c}\frac{d^2}{dt^2}(\dot{R}R^2). \tag{27}$$

The sound damping term is near the scale of $\dot{R}/c$ multiply other terms in the equation. When the liquid-gas interface motion is slow $\left|\dot{R}\right|/c \ll 1$, sound radiation can be omitted. Whereas $\left|\dot{R}\right|/c \sim 1$, it is significant. The sound radiation term make RPE from second order to third order and causes a lot unphysical error when solving. Physically only the initial conditions of R and $\dot{R}$ are given, but not $\ddot{R}$. Finding the initial condition of $\ddot{R}$ to avoid spurious unstable solution, it is better to calculate the term $\frac{d^2}{dt^2}(\dot{R}R^2)$ using RPE itself. And then it leads to the Keller equation which was developed by Keller and co-workers (*90, 91*) as shown below

$$\left(1-\frac{\dot{R}}{c}\right)\rho R\ddot{R}+\frac{3}{2}\dot{R}^2\rho\left(1-\frac{\dot{R}}{3c}\right)$$

$$=\left(1-\frac{\dot{R}}{c}\right)\left[p_g-P_0-P(t)\right]+\frac{R}{c}\dot{p_g}-4\eta\frac{\dot{R}}{R}-\frac{2\sigma}{R}. \quad (28)$$

There is a series of equations with one-parameter that originated from equation (27) as shown below:

$$\left(1-(\lambda+1)\frac{\dot{R}}{c}\right)\rho R\ddot{R}+\frac{3}{2}\dot{R}^2\rho\left(1-(\lambda+\frac{1}{3})\frac{\dot{R}}{c}\right)$$

$$=\left(1-(1-\lambda)\frac{\dot{R}}{c}\right)\left[p_g-P_0-P(t)\right]+\frac{R}{c}\dot{p_g}-4\eta\frac{\dot{R}}{R}-\frac{2\sigma}{R}. \quad (29)$$

When the parameter value $\lambda=0$, it becomes the Keller equation, and when $\lambda=1$, it is transformed into the formula derived by Herring (*92*) and Trilling (*93*). The Keller equation yields the best results compared to numerical simulations of full partial differential equation. Other forms of RPE derivatives are summarized and discussed by Lastman and Wentzell (*94*, *95*).

With the enthalpy H into consideration, the speed of sound C is then depend on H. Based on the Kirkwood-Beth approximation, we have the Gilmore equation.

$$\left(1-\frac{\dot{R}}{C}\right)R\ddot{R}+\frac{3}{2}\dot{R}^2\left(1-\frac{\dot{R}}{3C}\right)=\left(1+\frac{\dot{R}}{C}\right)\frac{H}{\rho}+\left(1-\frac{\dot{R}}{C}\right)\frac{R}{c}\frac{\dot{H}}{\rho}. \quad (30)$$

According to Gompf and Pecha (*96*), this enthalpy term helps modeling the varying local speed of sound based on pressure change around the bubble, leading to enormous Mach number reduction at bubble collapse.

The popular form (*97*, *98*) in sonoluminescence is the one that all the terms in $\left|\dot{R}\right|/c$ is deleted for simplification, which is shown below

$$\rho\left(R\ddot{R}+\frac{3}{2}\dot{R}^2\right)=\left[p_g-P_0-P(t)\right]-4\eta\frac{\dot{R}}{R}-\frac{2\sigma}{R}+\frac{R}{c}\frac{d}{dt}(p_g). \qquad (31)$$

Lord Rayleigh's bubble dynamics $R\ddot{R}+3/2\dot{R}^2=0$ is the collapse of a void, only liquid inertia mattered, and contributions from other effects such as surface tension, intracavity pressure and viscosity are all neglected. He pointed out that the singularity in the liquid is the reason for cavitation damage as well as the SL light emission via energy focusing. But something need to prevent the cavitation interface velocity from diverging. For the RPE to approach SL, it must have some physical effects that achieve this. The viscous stress and surface tension are too weak (*5*). The pressure in the gas with polytropic process can be stronger than the inertial acceleration. Though the gas pressure can halt the Rayleigh collapse, it turns out the most strongly divergent term is the one associated with sound radiation into the liquid during the final stage of collapse in equation (31). Up to 50% of the cavitation mechanical energy during the collapse may be transferred to a radiated pressure wave (*96*).

2.3.5.3. The Bubble Interior

Before Flannigan and Suslick (*4*, *68*) using the plasma pyrometer measure the temperatures, pressures inside the bubble, there is no direct measurement to know about the conditions inside the bubble. Although the plasma pyrometer of discrete emission line spectra tell the story inside certain SL bubbles, for most aqueous solution cases in cavitation luminescence, the featureless spectra due to water vapor still hide those information. Direct measurement of the plasma state inside the bubble are severely hard

to achieve. One possible approach is using the bubble dynamics modeling as a basis for predicting the temperatures, pressures within the oscillating cavitation.

Assuming local equilibrium, gas motion in the cavitation bubble can be represented by the Navier-Stokes equation and the conservation of mass and energy as shown in the following Einstein notation form

$$\partial_t \rho_g + \partial_i(\rho_g v_i) = 0, \tag{32}$$

$$\partial_t(\rho_g v_i) + \partial_j(p_g \delta_{ij} + \rho_g v_i v_j - \tau_{ij}) = 0, \tag{33}$$

$$\partial_t E + \partial_i\big[(E + p_g)v_i\big] - \partial_i\big(v_j \tau_{ij}\big) - \partial_i(K_g \partial_i T) = 0. \tag{34}$$

The velocity components are v_i, and ρ_g, p_g are the gas density and pressure, the total energy density is in the form of enthalpy $E = \rho_g e + \rho_g v^2/2$, e is the specific internal energy. K_g is the thermal conductivity of the gas and T is the gas temperature, δ_{ij} is the Kronecker delta. The viscous stress tensor is given by

$$\tau_{ij} = \eta_g(\partial_j v_i + \partial_i v_j - 2/3\delta_{ij}\partial_k v_k), \tag{35}$$

in which η_g is the dynamic viscosity of gas, and assume that the second viscosity effect is negligible. In order to solve these equations, an equation of state which connects system and material properties is needed to complete those equations. There are three major methods assuming spherically symmetric bubble collapse to apply boundary conditions at the cavitation bubble interface: 1) inviscid models, 2) dissipative models, and 3) dissipative models including phase change.

Inviscid models

Based on the SBSL light pulse duration (<50 ps) measured by Barber et al. (*71*), early theoretic studies concentrated on the notion of imploding shock were vital for SBSL (*99–101*). One of the earliest numerical solution of the gas-dynamical equation driven by RPE was derived by Wu and Roberts (*100*). The major assumptions of their work are a) the dynamic viscosity and thermal diffusion are negligible, b) there is no heat and mass transfer on the bubble interface, and c) an equation of state in the form of van der Waals with a fixed polytropic index or specific heat ratio $\Gamma = 7/5$. With this model, Wu and Roberts (*74*, *100*) predicted a spherical shock wave focusing to the bubble core and then radiating outward. Based on the model results, the temperature inside increased over 10^8 K and light pulses duration was predicted as 1.2 ps. There were debates against this theory with direct experimental evidence since the imploding shock theory was proposed. Following the research of Ohl et al. (*102*, *103*) on laser-induced cavitation, which also emit light during bubble collapse, Baghdassarian et al. (*104*, *105*) discovered that highly aspherical bubbles can still give off considerable light emissions. Evans demonstrated that an asphericity of 5% on the bubble interface is capable of disrupting the energy focusing power of a shock.

Dissipative models

The scenario of assuming heat and mass transfer negligible on the bubble boundary make the inviscid models less convincing and scientists begin to realize the need of implementation of dissipation to the gas dynamics model, giving some estimates for the

heat transfer. Vuong and Szeri (*73*) mentioned viscous and thermal dissipation in solving the equations of motion for the gas phase inside the cavitation bubble, which they and also Cheng et al. employed a linear relation shown below

$$K_g = K_g(T_0)\frac{T}{T_0} \tag{36}$$

involving temperature and heat conductivity. The heat transfer on the water side was describe using the following equation

$$\partial_t T_w + u\partial_r T_w = \chi_l \frac{1}{r^2}\partial_r(r^2\partial_r T_w). \tag{37}$$

In Vuong and Szeri's paper, there was no shock waves demonstrated in argon bubbles. The radial temperature distribution in the collapsing bubble was not spiked dramatically near the core, and exhibited slow variations for most of radius, accompanied with a large temperature gradient near the bubble boundary.

Dissipative models including water vapor

The dissipative model become more complex over time, and scientists realize that water molecules within cavitation bubble plays an important role in heat and mass transfer. The water vapor inside the cavitation bubble will undergo chemical reactions (more than 25 different reactions) that impact the gas temperature (*55*, *106–108*). Moss et al. (*109*) carried out the first numerical simulation of a SBSL with both xenon and water vapor inside. Due to the fact that water molecules have more internal degree of freedom, including of water vapor results into a smaller polytropic index. Endothermic reaction of water vapor such as dissociation reduces heating and shock waves may occur close to the

core. Storey and Szeri (*108*) employed a varying water vapor content instead of a constant one as in the model by Moss et al. (*75*)

Phase changes on the bubble boundary are modeled based on a kinetic theory by Carey in 1992 (*110*). The mass transfer rate per unit area at which water molecules permeate the interface is proportional to the water vapor partial pressure difference $p_{H_2o} - p_{sat}$, in which p_{H_2o} is the partial pressure of water vapor and p_{sat} is the saturation pressure at the temperature of interface. The fraction of H_2O molecules attach to the interface is defined as accommodation coefficient σ_a, this parameter was adapt to 0.4 according to Yasui (*106*) and Eames et al. (*111*). In order to show how significant the water vapor effect is, Storey and Szeri (*108*) studied a seeded bubble initially filled with argon with $R_0 = 4.5$ μm and driven at $P_a = 1.2$ bar and $f = 26.5$ kHz. Due to the implementation of model with water vapor effects, the maximum temperature inside the luminescing bubble at minimum volume decrease from 20,900 K predicted by Vuong and Szeri (*73*) to 9,700 K. Owning to the fact that lower heat capacity ratio including water molecule (water vapor ~1.31 and argon ~1.66), the amount of water molecule in the bubble was not constant and there was no shock waves observed. As bubble reached maximum volume, the amount of water molecules inside the gas content will end up to 90%. Vapor transfers into liquid on the interface again during collapse, but not 100% due to the time scale of collapse is much smaller than the time scale of water vapor mass transfer. There are two major steps for water vapor transport process, the diffusion to the boundary and condensation on the wall. The time scales of the two steps involved are vapor diffusion in the bubble and condensation at the wall:

$$\tau_{dif} = \frac{R^2}{D_{H_2O}(R,T)} \approx \frac{1}{D_{H_2O}(R,T)} \frac{R_0^3 T_0^{1/2}}{R T^{1/2}}, \tag{38}$$

$$\tau_{con} = \frac{R}{c_g} \sqrt{\frac{2\pi \Gamma M_{H_2O} T_0}{9\sigma_a^2 M_0 T_{int}}}, \tag{39}$$

where $c_g = \sqrt{\Gamma p_{g0}/\rho_{g0}}$ is the speed of sound in gas at the initial state, M_{H_2O} is the molecular mass of water and M_0 stands for molecular mass of the initial bubble content. Storey and Szeri (*108*) compared the above time scales with the time scale of the collapse $\tau_{dyn} = R/|\dot{R}|$, they find that: in the early part of the collapse, $\tau_{dyn} \gg \tau_{dif}, \tau_{con}$, the molar fraction of water vapor is uniform inside the bubble for different radial positions. Since water vapor has sufficient time to condense, the water vapor fraction is shrinking. When $\tau_{dyn} \ll \tau_{dif}, \tau_{con}$ in later stage of collapsing process, the water vapor (~14%) is trapped inside the bubble. With the comparison between the diffusion time scale and the condensation time scale, they also found out the vapor transport was always diffusion constrained, $\tau_{dif} > \tau_{con}$.

They also discussed the chemical reactions of the water vapor in the later section of their paper according to the reaction scheme from Maas and Warnatz (*112*) and covered 19 forward and reverse elementary reactions of the nine species H, H_2, Ar, O, O_2, OH, HO_2, H_2O, and H_2O_2. The reaction rates were based on Gardiner's book (*113*) and in the high pressure limit based on data from GRI-Mech 3.0 online database. Including the chemical reaction of the water vapor, the maximum temperature of the previous case decreases from 9,700 K (only consider water vapor, chemical reaction not included) to 7,000 K. Most of the water vapor chemical reactions are endothermic and hence majority

of focused energy is consumed. An easier interpretation is treating the chemical pathway as additional degrees of freedom, which reduces the polytropic index even more. Due to the collision frequency at high densities is still high, thermo-chemical equilibrium should prevail in the collapse up to the point of minimum radius.

2.3.5.4. Simple models

In the detailed review of Brenner et al. (*5*), some reasonable simplifications is recommended to ease the complexity of the aforementioned models. For example, the approximation of the bubble's interior with spatially uniform, unsteady pressure $p_g(t)$ and temperature $T(t)$. There are two types of simple models, one that can assume no heat and mass transfer on the bubble interface and one that including those effects.

Homogeneous van der Waals gas without heat and mass exchange

The simplest model is just assuming the cavitation bubble collapsing an adiabatic process (*114*, *115*), thus

$$p_{gas}(t) = \left(P_0 + \frac{2\sigma}{R_0}\right)\frac{(R_0^3 - h_o^3)^\Gamma}{[R(t)^3 - h_o^3]^\Gamma}, \tag{40}$$

and the corresponding temperature equation

$$T(t) = T_0\frac{(R_0^3 - h_o^3)^{\Gamma-1}}{[R(t)^3 - h_o^3]^{\Gamma-1}}, \tag{41}$$

where Γ is the polytropic index. The obvious limitation is that this adiabatic bubble compression neglect heat exchange between the bubble and the liquid around. For majority of the bubble oscillating process, there is nearly unconstrained heat exchange, which means that the process is isothermal. Whereas near singularity the Pélect number is

larger than 1. Therefore the ratio of the specific heat $\Gamma = 1$ in most of the time, and it approaches to adiabatic value near the cavitation collapse $\Gamma \to \gamma$. This kind of transition will take place when Pélect number is approaching unity.

Prosperetti (*116*) proposed a transition function of the polytropic index $\Gamma[\mathrm{Pe(t)}]$ connecting the isothermal and adiabatic processes. Hilgenfeldt et al. (*79*, *117*) used this method to estimate intracavity characteristics inside a SBSL bubble. The RPE is implemented by a differential version of equation (41) with varying $\Gamma[\mathrm{Pe(t)}]$,

$$\dot{T} = -\{\Gamma[\mathrm{Pe(t)}] - 1\}\frac{3R^2\dot{R}}{R^3 - h^3}T - (T - T_{w0})\chi_g/R^2, \tag{42}$$

in which T_{w0} is the ambient liquid temperature and χ_g is the gas thermal diffusivity. With this approach to complete the RPE, the results are comparable to Storey and Szeri (*108*), but the temperature is higher since no heat loss and mass exchange are included.

Homogeneous van der Waals gas with heat and mass exchange

The complex version of the simple model will take the heat and mass transfer into account explicitly. In 1997, Yasui (*106*) proposed the first models of this type, in which he assumed a homogeneous properties inside the cavitaton with temperature and pressure dependent on time. The mass transfer was modelled with condensation and evaporation, and the heat transfer was modelled by an energy flux depending on the compression, the temperature gradient, and phase change. They also assumed a thin film of liquid water around the bubble interface that can be heated. There are 25 chemical reactions of water

vapor employed based on previous research by Kamath et al. (*55*), and the overall effect of these reactions should be endothermic.

According to Yasui's result, the majority of the bubble is filled with water vapor, and there is still ~1% of water remaining at collapse. The maximum temperature inside the bubble is ~10,000 K, which is consistent with the complete model reported by Storey and Szeri (*108*). Yasui's model is helpful for scrutinizing the conservation of energy at singularity. For a SBSL event, there are 1.4 nJ thermal energy reduction through chemical reaction and 0.6 nJ energy reduction through heat conduction at the last 120 ps before the singularity. The energy loss due to photon emission is only ~0.2 pJ.

Toegel et al. (*118, 119*) developed a simple diffusion-constrained model for heat and mass transfer on the bubble interface with a boundary layer approximation. The intracavity number of water molecule change over time is described by the following equation

$$\dot{N}_{H_2O}^{d} = 4\pi R^2 D \partial_r n|_{r=R} \approx 4\pi R^2 D \frac{n_0 - n}{l_{diff}}, \tag{43}$$

in which n_0 stands for the equilibrium number density of water vapor molecules at the interface and n is their actual number density. With dimensionless analysis, the diffusion length is determined as $l_{diff} = \min[(RD/\dot{R})^{1/2},\ R/\pi\ ]$, where D is the gas diffusion constant. The cut-off is for keeping the boundary layer from unrealistically large. And the heat flux within the diffusion length can be expressed as

$$\dot{Q} = 4\pi R^2 \chi_{mix} \frac{T_{w0} - T}{l_{th}}, \tag{44}$$

where Q is the total heat of the bubble, T_{w0} is the temperature under equilibrium condition, χ_{mix} is the thermal diffusivity of the gas mixture, and the thermal diffusion length is $l_{th} = \min[(R\chi_{mix}/\dot{R})^{1/2},\ R/\pi\ ]$.

Toegel et al. (*119*) implemented the chemical reactions in their boundary layer model, the most vital endothermic process is

$$H_2O + 5.1\ eV \leftrightarrow OH + H, \tag{45}$$

and the inclusion of this process demonstrated the essential effects of more complicated reaction scheme. And thus resulted into the ordinary differential equation for the intracavity temperature,

$$C_v\dot{T} = \dot{Q} - p_g\dot{V} + h_w\dot{N}^d_{H_2O} - \sum_X \frac{\partial E}{\partial N_X}\dot{N}_X, \tag{46}$$

in which h_w is the enthalpy of water molecules near the bubble wall, the summation consists of all species ($X =$ Ar, H_2O, OH and H). The derivatives $\partial E/\partial N_X$ and C_v are temperature dependent and will involve rotational and vibrational internal energy levels in various molecules.

Most of the models taking chemical reactions into account inside the cavitation bubble seem to underrate the temperature within the bubble. Except Yasui's model, in which water vapor is not significant due to the fast transport rate, all of these models predicted that the gas temperatures inside the bubble below 10,000 K in the SBSL. Under these temperatures, there are not enough photons produced to match the experimental results. Toegel et al. (*119*) suggested that the intracavity high densities actually prefer the back reaction process ($OH + H \rightarrow H_2O$,) according to the chemical equilibrium law, also

known as the Le Chatelier-Brown principle. Higher temperatures inside the bubble are made feasible due to the fact that the most significant energy-consuming water dissociation reaction (endothermic process) is suppressed. This suggests that extrapolation of temperature and pressure dependent reaction rates acquired from other experiments is not suitable for SBSL regime particle densities. Therefore the reaction rates deduced from the partition function is suggested.

Storey and Szeri (*120*) came up with another simple ODE model which relied on the ratios of the relevant time scales for bubble dynamics, molecules exchange and heat transfer, neglecting the assumption of boundary layers for heat and water molecule exchange. After verification with their full simulation, the same trend of peak temperature, intracavity argon mass percentage and the number of chemical reaction products were found.

Sonoluminescence light emission

Certain excitations will dominant over others within the cavitation near singularity based on the final temperatures achieved. The thermal emission involves a large number of different processes. As temperatures ranges from several hundred kelvin to many thousands kelvin, those excitation processes can be molecular recombination (*121*), collision-induced emission (*122*), molecular emission (*67*), excimers (*123*), atomic recombination (*117*), radiative attachment of ions (*123*), neutral and ion bremsstrahlung, or emission from confined electrons in voids (*124*). Due to the large uncertainty of temperatures inside SBSL bubbles, most of these mechanisms could be possible. Though

thermal emission does not necessarily end up with a blackbody spectrum, all thermal processes can contribute to blackbody radiation.

The publication of Gompf et al. (*125*) demonstrated that light emission pulse profiles in different part of spectrum (UV 300-400 nm, red part 590-650 nm) had no detectable difference. This result was different from thermal models favoring blackbody emission as surface emitter. Those model predicted that the gas mixture in the cavitation bubble maintains lower temperatures for a longer time compared to higher temperatures. Thus the light emission duration at long wavelengths should be longer (red pulse should be about twice of UV pulse) than at short wavelengths. Hiller et al. (*126*) and Moran and Sweider (*127*) verified these discoveries, although the Dr. Putterman's group did actually report a slightly longer pulse in the red than in the UV if cooled water was used.

2.3.6. Laser-induced Cavitation Luminescence

The first laser-induced cavitation luminescence was recorded by Buzukov and Teslenko in 1971 (*128*), they termed it sonoluminescence following focusing of laser radiation into a liquid though no ultrasonic device was used for cavitation generation. Later when revisited by Ohl et al. (*102*) in 1998, it was named as single cavitation bubble luminescence (SCBL). The cavitation are generated by focused laser light, and the light emission of the collapsing cavitation at the following singularity was recorded by an ICCD camera. The laser they used is a Q-switched Nd:YAG laser with 8 ns pulse width and up to 20 mJ at wavelength of 1064 nm. For spherical bubble collapse, the maximum radius ranges from 0.8 mm to 1.5 mm when luminescence occurs. Aspherical collapsing bubbles

luminesce at the bubble site of the jet impact. In order to further boosting the collapse strength of laser induced cavitation, Ohl (*103*) later in 2000 employed acoustic driven technique to explore the enhancement and reduction of the luminescence from the laser induced cavitation due to the phase difference and sound amplitude.

In 1999, Baghdassarian et al. (*104*) also investigated the laser-induced cavitation luminescence for pressures between 1 and 15 bars. In higher pressure, the bubble generated was instable and splits into two collapse. And interestingly, they pointed out that the luminescence is independent of whether the water contains ambient dissolved air, completely degassed, or filled with argon or xenon. To further expand the scope of laser-induced cavitation luminescence, Baghdassarian et al. (*129*) conducted experiments in liquid nitrogen and liquid argon. Light emission during the first collapse point (first singularity) were also observed, but the light pulse at the order of 100-1000 ns compared to 2-8 ns case in water. Later in 2007 (*130*), atomic lines in liquid nitrogen and liquid argon were observed, the spectrum even contains chromium line came from stainless steel metal flake in dropped in the cryogenic liquid by the shock wave.

Eventually, the spectrum analysis for laser-induced cavitation luminescence was measured for different maximum bubble size in water. Cavitation size as large as 2 mm show a molecular OH* band at 310 nm in the spectrum and other part of the spectrum was fitted with a blackbody curve at temperature of 7800 K (*105*).

Dr. Gary Williams's group conducted series of research on this phenomenon. In 2005, Brujan et al. (*131*) investigated the laser-induced cavitation luminescence in pressurized water from 0.25 to 15 bars. They reported that the duration of the light pulse

is linear to the maximum bubble size, and with given bubble size, it increases with the pressure in a power law $\sim p^{0.38}$. The spectrum analysis displayed a broad band featureless blackbody spectrum with fitted temperature from 8100 K at 1 bar to 9400 K at 10 bars. Due to hydrodynamics instabilities during high pressure collapse, the blackbody temperature dropped due to the energy focusing happened in more than one collapsing site. The spectra analysis for laser-induced cavitation bubbles near rigid boundaries demonstrated OH* emission bands (*132*). And when the bubble got closer to the rigid wall, the collapsing strength reduces as indicated by decreasing blackbody temperature. Effect of viscosity on the luminescence was discussed by Englert et al. (*133*) in 2011 using water-glycerin mixture.

Precursor luminescence pulse consisted of atomic emission line (589 nm for Na, 671 for Li, 767 nm for K) was observed by Chu et al. (*134*) in laser-induced cavitation luminescence. The atomic emission line duration was found to depend on the salt concentration, and the duration of the blackbody pulse was reduced by up to 30% as salt concentration increased.

Bubble shape during collapse is crucial for the relative luminescence energy generated inside. Supponen et al. (*135*) investigated the luminescence from laser-induced cavitation deformed in uniform pressure gradients. They found out that luminescence energy decreases rapidly as the bubble asymmetry quantified by non-dimensional number increases.

2.4. Bioinspired Design for Cavitation Generation

There is a long history of finding efficient processes using biological inspiration, like the earliest human-made ropes inspired from vines, sailing from Velella or Portuguese man o' war and airplanes from flying birds (*136*). The well-known classic example of modern bioinspired engineering is the invention of 'Velcro' fastener by George De Mestral, borrowing the idea of burr, the nature's design for the method of seed dispersal (*137*, *138*).

In the animal kingdom there are a very limited number of plasma generation methods, like the snapping shrimp (*7*). The nature's design for plasma generation might be a high efficient method due to the long history of biological evolution. Dr. Lohse's group (*7*, *10*) investigated the cavitation and light emission process using a snapping shrimp (*Alpheus heterochaelis*) in seawater aquarium with pre-calibrated photon detector and hydrophone. They claimed that the total number of photons emitted from the cavitation bubble is up to 5×10^4, which is one to two orders of magnitude less than a typical cycle of single bubble sonoluminescence (SBSL). Mantis shrimp (*139*, *140*) (*Stomatopod*) generates cavitation between the surface being struck and the dactyl heel with peak speeds of 14~23 m/s with a high probability of generating light emission which is not yet verified in the cavitation collapse. Snapping shrimp can generate cavitation by shooting out high-speed water jet with a sudden snap of their giant snapper claw and make loud cracking noise (*141*, *142*) at the same time. The collapsing process of cavitation is so intense that gasses inside the cavitation bubbles even generate plasma in the form of light emission (*7*, *10*). This light emission phenomenon is similar to sonoluminescence in that

it occurs at the high pressure, high temperature singularity following the collapse of a cavitation bubble. Electrically induced microbubbles and plasmas (*143–145*) and laser-induced bubbles and breakdown (*104*, *146*, *147*) are slightly different in that they initiate as a high pressure, high temperature singularity then expand and oscillate as a cavitation bubble.

Attempts to mimic the shrimp's cavitation processes have been attempted by several researchers. Based on the morphology of snapper claw of a snapping shrimp (*Alpheus bellulus*) scanned by μ-CT, D. Hess et al. (*148*) designed a 70 times scaled-up mechanical device with the 2-dimensional mid-plane curves of the plunger and matching socket. This bio-inspired device was designed to match the Reynolds Number of the shrimp and was able to reproduce some of the jetting and vortex formation mechanism. A Ninjabot mimicking the mantis shrimp was built by S. Cox et al. (*149*). This design focused on mimicking the physical musculature of shrimp for energy storage and power amplification. This was used to investigate the mechanical principles, fluid mechanics and cavity generation. These two works point out independently important design aspects of non-dimensional scaling, morphology, and sudden energy release. However, neither of these focused on or were able to reproduce all the cavitation collapse processes.

3. DESIGN OF BIOINSPIRED DEVICE*

Biology is engineering.

--- Daniel Dennett

3.1. Overview

Design is a creative human endeavor that is the essence of engineering. It sits at the intersection of science, art, business, psychology, and politics (*136*). However, the design in Nature can expand the space of possible engineering solutions to a different level due to the long history of evolution of species. This chapter will cover the process of how this bioinspired idea get conceived, nurtured, embodied, and modified.

This bioinspired design aims to explore and reproduce the cavitation generation, cavitation collapse, shock waves and plasma generation reported to be generated by the living shrimp with a synthetic device. The general approached was to mimic the 3D morphology of the shrimp claw, have rapid energy, and to focus on using the cavitation number as the major non-dimensional scaling parameter. The bioinspired device similar to a snapping shrimp snapper claw allows us to carry out repetitive and consistent experiments on cavitation processes and plasma generation. This study is to fill the gap and exhibits solid evidence of mechanically generated plasma in the form of light

* Reprinted with permission from "Bioinspired mechanical device generates plasma in water via cavitation" by Tang, X., & Staack, D. (2019). Science advances, 5(3), eaau7765, © The Authors, some rights reserved; exclusive licensee American Association for the Advancement of Science. Distributed under a Creative Commons Attribution NonCommercial License 4.0 (CC BY-NC) http://creativecommons.org/licenses/by-nc/4.0/.

emission. Through this we learn more about the snapping shrimp, more about energy focusing processes, and more about underwater plasmas.

3.2. The Claw Morphology

Even though the previous research done by Hess et al. (*148*) only utilized the 2D mid-plane curve of a snapping shrimp snapper claw, they implemented an effective method to obtain the snapper claw 3D morphology of one snapping shrimp species, *Alpheus bellulus*. The snapping shrimp utilized for bioinspired design in this project is *Alpheus formosus* (*150*, *151*), as shown in Figure 8, which were purchased from peppermint-shrimp via eBay and kept in saltwater aquarium for months. The molt of the snapper claw was collected for μ-CT scanning in Cardiovascular Pathology Laboratory of College of Veterinary Medicine and Biomedical Science at Texas A&M University. The snapper claw molt was stabilized with cotton wool and scanned twice in the μ-CT (X-Tek Hawk CT and X-ray Imaging System). The open claw scan was conducted first with the dactyl plunger part raised to the cocked position with a resolution of 17.5 μm. Afterward, the claw was closed and scanned for the second time with a higher resolution of 9.7 μm. The microscope images of the snapper claw are illustrated in Figure 9(a), (b), (c) and a typical μ-CT image for the open claw scan is shown in Figure 9(d).

Figure 8 *Alpheus formosus*, the striped snapping shrimp (*12*)**.**

The complex 3D surface data were captured by Inspect-X and reconstructed by CT Pro. Then the reconstructed model was converted into mesh file using software VGStudio MAX 3.0 with appropriately adjusting opacity curve and thresholds for different materials in surface determination. Due to the fragile nature of the shrimp claw molt, one side of the claw joint detached from its original position, see Figure 10(a), which illustrates the reconstructed 3D rendering of the converted mesh file in an open source software MeshLab (*152*, *153*). The mesh file contains all the information including claw morphology and quantitative 3D geometrical data of the snapper claw. With careful modifications such as bridging and filling cavity holes in matching socket area and reducing unnecessary points and surfaces, the open claw was divided into two separate manifold parts, the dactyl part and the propus part shown in Figure 10(b) and (c) respectively. Then those manifold mesh file can be imported into Solidworks as solid bodies for future design after uniformly simplifying the surface point clouds.

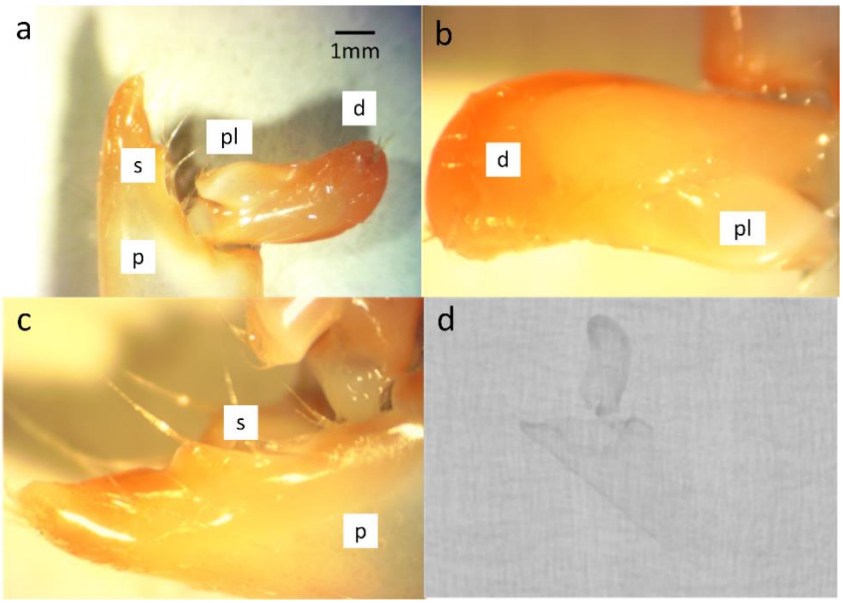

Figure 9 Snapper claw molt of Alpheus formosus
(a) Snapper claw molt at its cocked position (*12*). d: dactyl, pl: plunger, s: socket, p: propus (b) dactyl and plunger (c) the matching socket and immobile propus (d) typical μ-CT image of the shrimp molt.

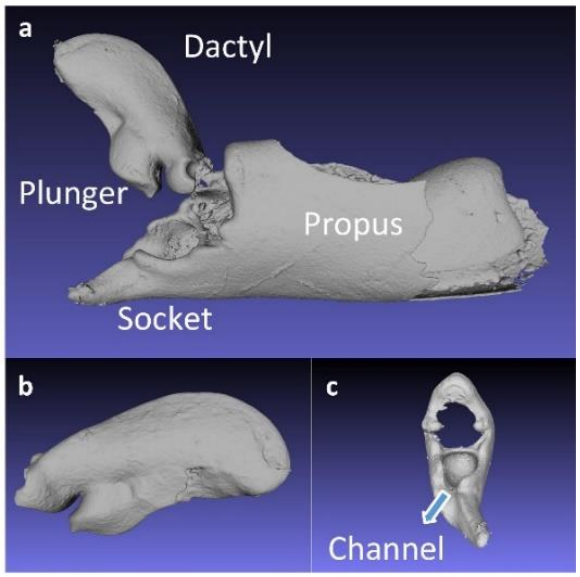

Figure 10 3D rendering of converted snapper claw mesh shown in MeshLab (*12*)
(a) Open claw (b) claw dactyl part (c) claw propus part

3.3. Bioinspired Engineering Design

3.3.1. Conceptual CAD Design

With geometrical data of snapper claw imported into CAD software as solid bodies, alignment of the two parts were carried out with the approximation that assuming there is a virtual rotating axis for the dactyl plunger. Since the actual shrimp joints are similar to human joints which are face-to-face joined, this virtual rotating axis was located by clearance detection of the plunger in the socket. Post production of the minor wear on the bioinspired claw after repetitive snaps further ensured a proper fit. Torsion springs were chosen for providing the driving torque mimicking the shrimp muscle. Due to the small size of the snapper claw (dactyl length = 4.87 mm), it was scaled up to 5 times (5X) to facilitate manufacture and mechanical integration.

Geometrically the claw consists of three main parts which lead to the issuance of the high velocity water jet, the plunger, the socket, and the channel. These are labeled in Figure 10. The plunger displaces the water in the socket forcing it out through the channel. There is an angle deviation between the water channel for generating the high-speed jet and the mid-plane of the propus part. From the top view of high frame rate videos, this angle is varying depend on the closing kinematics, which is mainly affected by torsion spring torque, liquid property, momentum inertia of the dactyl plunger. For double weak torsion spring configuration and the 3D printed white strong plastic dactyl plunger operating in water, this angle is approximately 25˚ for double 1 torsion spring configuration case. Evolutionarily this angle is probably important as it forces the jet development and cavitation to occur off of the claw surface and avoid self-inflicted

implosion damage. The dactyl part was modified near the virtual rotation axis for attachment of the torsion spring assembly and flanged ball bearing assembly, see Figure 11(a). The immobile propus part is shown in Figure 11(b), and the cavity volume of the 5X socket was estimated as 222.89 mm^3 using computer-aided design (CAD) software as exhibited in Figure 11(c). In order to ensure the compatibility with various torsion springs, groove size for holding right-hand and left-hand 90-degree torsion springs were carefully designed.

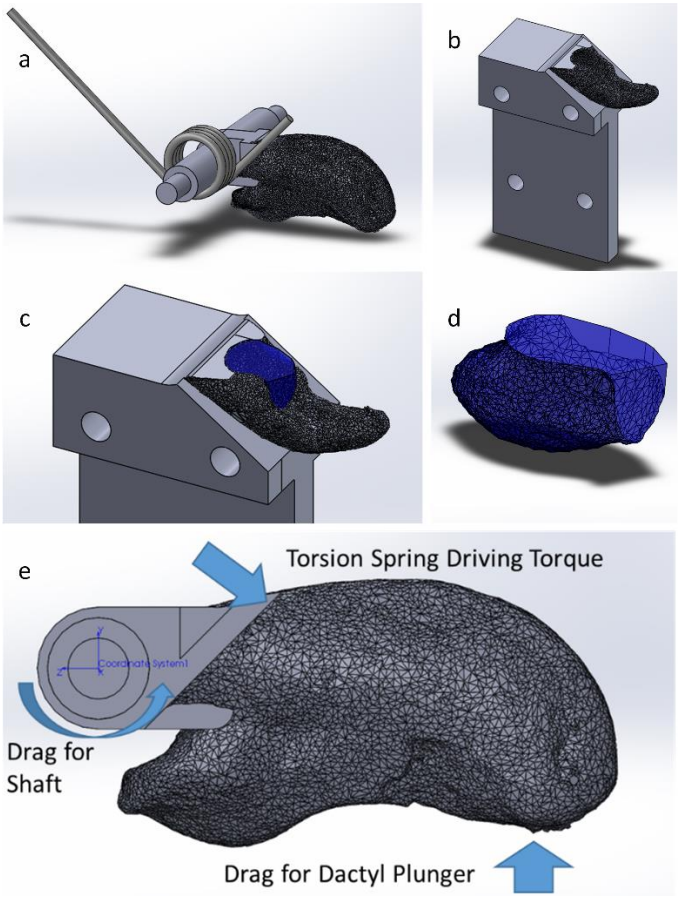

Figure 11 Modified dactyl CAD model (*12*)
(a) Dactyl with step shaft and torsion spring (b) immobile propus CAD model (c) immobile propus and socket cavity volume (d) socket volume geometry captured in CAD (e) free body diagram of rotating dactyl with major forces

An important aspect of designing a functional shrimp claw is choosing the spring sizes and plunger angular velocity to create an effect similar to the real shrimp. The scaling parameter chosen was to match the cavitation number $\sigma = (p - p_v)/(1/2\rho v^2)$, where ρ is the density of the fluid, p is the local pressure, p_v is the vapor pressure of the fluid and v is a characteristic velocity of the flow. We have chosen to use the cavitation number, rather than another number (e.g. Reynold number) because we believe the dominant physical process is related to dynamic pressure and not viscous drag. To mimic the shrimp process in saline water, the controllable parameter is the flow velocity which directly relates to the time it takes the plunger to displace the socket cavity volume which in turn is directly related to the angular velocity and tip velocity of the plunger. From literature (*10*) the flow velocity is given as about 25 m/s and the closing time of the claw from their video to be 600 μs. These lead to a target plunger tip velocity around 32~35 m/s.

3.3.2. ODE Model for Dactyl Tip Speed Prediction

The plunger velocity is dependent on the model moment of inertia, fluid drag, and torsion spring driving torque ignoring the negligible torque induced by gravity and bouncy forces. The density of the 3D printing material EOS PA2200 (0.93 g/cm^3), snapping shrimp plunger chitin layers with inner tissues (*154*) and water are close. In the design process a simple ordinary differential equation (ODE) was proposed according to the free body diagram shown in Figure 11(d) for depicting the rotating motion physics as illustrated in Equation (47). There are only four major terms. The inertial term, the spring driving torque, fluid drag on the plunger, and fluid drag on the rotating shaft respectively

from the left to right. The force required to expel the water from the socket by the plunger is not included.

$$I_{xx}\frac{d^2\theta}{dt^2} = -k\theta + \frac{C_{Dp}\rho b_1 R_1^4}{8}\left(\frac{d\theta}{dt}\right)^2 + \frac{C_{mc}\pi\rho R_{shaft}^4 W_{shaft}}{2}\left(\frac{d\theta}{dt}\right).^2 \quad (47)$$

In the equation, k is the torsion spring coefficient, and θ is the deflection angle from rest position of torsion spring, I_{xx} is the moment inertia about the rotation axis. C_{Dp} is the drag coefficients for dactyl, including corresponding friction drag and pressure drag. C_{mc} represents the fluid drag coefficient for the rotating shaft (*155*, *156*). b_1 is the width of the dactyl, W_{shaft}, is the width of the shaft, ρ is the density of the liquid, R_1 is the distance from dactyl tip to the rotation axis, R_{shaft} is the radius from shaft cylinder surface to rotation axis. The first, second and forth terms are relatively straight forward, the dactyl drag term is more complicated as it involves a variation in flow velocity along the dactyl. For the dactyl drag term, it is the results of integrating along the length of the dactyl as shown in equation 2. Drag coefficients data by Hoerner (*157*), approximations are selected, $C_{Dp} \approx 0.5$ are used for the dactyl. For the shaft the radius is constant and no integration is needed, a value of $C_{mc} = \frac{8}{Re}, Re < 60$ and $C_{mc} = (\frac{1}{-0.8572+1.25\ln(Re\sqrt{C_{mc}})})^2, 60 \leq Re \leq 5.6 \times 10^6$ is used. The Reynolds number for the dactyl tip with dactyl length as the characteristic length ranges from 0 to 7.55×10^5, and for the rotating shaft with shaft diameter as the characteristic length is 0 to 1.517×10^5. As simplified this ODE is readily solved using an explicit Runge-Kutta scheme (ode45) in Matlab.

$$F_{Dp} = \int_0^{R_1} dF_{Dp} = \int_0^{R_1} C_{Dp}\frac{1}{2}\rho\omega^2 r^2 b_1 dr \quad (48)$$

$$\left\|\overrightarrow{D_p}\right\| = \left\|\vec{r} \times \overrightarrow{F_{Dp}}\right\| = \int_0^{R_1} C_{Dp} \frac{1}{2} \rho \omega^2 r^3 b_1 dr = \frac{C_{Dp} \rho \omega^2 b_1 R_1^4}{8}$$
$$= \frac{C_{Dp} \rho b_1 R_1^4}{8} \left(\frac{d\theta}{dt}\right)^2$$

Three types of 90-degree torsion springs shown in Figure 12 are chosen. The detailed parameters are listed in Table 1. The coefficient of torsion spring, k, is calculated by the torque value at 90˚ deflection angle provided on McMaster website. The moment inertia component I_{zz} can be easily obtained from Solidworks with the material density known for the specific plunger model. A torsion spring goes from strong to weak. Relative to neutral angle the spring is acting theta = 100^o to 25^o. It is not known precisely how this compares to a real shrimp. By variation of the springs a range of velocities can be attained.

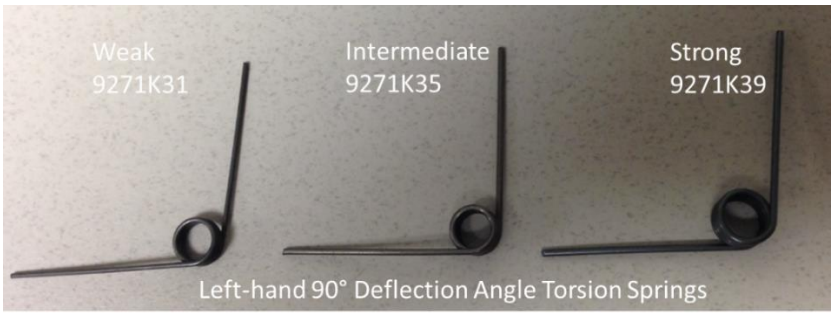

Figure 12 Three types of 90-degree torsion spring

Table 1 Torsion Spring Parameters (*12*)

Spring type	Spring OD	Wire Dia.	No. of Coils	Torque in.-lbs.	Moment N*m	Spring Length @Torque	k N*m/rad
Weak	0.315"	0.035"	3.25	1.071	0.121007	0.135"	0.077035
Intermediate	0.309"	0.040"	4.25	1.473	0.166427	0.198"	0.10595
Strong	0.357"	0.045"	4.25	2.143	0.242126	0.259"	0.154142

The ODE is solved using a MATLAB solver ode45 with relative tolerance 1e-6. The snap shut starts with initial condition (t =0) at deflection angle around 100˚ and stops

at deflection angle around 25˚, during which the driven torque is not zero. The ODE results for 3D printed white strong flexible plastic dactyl with varying torsion springs are illustrated in Figure 13. These range of velocities are comparable to those from the real shrimp, and should lead to similar cavitation phenomena.

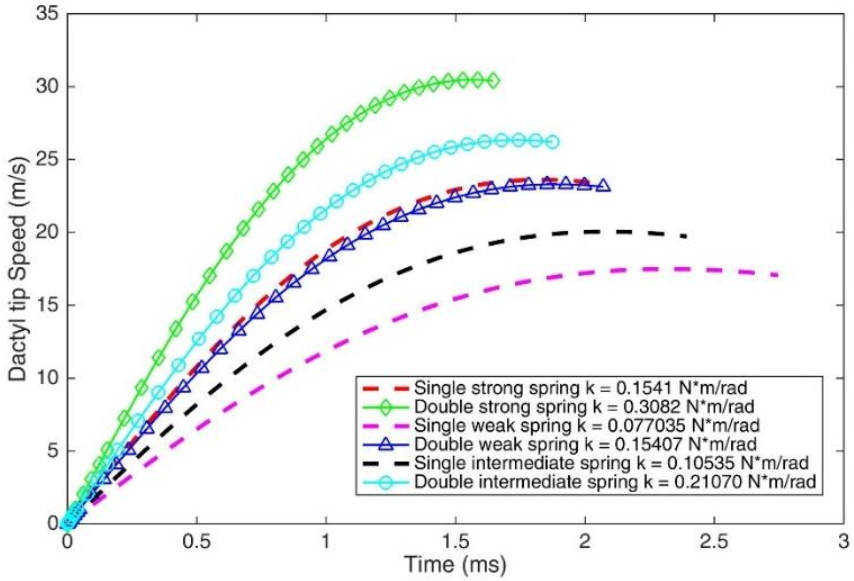

Figure 13 Dactyl tip speed with white strong plastic material for Cd = 0.5 (*12*)

Additive manufacturing (AM) which is also known as 3D Printing was utilized to print out the complex geometry of the bioinspired snapper claw. Majority of the 3D printed parts were ordered on Shapeways Inc., a 3D printing service company, including the dactyl and propus, together with the clutch. The materials for printing those parts was 'white strong flexible plastic' chosen for its strength and low moment of inertia. Machined parts, the springs, and ball bearings completed the assembly. A comparison of CAD model with manufactured bionic device can be seen in Figure 14. The spring was removed from the

assembly in Figure 14b because accidental snapping of the claw in air will destroy it, however, this does not happen in water due to additional drag.

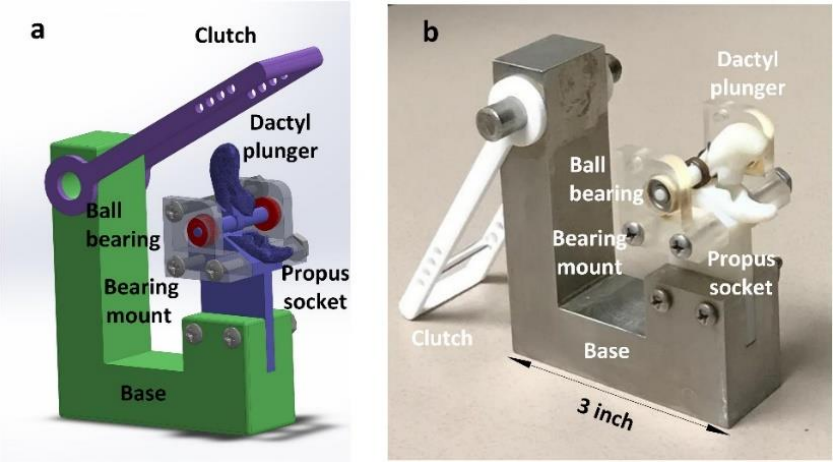

Figure 14 Comparison of CAD model and actual bioinspired device (*12*)
(a) CAD model and (b) manufactured bioinspired device

The shrimp's snapper claw releasing angle at cocked position was hard to trace due the fragile nature of the molt during μ-CT scan. Based on the open claw scan data, the dactyl plunger molt part was already damaged and detached from one side of the joint as demonstrated in Figure 15. Therefore the releasing angle of the device worth exploring.

In the CAD design of the clutch releasing version, there are four rod position placed on the clutch for different cock positions of the dactyl plunger. However, these cocked angles are different from the releasing angle due to the deformation of the clutch rod as well as the 'hook' shape dactyl of the complex surface morphology. The actual releasing angle can be estimated from the high frame rate videos.

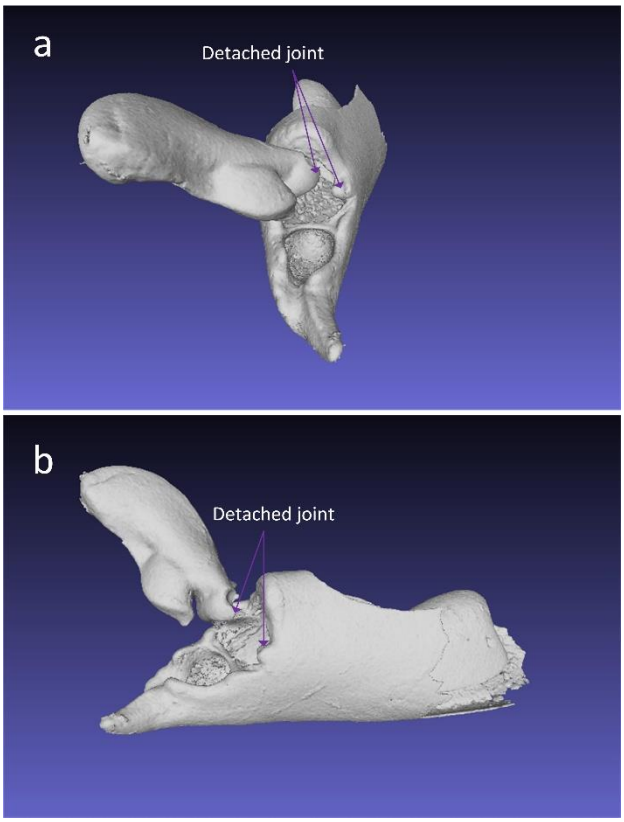

Figure 15 Open claw scan detached joint between plunger and the immobile propus
(a) Detached joint of snapper claw mesh front view. (b) Detached joint side view

3.4. Summary

Before the morphologically accurate snapper claw geometry of the striped snapping shrimp was acquired from μ-CT scan, a 2D mid-plane profile of the *Alpheus bellulus* snapper claw from David Hess article (*148*) was employed to design a similar clutch version device which did not work out successfully with dactyl plunger back cavitation and several small cavitation bubble attached to the plunger bottom surface at the end of the snap due to impact force, similar to water hammer device, no jet-induced cavitation was observed. This failure step addressed the prominent function of the snapper

claw morphology due to the three dimensional fluid dynamics complexity for cavitation formation and high-speed water jet issuance from the socket.

Pivoted from the failed design, the streamlined dactyl plunger was targeted. The streamline snapper claw shape reduces the fluid drag and therefore improve the rate of plunger expelling water out of the socket which results in high-speed water jet formation. Simple Bernoulli's principle just like what happened in the Venturi tube throat, however, the trick of making the Bernoulli’s principle work and generate a solitary cavitation not adjacent to a wall is quite challenging.

4. CAVITATION BUBBLE DYNAMICS AND UNDERWATER SHOCK WAVE*

> The sound emitted by an individual shrimp is a single sharp "snap" or "crack" produced only occasionally. It is the combined snapping of the members of a large population that results in a continuous loud under water crackle.
>
> --- Underwater Noise Caused by Snapping Shrimp (*158*)

It was only until the year 2000, the secret of the snapping shrimp noise was unveiled by Dr. Lohse's group with high frame rate videography (40500 fps) (*10*). The whole snapping process of a typical *A. heterochaelis*, the bigclaw snapping shrimp, is approximately 600 μs, and the time between shrimp cavitation initiation and the first collapse (first singularity) is around 650 μs. Both processes are hard to be observed by human eyes. Therefore, the high frame rate videography technique was utilized to investigate the cavitation evolution process, as known as the bubble dynamics of the cavitation. The schlieren imaging technique enable the direct observation of underwater shock waves generated during the cavitation collapsing process. The shock wave image captured by multiple exposure mode of an ICCD camera is also a direct visual evidence of where the snapping sound come from.

4.1. High Frame Rate Video Investigation on Bioinspired Device

4.1.1. Experiment Setup

High frame rate video experiment setup is shown in Figure 16, the Photron SA5 CMOS camera was placed to record the side view of the water jet channel of the bioinspired device in water tank. For access to top view, a mirror placed at 45° angle relative to the optical table can be set up together with a half immersed clear acrylic plate to avoid water ripples on the water air interface inside the water tank. Two lenses were used including a NIKON AF Nikkor 50mm f/1.8D lens and a Micro-NIKKOR 105 mm lens for large and small field of view experiment. The focal length of the camera lens was generally set at the minimum (magnification at maximum) and high frame rate camera was adjusted to the position where a clear image of bioinspired device can be observed in the region of interest (ROI). In this way, the camera will capture the maximum information with high resolution at specific frame rate from the ROI.

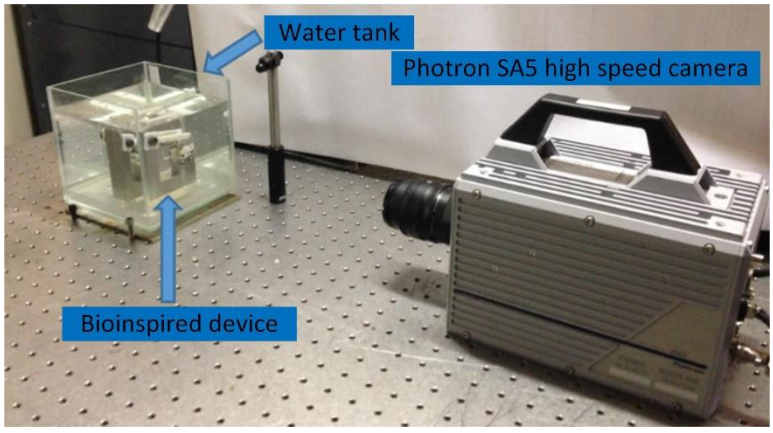

Figure 16 High frame rate video experiment setup for side view

High frame rate videography of the bio-inspired device in operation underwater was taken using a high frame rate camera (Photron, FASTCAM SA5), capable of one million frames per second (fps). This camera was used to estimate dactyl tip speed and to image cavitation evolution, at a frame rate of 60,000 fps.

4.1.2. The Effect of Different Torsion Spring Combinations

4.1.2.1. Closure time of the snapper claw

There were several options for driving torque choices due to the torsion spring parameters for the bioinspired device, which works better on cavitation generation under certain driving toque with various torsion spring combinations. The impulsive snap shut of the mechanical device is critical for generating the non-spherical cavitation. The typical snapper claw closure time for different snapping shrimp species varies, even the same shrimp may have different closure time from snap to snap due to jitter in muscle strength or other internal biological spring mechanism. The big claw snapping shrimp, *Alpheus heterochaelis*, dactyl closure time from its cocked position was approximately 0.6 millisecond (ms) according to the high-speed video images in literature (*10*). And the typical closure time for *Alpheus bellulus* was 0.5 ms reported by Hess et al (*148*). Based on a high frame rate video of one snap event by *Alpheus formosus*, a typical closure time was around 1.5 ms. The two frames right before and after the snap event are demonstrated in Figure 17, in which the snapper claw of shrimp A is highlighted with red circles. This video was recorded at 30,000 fps and the cavitation event was hard to be identified due to

the relatively low resolution of the zoom-in images. However, the snapper claw movement provided a rough estimation of the closure time for the snap event by *Alpheus formosus*.

The different closure time estimation for the bioinspired device is presented in Table 2 for different torsion spring combinations. Unlike other swimming animals in water and flying animals in air, the Strouhal number cannot be directly employed here to characterize the closure process for the snapping shrimp due to the unpredictable frequency of the snap event, however, the idea of vortex related cavitation in fluid mechanics could be borrowed for describing the high speed water jet induced by the shrimp's snap shut behavior. The dimensionless Strouhal number, as defined in equation (49), is widely used to demonstrate propulsive efficiency in animal flight or swimming, generally peaking in the 0.2-0.4 range (*159*).

$$St = \frac{fL}{U} = \frac{L}{\tau U}, \tag{49}$$

where f is the stroke frequency or frequency of vortex shedding, L is the characteristic length or amplitude of oscillation, U is the flow velocity, and τ is the closure time of the snapper claw.

By replacing the frequency with reciprocal of the plunger closure time, Hess et al. (*148*) reported the Strouhal number for *Alpheus bellulus* was 0.17. In the similar manner, the Strouhal number for bigclaw snapping shrimp can be estimated, which is around 0.52 with the front end of the cavitation speed. Since the maximum jet speed for *Alpheus formosus* was unknown, the Strouhal number of the bioinspired device based on the geometry of *formosus* is approximately 0.3 for the double weak torsion spring configuration.

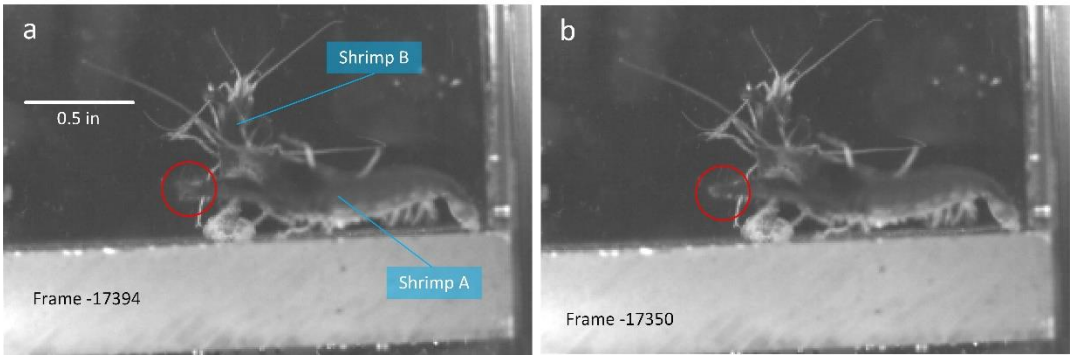

Figure 17 Alpheus formosus snapper claw closure time estimation. (a) Frame image right before the snap. (b) Frame image right after the snap. This video was recorded at 30,000 frame per second, the closure time was approximately 1.47 ms.

Table 2 Comparison of torsion springs on kinematics and cavitation generation

Spring combinations	Spring Constant [N*m/rad]	Input Energy [mJ]	R_{max} [mm]	Maximum bubble energy [mJ]	Closure time [ms]
Single 1	0.0770	102	3.17	13.2	3.08
Single 2	0.1060	140	4.05	27.5	2.67
Double 1	0.15407	204	4.68	42.5	2.43
Single 3	0.15414	204	4.58	39.8	2.05
Double 2	0.2120	280	5.24	59.7	1.97

4.1.2.2. Cavitation geometry near first singularity

For the bioinspired device, the socket volume is a fixed value, therefore the water jet generated during the snapping process differs in speed with various torsion spring combinations, which also resulted in the various size of cavitations. The maximum cavitation volume frames recorded in high speed videos are illustrated in Figure 18. The listed sequence is the same as shown in Table 2. For simplification purpose, the weak, intermediate, and strong torsion springs are represented by torsion spring 1, 2, and 3 respectively. For the single 1 torsion spring case, as shown in Figure 18a and b, the plunger

moving plane was rotated 25° counterclockwise along the vertical axis to ensure the water jet was only moving in the side view plane. Other torsion spring combination cases still utilized rotating plunger plane as the side view plane. With the increasing torsion spring constant, the jet-induced cavitation peak volume also increased, together with the plunger back cavitation.

Besides the maximum cavitation volumes, the first singularity cavitation geometry are also critical for the energy focusing process. The shock waves generated from non-spherical cavitation bubbles are multiple shock waves associated with different processes such as the jet impact and the individual collapses of the various separated parts of the bubble (*160*). The non-spherical geometry of cavitations induced by the bioinspired device are complicated to be quantified compared to cavitation generated by other methods like laser-induced ones. The correlation between the non-spherical cavitation collapse and the peak pressure during the collapse is not in the scope of this dissertation.

For those frames near cavitation first singularity shown in Figure 18, the case single 1 and case single 2 cavitation volumes were smaller compared to other cases, and the plunger back cavitation effects in single 1 and single 2 cases were negligible according to Figure 18a and c. In case double 1, single 3 and double 2, the maximum cavitation volumes were bigger than those in single 1 and single 2, however, the plunger back cavitations effects were also more intense. Especially for case double 2, the plunger back cavitation was more intense than the jet-induced cavitation, considering both the volume and the oscillating cavitation lifetime.

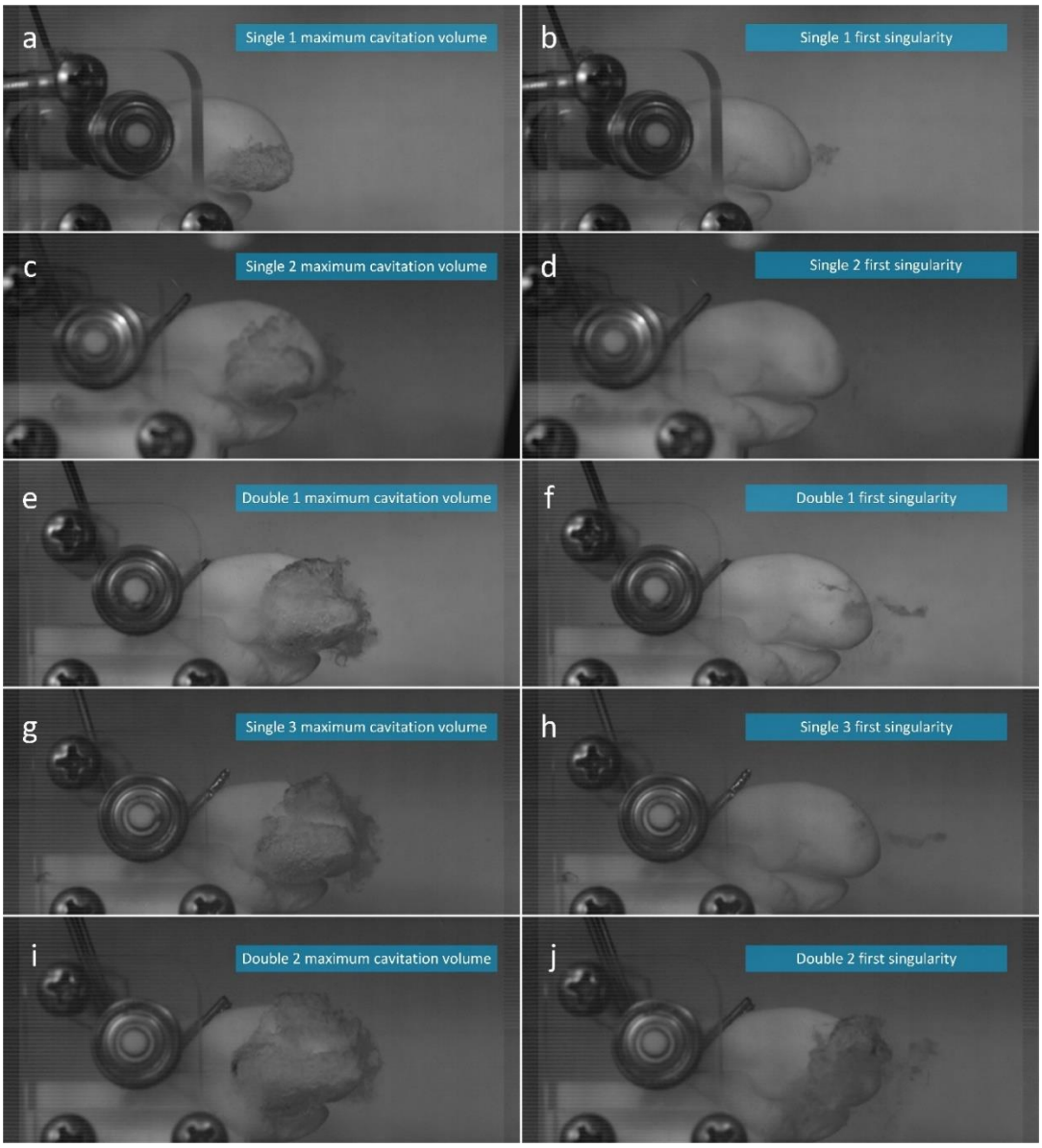

Figure 18 Maximum cavitation volume and the first singularities for different torsion spring combinations. (a), (c), (e), (g), (i) are maximum volume of cavitations for single 1, single 2, double 1, single 3 and double 2 torsion springs, which are listed according to torsion spring constants. (b), (d), (f), (h), (j) are the cavitation geometry near first singularities for each case.

In order to obtain a better idea of the aforementioned cavitation geometry near singularity, 8 frames near first singularity are compared for the four typical cases shown

from Figure 19 to Figure 22. As shown in Figure 19, the plunger back cavitation already disappeared before -0.05 ms for single 2 case, there was only hydrodynamic water jet induced cavitation spotted in the 8 frames near first singularity. However, plunger back cavitation were observed in other cases like double 1, single 3, and double 2. The difference among them are the position and the intensity of the back plunger cavitation.

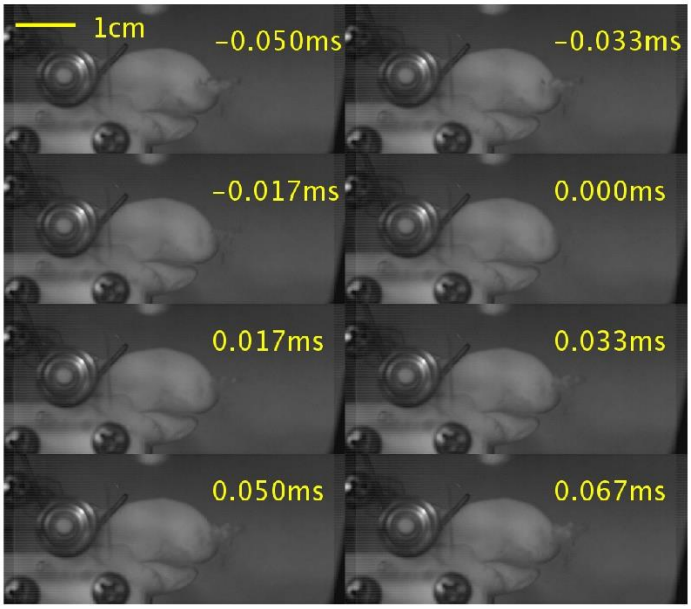

Figure 19 High frame rate video frames near first singularity for Single 2 case

For double 1 case presented in Figure 20, the plunger back cavitation collapsing spot was distinguishable from the major jet-induced one. Due to larger torsion spring constant and smaller moment of inertia compared to double 1 torsion spring configuration, the single 3 case plunger back cavitation was spotted at the left end of the major cavitation site, it was hard to distinguish those two apart since they were overlapping from side view video frames illustrated in Figure 21. Essentially, the two cavitation sites were spatially apart from each other since the high speed water jet ejected from the socket channel at an

angle around 25°. Another interesting phenomena was that the geometry of the cavitation near first singularity in case single 3 was a long cylinder shape before the singularity and after the rebound with similar orientation of the long axis. On the contrary, the long axis of the major ellipsoidal cavitation in double 1 case rotated clockwise after the rebound. This interesting comparison was caused by the hydraulic instabilities of the cavitation gas and liquid interface, and also the cavitation wall velocity variation at different orientations.

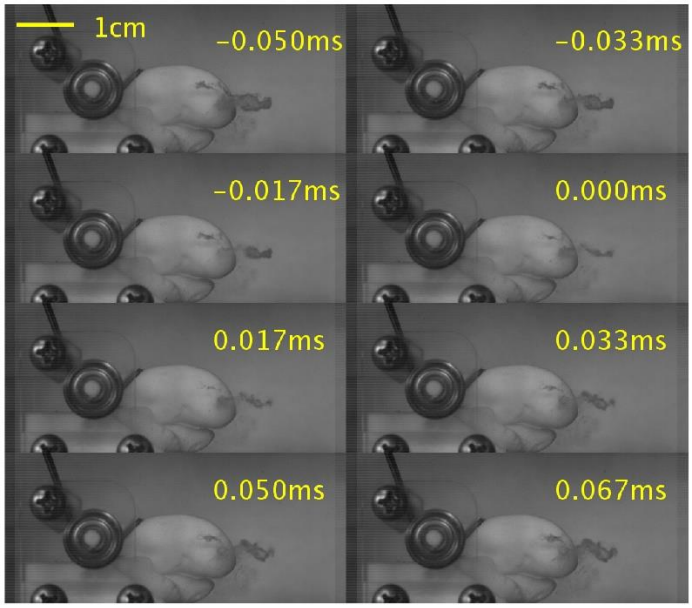

Figure 20 High frame rate video frames near first singularity for double 1 case

When the spring constant increased above certain value, the plunger back cavitation will eventually outperform the jet-induced major cavitation, this can be seen in the 8 frames of high frame rate videos in Figure 22. The size of the plunger back cavitation were larger throughout the 0.117 ms depicted in the 8 frames compared to the jet-induced one.

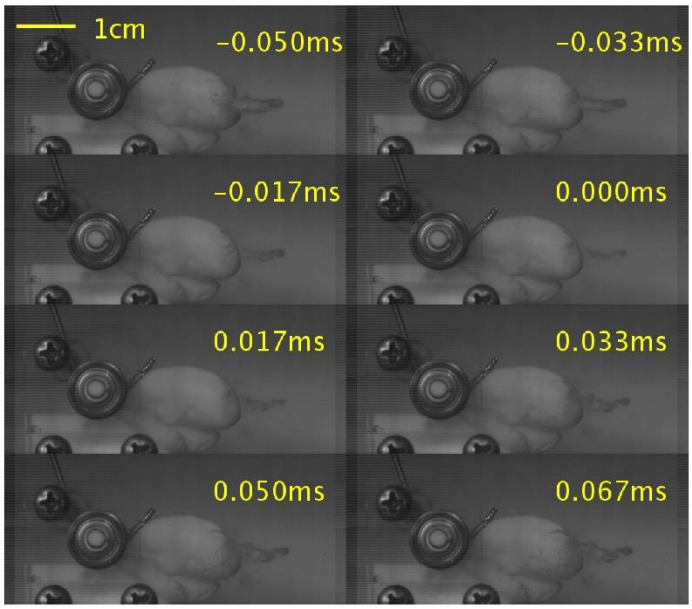

Figure 21 High frame rate video frames near first singularity for Single 3 case

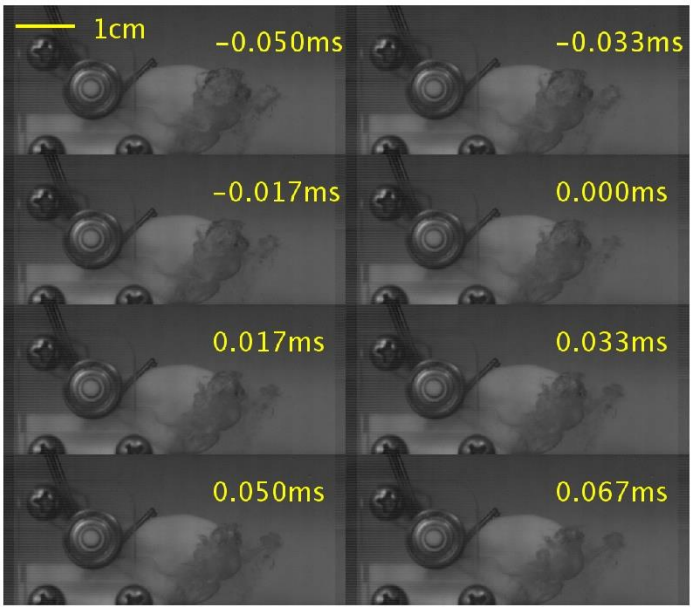

Figure 22 High frame video frames near first singularity for double 2 case

In summary, the driving torque is not 'the larger the better' for jet-induced cavitation generation process due to the influence of the plunger back cavitation. There

are certain driving torque range will benefit the bioinspired device which in turn indicates that the snapping shrimp also need a tailored range of rotating torque for the snapper claw to generate more powerful collapsing cavitation.

Judging by the maximum size (maximum volumetric equivalent radius) of the jet-induced major cavitation and the effects of the plunger back cavitation, the double 1 case has the potential to produce more intense collapsing cavitation which is critical for plasma generation. Therefore, the double weak torsion spring configuration was chosen for underwater shock wave investigation and light emission detection experiments.

4.1.3. Different Releasing Angle

4.1.3.1. Single weak torsion spring configuration

As aforementioned in the bioinspired design section, the cocked angle of the actual shrimp was not recorded. Despite of this, the releasing angles, the angle when the plunger detach from the clutch, play important roles for cavitation generation. The four series of near first singularity video stills recorded with single weak torsion spring configuration for various releasing angles are exhibited in Figure 23 to Figure 26. Four angles were tested based on the original clutch rod position design. Angle 1 to 4 are 47.0°, 64.4°, 81.5°, and 95.1° respectively.

All four cases with single 1 torsion spring did not show back plunger cavitation interference, displaying only one major cavitation collapsing site induced by the high-speed water jet with an angle around 20° between the jet and the plunger rotation plane. This angle differs from that of double 1 torsion spring configuration due to different fitting

clearance. The clearance change can be caused from three major contributions a) the spring preload which will push the dactyl plunger shaft forward; b) modifications conducted for fitting purpose; c) 3D printing quality for different material as well as wear developed from snap to snap.

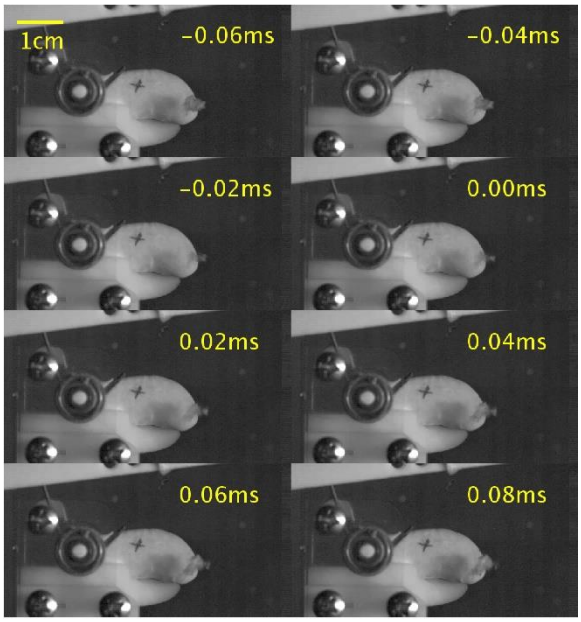

Figure 23 High frame rate video frames near first singularity for single 1 angle 1
(video taken at 50,000 fps and the releasing angle 47.0°)

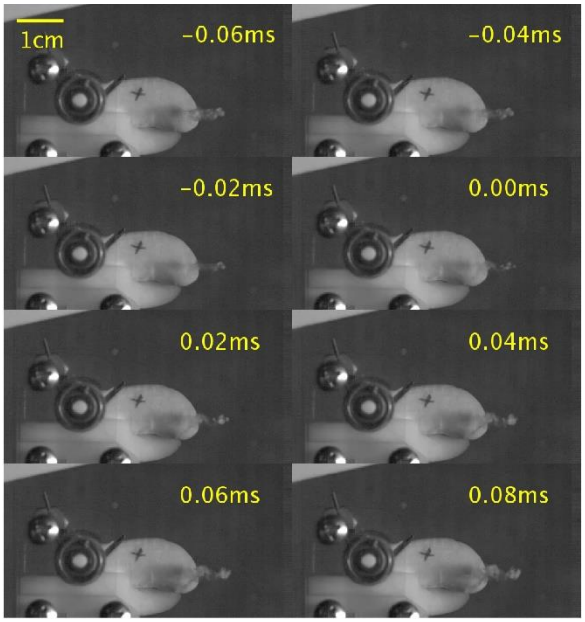

Figure 24 High frame rate video frames near first singularity for single 1 angle 2
(video taken at 50,000 fps and the releasing angle 64.4°)

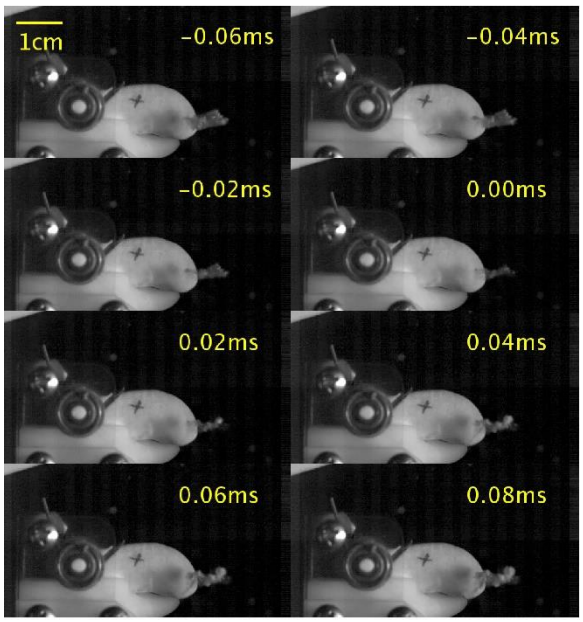

Figure 25 High frame rate video frames near first singularity for single 1 angle 3
(video taken at 50,000 fps and the releasing angle 81.5°)

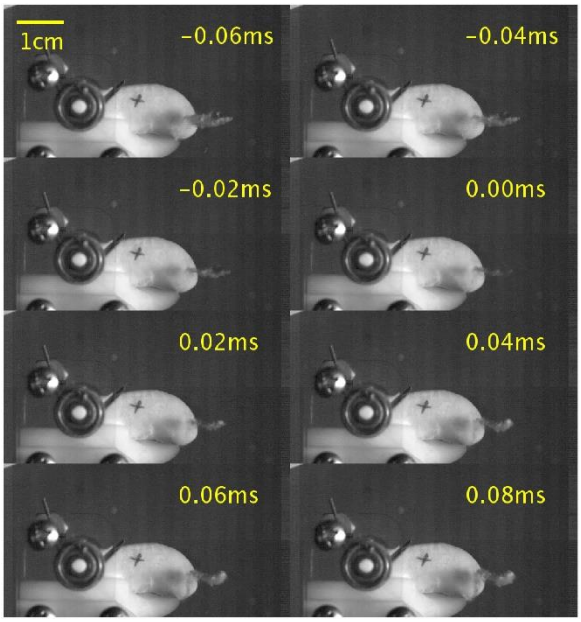

Figure 26 High frame rate video frames near first singularity for single 1 angle 4
(video taken at 50,000 fps and the releasing angle 95.1°)

Based on those video stills near first singularity, none of them were spherical collapsing cavitation, and the corresponding collapsing site moves further away with the increasing releasing angle. The releasing angle 1 case was totally free from back plunger cavitation caused by plunger rotation. The back plunger cavitations though were spotted in other releasing angle cases. Therefore, the single 1 angle 1 condition can generate a solitary single cavitation bubble, this is actually the regime that the snapping shrimp achieved.

Even though other releasing angle cases had back plunger cavitation observed, they had a better maximum cavitation volume, which can issue stronger shock waves and light emissions. The shock waves as known as the source of the underwater noise level can be distinguished rather directly with human hearing, no need utilizing a hydrophone

monitoring to the difference. The noise level was directly correlated with the maximum cavitation volume.

4.1.3.2. Double weak torsion spring configuration

With double weak torsion spring setup, all four releasing angles of dactyl plunger operation were spotted with cavitation near the dactyl surface. The interference of dactyl induced cavitation were not recorded near the first singularity of the major cavitation induced by high speed water jet, as illustrated in Figure 27 to Figure 29. Angle 1 to angle 3 cases were similar to their counterpart in single weak torsion spring, with the value of 47.1°, 68.1°**,** and 79.0° respectively. In angle 4 case as shown in Figure 30, both cavitation sites during first singularity were recorded, indicating strong interference.

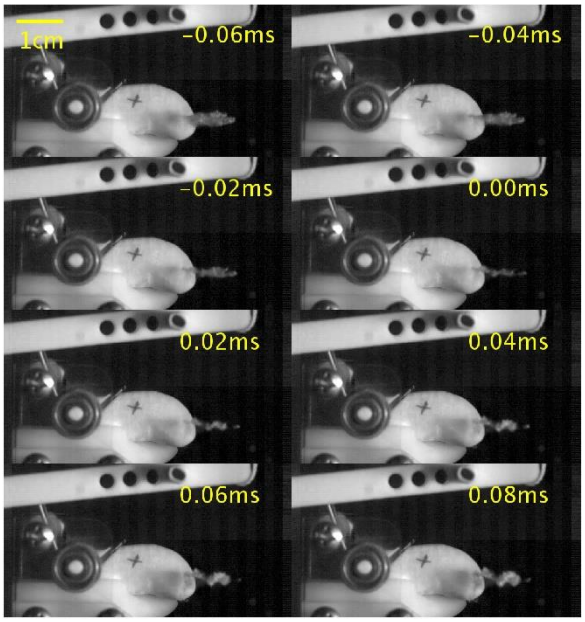

Figure 27 High frame rate video frames near first singularity for double 1 angle 1 (video taken at 50,000 fps and the releasing angle 47.1°)

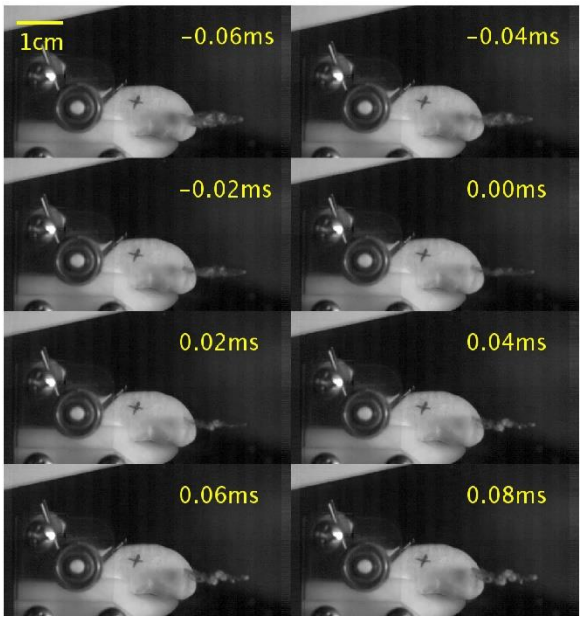

Figure 28 High frame rate video frames near first singularity for double 1 angle 2
(video taken at 50,000 fps and the releasing angle 64.8°)

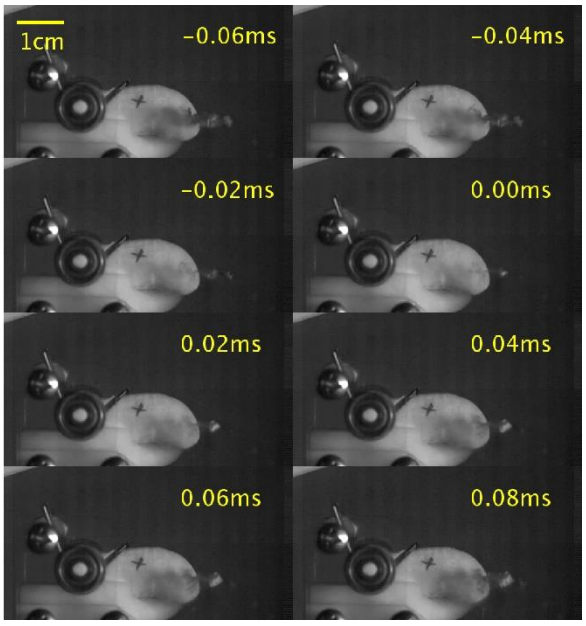

Figure 29 High frame rate video frames near first singularity for double 1 angle 3
(video taken at 50,000 fps and the releasing angle 79.0°)

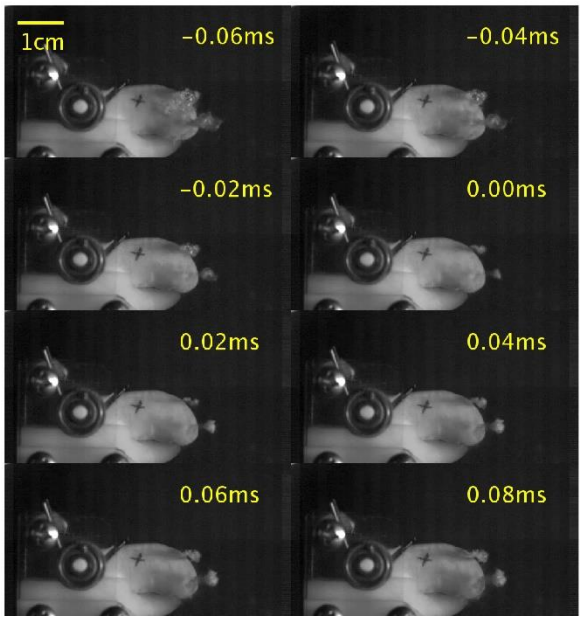

Figure 30 High frame rate video frames near first singularity for double 1 angle 4
(video taken at 50,000 fps and the releasing angle 92.0°)

Releasing angle 1 case only had small dactyl cavitation on the side of dactyl part during snap operation, which disappeared ~1.1 ms before the major cavitation bubble reached the minimum volume. For angle 2 to 3 cases, the two cavitation sites collapsed in sequence with dactyl back cavitation leading about 0.16 ms and 0.02 ms accordingly. The shockwave generated during the leading event affected the volume of the jet-induced cavitation. Whereas the angle 4 case, jet-induced cavitation took the lead approximately 0.02 ms (for 50,000 fps, this is only one frame difference) near the first singularity event. However, the dactyl back cavitation volume shrunk to a small rotating vortex cavitation first without completely collapse and became large again later collapsed one frame after the jet-induce one.

In sum, whether the shrimp has a best cocking angle for shooting out destructive collapsing cavitation is still unknown, whereas best angle definitely exits for the bioinspired mechanical device. Considering different aspects such as the maximum cavitation bubble volume with different torsion spring choice and releasing angle option, the double weak torsion spring configuration at angle 2 seems more promising to produce a strong cavitation collapsing event though observed with some dactyl-induced side cavitation interference. The single solitary cavitation regime seems to fit into the parameter scope in which snapping shrimp operating their snapper claw, however, for the scale-up design, this single cavitation collapsing regime was not powerful compared to other cases. For the shrimp-inspired device, there is definitely a choice of an angle that outperformed others. And double 1 torsion spring at angle 2 case is the amenable condition with strong collapsing behavior to explore the cavitation luminescence phenomenon.

4.1.4. Bubble Dynamics and Water Jet Speed for Double 1 Angle 2 case

A series of selected high frame rate video imaging stills of the rotating dactyl driven by two weak torsion springs with front-lit are shown in Figure 31 to illustrate claw operation. Two major cavitation sites were spotted: one from the water jet and the second along the tip of the claw. This led to one implosion singularity site at the surface of the dactyl and another one located at a distance from the dactyl, generated by the high-speed water jet. Additionally, cavitation formed around the narrow area between socket edge and plunger side surface helped confined the water and push the remaining water out of the nozzle shaped channel forming a high-speed water jet. The cavitation generated by the

high-speed jet is ellipsoidal and oscillatory in time. Since the non-spherical cavitation volume was difficult to estimate accurately, an effective radius, was approximated by assuming a volumetric equivalent ellipsoidal cavitation with major and minor axes measured from the video. By comparing multiple trials of top view and side view videos, the two minor axes b and c as shown in Figure 32 were almost equivalent, thus the two minor axes were assumed to be equal for effective radius estimation.

Based on three trials of side view videos, the bubble dynamics using volumetric effective radius is illustrated in Figure 33. The cavitation conversion efficiency, which can be defined as ratio between cavitation mechanical energy at its maximum volume over input torsion spring potential energy at releasing state, was around 20%. The details of the efficiency calculation and discussion will be discussed in later chapter.

The dactyl dynamics ODE model was used to make comparison to experimental video data obtained via feature tracking. A black cross was drawn manually on the surface of the dactyl plunger part as feature tracking target. Figure 34a highlights this comparison. According to experimental data, the maximum speed of the dactyl tip was 20.9 ± 2.6 m/s, the duration of sweep was approximately 1.5 ms, and the stopping time was 1.2 ms. The cavitation front propagation speed can be used as a close estimation for water jet speed, shown in Figure 34b. With a maximum cavitation front speed of 25.6~37.4 m/s, this implies Reynolds numbers of $0.84\sim1.23\times10^5$ and a cavitation number of $\sigma = 0.14\sim0.30$, which are comparable to the real shrimp (*10*).

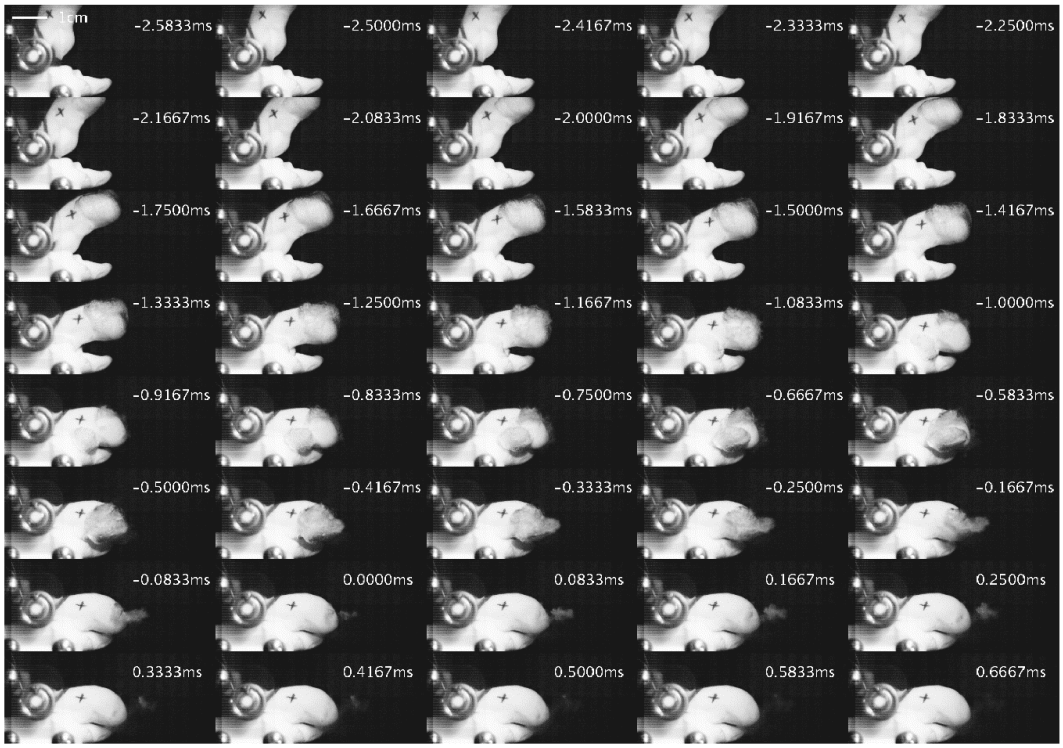

Figure 31 Selected high frame rate video frames during device operation with double weak torsion spring configuration, emphasizing cavitation evolution.
Recorded at 60,000 fps with t=0.000 ms corresponding to the first singularity.

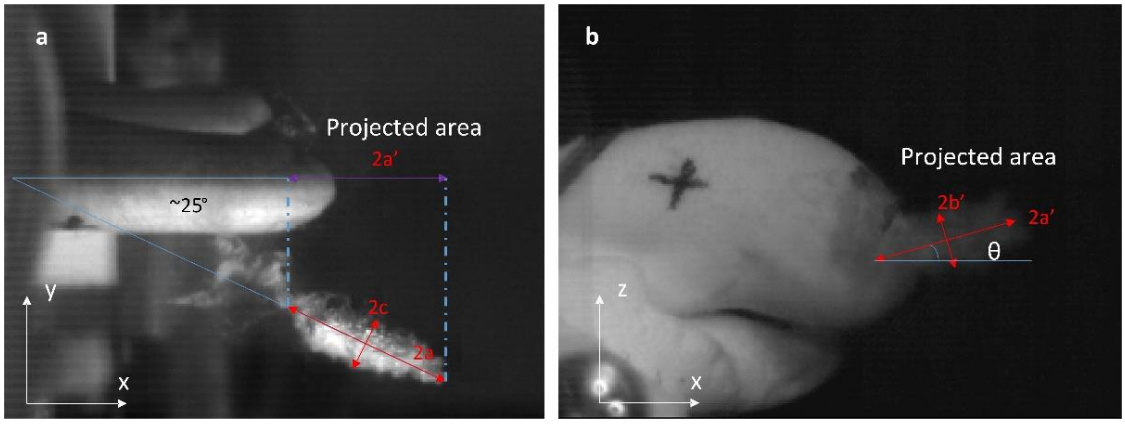

Figure 32 Effective radius estimation for ellipsoidal cavitation
(a) top view (b) side view

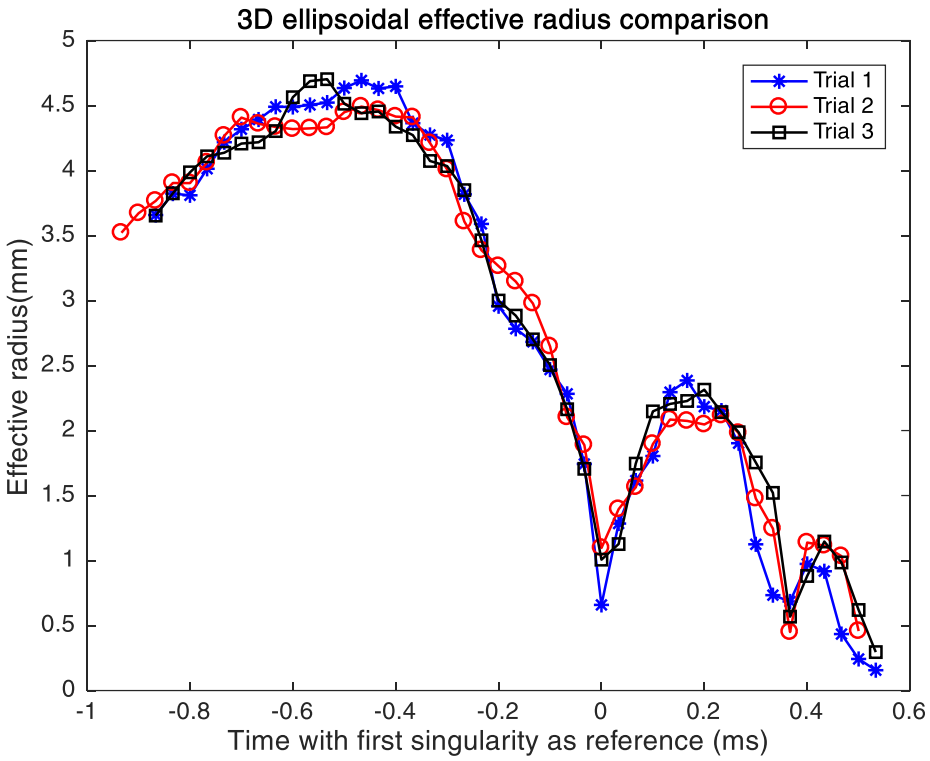

Figure 33 Cavitation bubble dynamics (*12*). Plot of effective radius over time for three different trials.

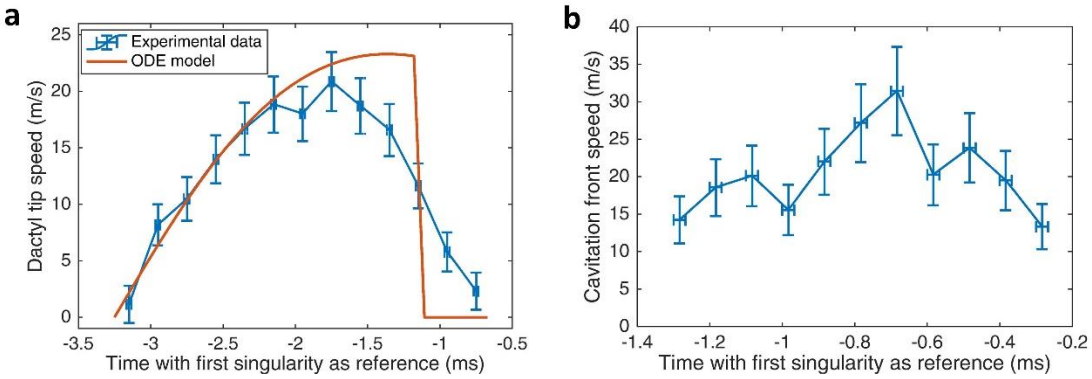

Figure 34 Dactyl tip speed and cavitation front speed (*12*)
(a) Comparison of device dactyl tip speed experimental data with the numerical model result, (b) Cavitation front speed estimation.

4.1.5. Uncertainty Analysis

The bioinspired device dactyl tip speed was estimated by equation (50),

$$V = \frac{d_o}{D_o}\frac{R_1}{R_2}\frac{D}{\Delta t} = \frac{d_o}{D_o}\frac{R_1}{R_2}\frac{\|\overrightarrow{x_1} - \overrightarrow{x_2}\|}{\Delta t}, \tag{50}$$

where d_o is the calibration bar actual distance, D_o is the calibration bar length in pixels, R_1 is the radius of the dactyl tip to the pivot axis in pixels, R_2 is the radius of the tracking point to the pivot axis in pixels, D is the tracking point pixel distance between two different video frames, Δt is the time difference between the two different video frames, and $\overrightarrow{x_1}$, $\overrightarrow{x_2}$ are the tracking point positions vector relative to pivot axis in the two video frames.

The uncertainty analysis for the dactyl tip speed was estimated by using the differential method (*161*, *162*) for single-sample experiments. Since the dactyl tip speed is a linear function of seven independent variables, the equation (51) as referred as the second power equation can be used directly as an approximation for calculating the uncertainty interval in the result.

$$\frac{W_v}{v} \tag{51}$$

$$= \sqrt{\left(\frac{W_{d_o}}{d_o}\right)^2 + \left(\frac{W_{D_o}}{D_o}\right)^2 + \left(\frac{W_{R_1}}{R_1}\right)^2 + \left(\frac{W_{R_2}}{R_2}\right)^2 + 2\left(\frac{W_{\vec{x}}}{\|\overrightarrow{x_1} - \overrightarrow{x_2}\|}\right)^2 + \left(\frac{W_{\Delta t}}{\Delta t}\right)^2}$$

In which W_v is the uncertainty of dactyl tip speed, W_{d_o} is the uncertainty of calibration bar distance (W_{d_o}=1 mm), W_{D_o} is the uncertainty of calibration bar length in pixels (W_{D_o}= 1 pixel), W_{R_1} and W_{R_2} are uncertainties for radius R_1 and R_2, $W_{\vec{x}}$ is the uncertainty of tracking point position vector, and $W_{\Delta t}$ is the uncertainty of time.

The cavitation front speed uncertainty was calculated in the similar method with one more nonlinear independent variable, the angle between the dactyl rotation plane and the water jet angle. Since the cosine relation of the angle is nonlinear, the error bars were estimated by considering both the upper bound and the lower bound for this nonlinear term.

4.2. Schlieren Imaging of Underwater Shock Wave

Snapping shrimps are special contributors of underwater noise throughout the world's tropical and subtropical shallow waters in the ocean (*158*, *163*), since shockwaves are generated during their snaps of the snapper claws. Schlieren imaging technique will help to unveil the detail of the shockwave generation and propagation.

4.2.1. Experimental Setup

The experimental setup is a popular Z-type 2-mirror Herschellian schlieren system arrangement (*164*) which is illustrated in Figure 35. The illumination source is a continuous wave (CW) Diode pumped solid state (DPSS) class IIIb laser (300 mW, Changchun New Industries Optoelectronics Tech. Co. Ltd, China), emitting light with a wavelength of 532 nm. The laser beam is then expanded to a larger diameter beam through a combination of plano-convex and a plano-concave lenses and collimated by the 1st parabolic mirror. The collimated laser light is then reflected and refocused by the 2nd parabolic mirror and cut off by a vertical knife-edge, which is a ubiquitous razor coated

with black paint. The vertical cut-off will enable the observation of the horizontal gradient of the refraction index in the test section.

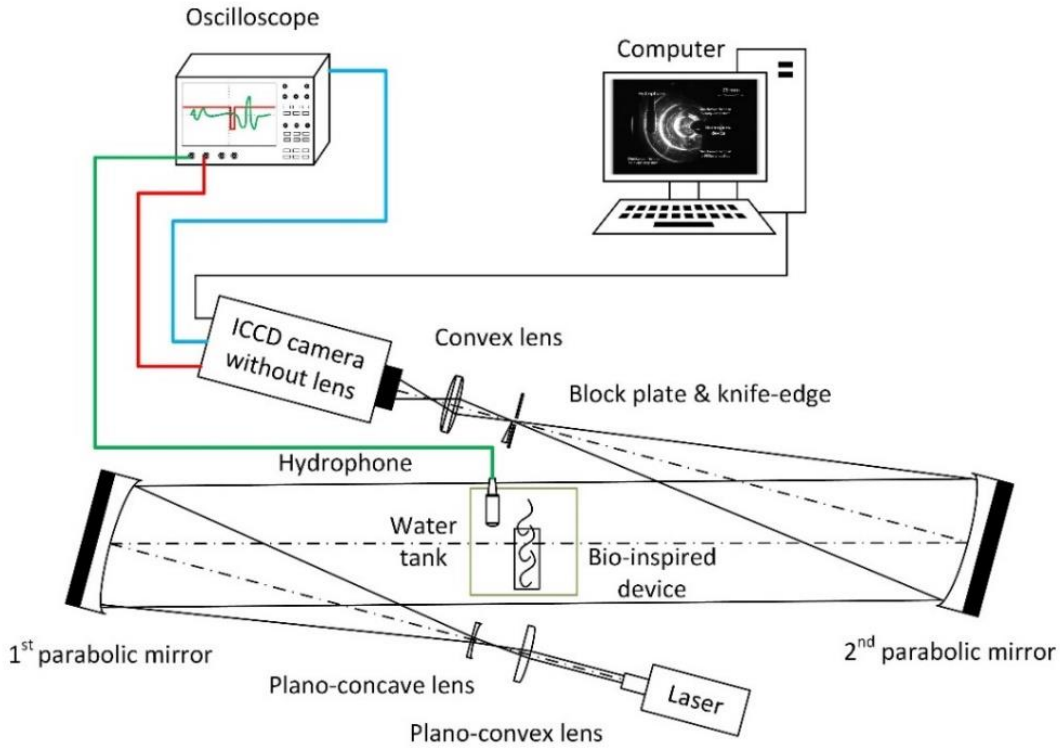

Figure 35 Schematic diagram of the Z-type schlieren imaging setup (*12*)

An aluminum plate with a 0.25 inch hole is placed right before the knife-edge to let through the refocused laser light and block other diffracted and reflected stray light. Only a single convex lens is placed after the knife-edge cut-off for enlarging the image size captured by the ICCD camera with minimal light loss. A 4 Picos ICCD camera, Stanford Computer Optics Inc., is used in multi-exposed mode to capture the schlieren photograph of shockwave propagation, and the underwater pressure signals is monitored by a Teledyne RESON hydrophone, TC 4013, 170 kHz. A multi-exposure mode allows for multiple images from a single snap and are reordered by re-exposing the ICCD without

clearing it. In this case typically 100ns exposures were spaced by 10 or 20 μs. Effectively this gives information at both high resolution and high frame rate. An oscilloscope (WaveRunner 204MXi 2 GHz), produced by Teledyne LeCroy company, is utilized to monitor hydrophone signal for triggering the ICCD camera by manually setting the trigger voltage level on hydrophone signal channel. ICCD camera will also send its gated exposure signal to the oscilloscope showing the timing of shutter operation, delay time after trigger and exposure time. The ICCD internal delay between the trigger and the shutter of the camera is around 65 ns.

4.2.2. Schlieren Imaging of Underwater Shock Wave

Four multi-exposed images of a propagating shockwave generated by bioinspired device with two weak torsion springs and their corresponding hydrophone and ICCD camera signals recorded by the oscilloscope are presented in Figure 14.

In Figure 36(a), three exposures demonstrated the expanding shock front generated by the first singularity of collapsing cavitation. Expansion of the cavitation after the first singularity was also spotted near the tip of the bioinspired snapper claw. The distance between hydrophone and the claw tip is around 32.36 mm, and it takes approximately 15.7 μs for the first singularity shock front to approach to the hydrophone from the cavitation site. Three-exposed schlieren image have exposure times of 100 ns, and the delay between images is 10 μs, which can be seen in the bottom part zoom-in view of the oscilloscope data in Figure 36(b).

For the oscilloscope signals, the upper part covered the time range from -600~1400 μs range and the zoom-in part showed the 200 μs signals around the first singularity. The first singularity is the first largest negative peak of the hydrophone signal (red). Two exposures located on the left side of first singularity and one exposure on the right side, which agreed well with the schlieren image in Figure 36(a) with the last shock front passed the hydrophone position and the other two shock fronts still on the way to hydrophone. Owning to the jitter of clutch releasing process, sometimes two or more major cavitation sites can be observed. With the same experimental condition, two major first singularities were initiated as shown in Figure 36(c). At the last exposure, the two major shock fronts divided into several shock fronts, indicating that those two major shock fronts were actually the overlapping result of several different shock fronts. This proves that the bioinspired device may create several cavitation sites with volumes at the equivalent order of magnitude. Figure 36(e), (g) exhibited two double exposed schlieren image of shock with the same exposure time and different delay time between the two exposures, which are 20 μs for (e) and 15 μs for (g).

Based on the calibrated images, the shockwave propagation speed can be estimated. The measured results are shown in

Table 3. The jitter of ICCD is 0.02 ns and the ICCD internal delay between trigger and shutter is 65 ns. The distance measurement was carried out using calibrated 25 mm scale length on hydrophone verified by caliper. The uncertainty is approximately 2.55%. The shockwave front speed is 1487.9 ± 38 m/s. The distilled water was 21 ± 0.2 ˚C when conducting the experiments.

Table 3 Measured Results of Underwater Shock Wave Propagation Speed (*12*)

Trial #	Shockwave front (inner to outer, 1=>3)	Distance between shockwaves (mm)	Speed of sound (m/s)
a	1-2	14.845	1484.5
	2-3	15.049	1504.9
	1-3	30.086	1504.3
c	1-2	14.706	1470.6
	2-3	14.939	1493.9
	1-3	29.329	1466.5
e	1-2	29.742	1487.1
g	1-2	22.368	1491.2

4.2.3. Uncertainty Analysis

The underwater shock wave propagation speed can be estimated by the following equation (52)

$$V = \frac{d_o}{D_o}\frac{D}{\Delta t}, \tag{52}$$

in which d_o is the calibration bar actual distance, D_o is the calibration bar length in pixels, D is the pixel distance between two shock wave fronts in the same multiply exposed image, Δt is the time difference between the two shock wave fronts.

The uncertainty of the underwater shock wave speed can be calculated with a 95 percent confidence interval estimated by the differential method. For equation (52), the uncertainty of the speed is given by

$$\frac{W_V}{V} = \sqrt{\left(\frac{W_{d_o}}{d_o}\right)^2 + \left(\frac{W_{D_o}}{D_o}\right)^2 + \left(\frac{W_D}{D}\right)^2 + \left(\frac{W_{\Delta t}}{\Delta t}\right)^2}. \tag{53}$$

The time uncertainty was around 0.02 ns, which was the precision of the scope at sampling rate of 10 G/s. The caliper measuring uncertainty was around 0.01 mm and the pixel

distance uncertainty was approximately were 3 pixels for both D_o and D. Therefore the relative uncertainty $\frac{W_v}{v}$ for shock wave propagation speed was around 2.67%.

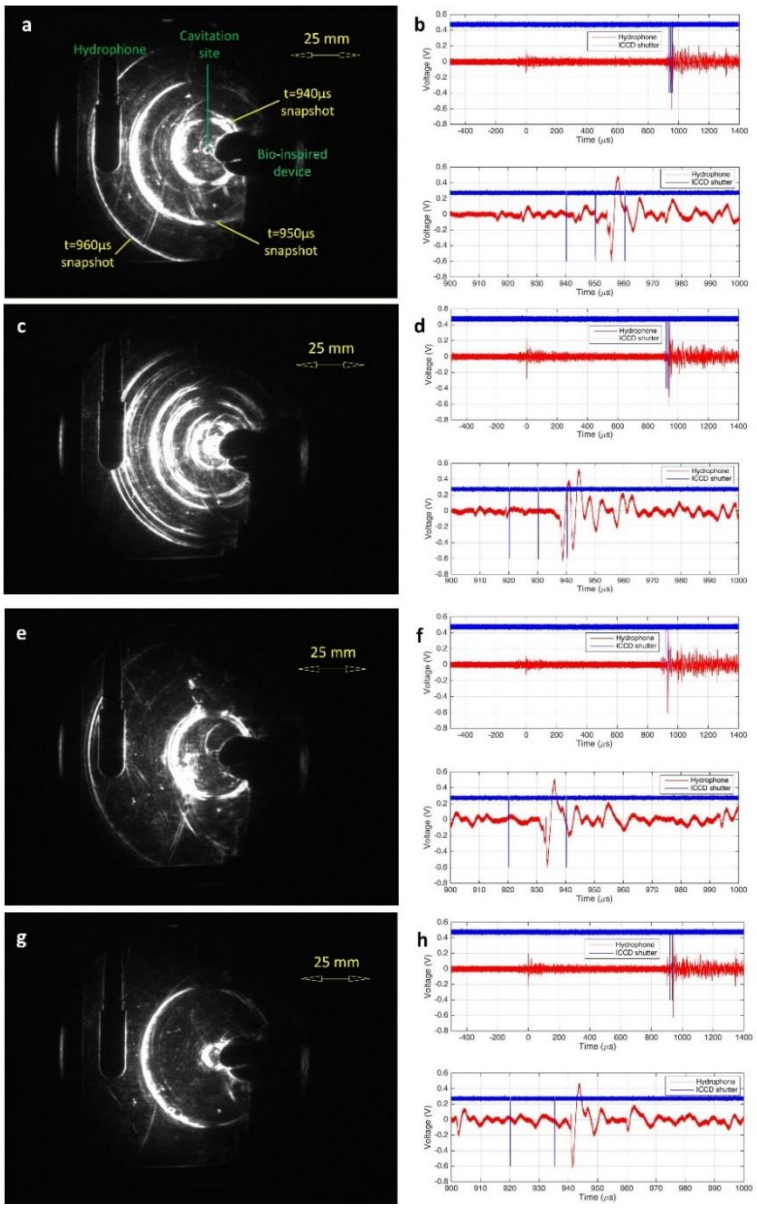

Figure 36 Schlieren images of shockwave (*12*). (a). Three-exposed image with exposure time 100 ns, delay time 10 μs; (c). Three-exposed image with exposure time 100 ns, delay time 10 μs; (e). Two-exposed image with exposure time 100 ns, delay time 20 μs; (g). Two-exposed image with exposure time 100 ns, delay time 15 μs; (b, d, f, h). Corresponding hydrophone (red) and ICCD shutter (blue) signals and zoom-in view around the first singularities.

5. BIOINSPIRED DEVICE CAVITATION LUMINESCENCE DETECTION[*]

> We have dubbed this phenomenon ‘shrimpoluminescence’— the first observation, to our knowledge, of this mode of light production in any animal— because of its apparent similarity to sonoluminescence.
>
> — Detlef Lohse (*7*)

5.1. Cavitation Luminescence

According to the brief communication to nature by Dr. Lohse’s group (*7*), there was a short, intense flash of light emitted as the cavitation collapse, indicating that extreme pressures and temperatures of at least 5000 K inside the collapsing cavitation at the point of collapse which is referred as the first singularity in this dissertation. The duration of this light emission was around 10 nanoseconds, which exceeded their experiment setup temporally resolving power. The total number of photons emitted from the flashing bubble was up to 5×10^4, which is one to two orders of magnitude less than the Single Bubble Sonoluminescence (SBSL) collapsing bubble. Therefore, the shrimpoluminescence phenomenon cannot be detected with the naked eye.

---

[*] Reprinted with permission from “Bioinspired mechanical device generates plasma in water via cavitation” by Tang, X., & Staack, D. (2019). Science advances, 5(3), eaau7765, © The Authors, some rights reserved; exclusive licensee American Association for the Advancement of Science. Distributed under a Creative Commons Attribution NonCommercial License 4.0 (CC BY-NC) http://creativecommons.org/licenses/by-nc/4.0/.

5.1.1. Experimental Setup

A 4 Picos ICCD camera, Stanford Computer Optics Inc., was used for the light emission detection, and the underwater pressure signals were monitored by the hydrophone TC 4013. The experimental setup in the darkroom for light emission detection is illustrated in Figure 37. The oscilloscope (WaveRunner 204MXi 2 GHz, 10 GS/s, produced by Teledyne LeCroy company) was used to monitor hydrophone and ICCD output signal, and trigger the ICCD camera by manually setting the trigger voltage level. A photomultiplier tube (PMT, Hamamatsu Photonics K.K., R928) was established on the opposite side of the water tank, with a plano-convex lens focusing the region of interest (ROI) into the PMT box.

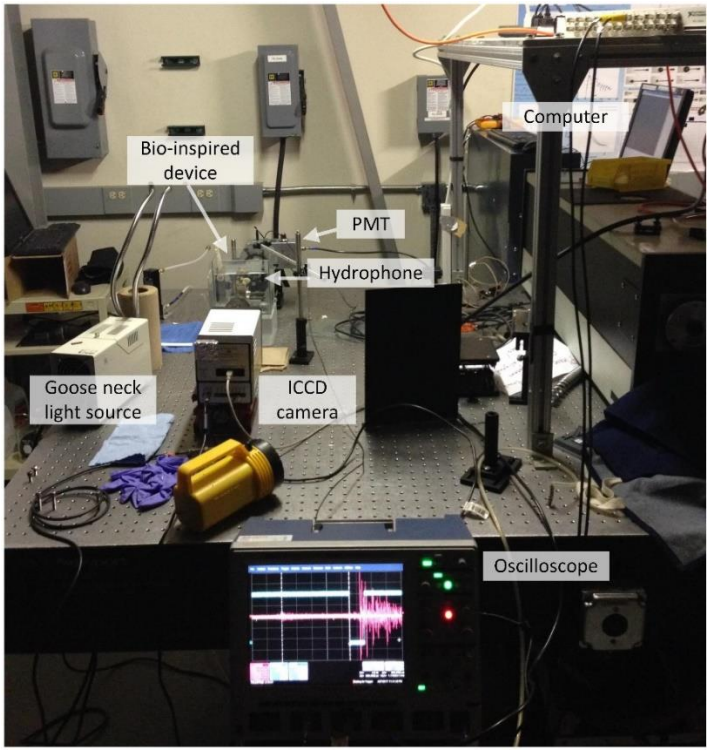

Figure 37 Light emission detection experiment setup (*12*)

Initial attempts to measure light emission from the device in distilled water using an ICCD camera did not yield conclusive results; to solve this issue argon doping (*66*) and air doping were introduced to promote light emission.

Before carrying out light emission detection experiments, compressed air or argon was doped into the water tank via a bubbling disk for 20 to 30 min to ensure that the solubility of air or argon in the water tank was saturated. In order to verify the consistency of the bio-inspired device and identify region of interest, several 1360-by-1024-pixel 12-bit images were taken of the bio-inspired device during operation in distilled water using an ICCD camera with a hydrophone trigger located 5 cm away from the cavitation region, at various delay times as shown in Figure 38. The major cavitation singularity site location appeared to vary by ±3 mm from snap to snap. The hydrophone signal which triggered the camera was caused by sound from the manual clutch release, and was therefore prone to jitter. To address this jitter, a relatively long exposure time of 20 μs was used to image the first singularity.

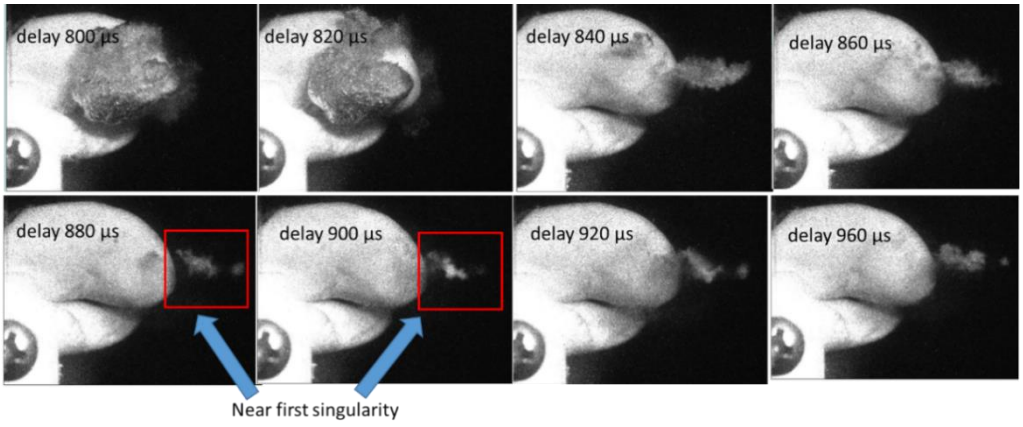

Figure 38 Cavitation sites captured by ICCD camera with varying delay time at 20μs exposure for double weak torsion spring configuration (*12*)

5.2. Light emission detection for saline water with air doping

5.2.1. Light emission results

Saline water (35,000 ppm NaCl) was used to simulate the snapping shrimp's living condition in the ocean. In order to determine the timescale of the light emission process, a photomultiplier tube (PMT) was set up on the opposite side of the water tank to measure ns-timescale light emission in parallel with the ICCD camera (Figure 37). To reduce background noise, all light sources in the laboratory dark room were turned off or blocked. Twenty hydrophone-triggered images were taken, then the location of all pixels with an intensity significantly above background were cataloged; a probability distribution histogram of average above-threshold pixel intensities is shown in Figure 39a. The location of these above-threshold pixels (corresponding to cavitation luminescence sites) are presented in Figure 39b, superimposed on a reference image to show the consistency of the first singularity position. The chosen detection threshold is nine standard deviations above the average of background noise, therefore any signal above this can be confidently interpreted as light emission. While light has been detected before from a shrimp, this is the first imaging of the light emission and directly correlates the light with the cavitation singularity site.

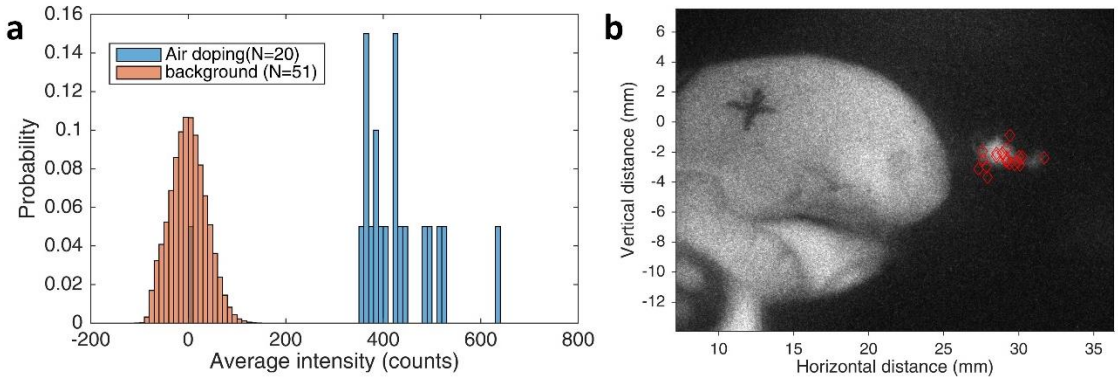

Figure 39 Light emission brightness statistics for the bioinspired device operating in saline water (*12*). (a) Probability distribution of the average intensity of pixels above threshold for different trials using saline water with air doping, bin width = 10. (b) Cavitation locations (marked red diamonds) relative to claw, as measured by ICCD.

Unlike the ICCD, the PMT can measure ns-timescale changes in light emission for a narrow region of interest. A typical ICCD image and corresponding oscilloscope traces of claw-induced light emission in saline water with air doping are presented in Figure 40. A large localized cavitation and light emission event can be spotted in the ICCD image Figure 40a, with a spatial diameter around 118.3 μm. While the cavitation oscillated, two substantial short (⩽13 ns full-width half-maximum, FWHM) light pulses were observed in the PMT signal (Figure 40b), which prove that there was light emission from the first and second cavitation singularities. PMT peak magnitudes were scaled up 5 times to make the data comparable as presented. Interestingly, there were also dim flashes near the clutch releasing process and dactyl plunger closing process, which were mainly caused by the small cavitations generated during the clutch releasing and back cavitations formed at the back of dactyl plunger as shown in the high frame rate video stills in Figure 31.

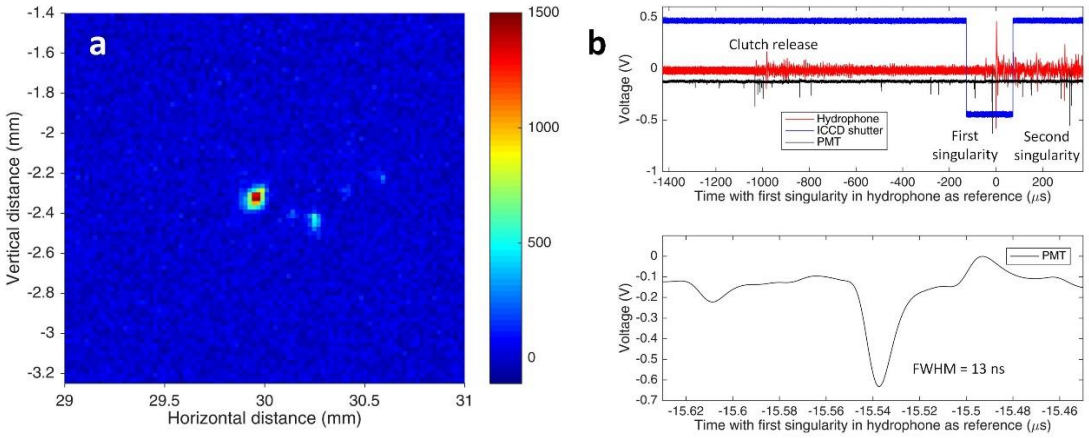

Figure 40 Light emission in ICCD images (200 μs exposure time) and corresponding hydrophone, camera shutter and PMT signal for saline water with air doping (*12*). (a) Trial #4 ICCD image and (b) trial #4 oscilloscope data and PMT signal zoom-in around first singularity.

According to data from the trial #15 as shown in Figure 41, the brightest light pulse was slightly dimmer, with light emission duration FWHM less than 14 ns. Trail #20 presented in Figure 42 has an above-average brightness, when compared to all trials. The estimated length scale of the combined light emission area in this trial approached ~600 μm, and had a slightly longer duration (less than 17 ns for FWHM), which can be attributed to the contribution of several small light emission events occurring in quick succession. Near the main light peak at the first singularity, there were dim flashes which may be due to emission of light from the tiny bubble fragments around the major cavitation site as presented in Figure 41a and are associated with the non-spherical collapse of the cavitation. This was also mentioned in the *Alpheus heterochaelis* light emission detection experiments (*7*).

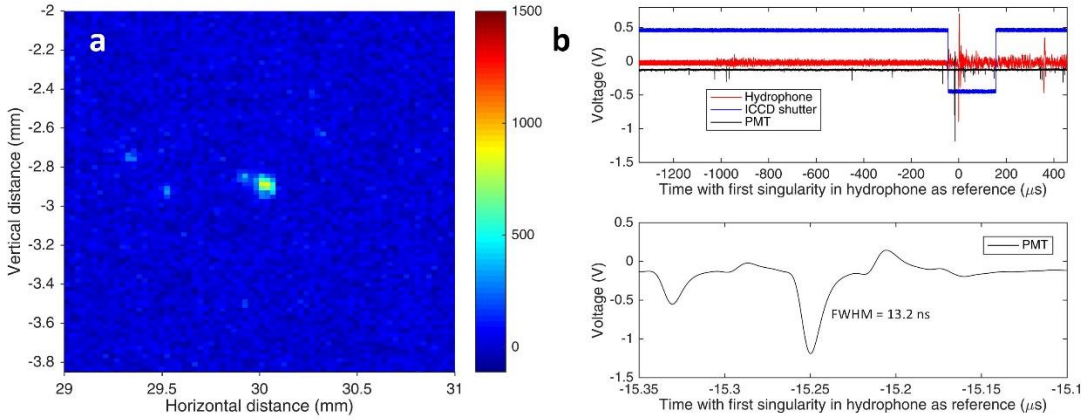

Figure 41 Light emission in ICCD images (200 μs exposure time) and corresponding hydrophone, camera shutter and PMT signal for saline water with air doping (*12*). (a) Trial #15 ICCD image and (b) trial #15 oscilloscope data and PMT signal zoom-in around first singularity.

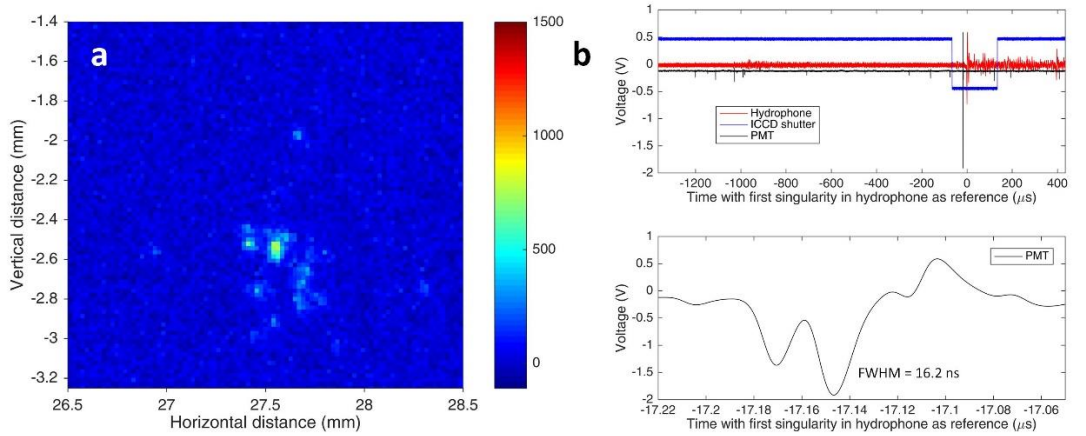

Figure 42 Light emission in ICCD images (200 μs exposure time) and corresponding hydrophone, camera shutter and PMT signal for saline water with air doping (*12*). (a) Trial #20 ICCD image and (b) trial #20 oscilloscope data and PMT signal zoom-in around first singularity.

Since PMT and ICCD camera were placed at different position during light emission experiments, there are ROI difference, lenses attenuation difference and quantum

efficiency difference for both devices. The comparison of PMT signal and ICCD image intensity is shown in Figure 43.

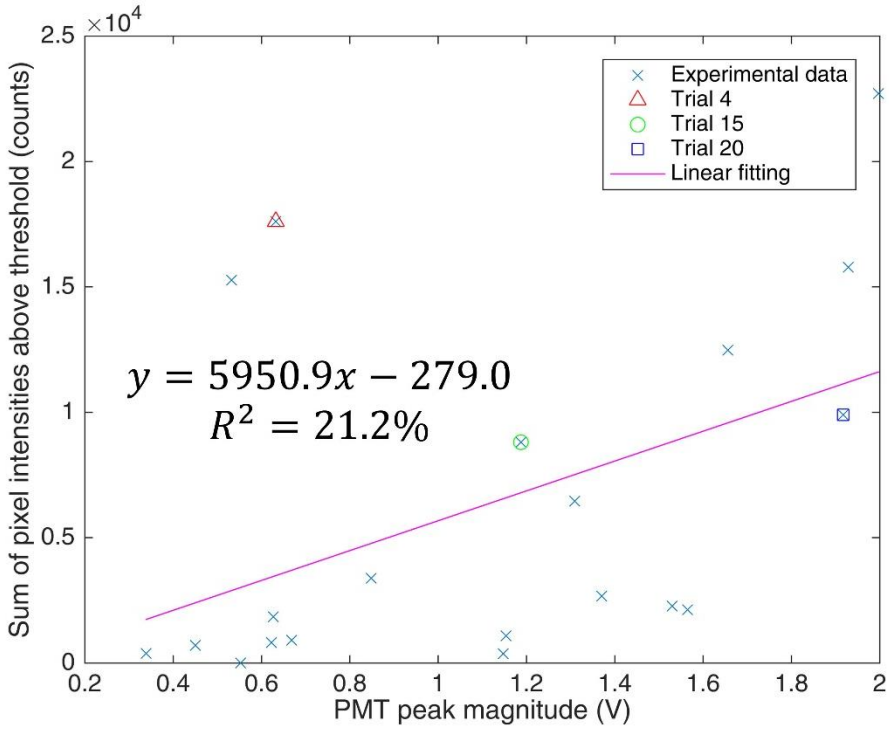

Figure 43 Relation between PMT signal peaks and ICCD image sum of pixel intensities above threshold (9σ) (*12*)

5.2.2. ICCD light emission image collection and processing

The aforementioned ICCD was also used to image the light emission from the cavitation singularity using a macro lens (AF-S VR Micro-Nikkor 105mm f/2.8G IF-ED), at 1:1 magnification ratio and f/2.8 aperture. The ICCD image exposure time was 100 μs or 200 μs with a gain setting of 1000 and artificially delayed from the clutch release time sensed by the hydrophone for around 880 μs (chosen based upon analysis of the high frame rate videos). This timing correlates to be around the first singularity and is long enough to

account for most jitter in the clutch release and short enough to avoid excessive background signal. Multiple background images were taken without triggering the bioinspired device in a dark room. These background images were averaged and subtracted from images acquired during device operation for presentation in this article. The average intensity of background images taken for background subtraction is around 60 counts (out of 4095 counts for a 12-bit system) for distilled water and 73 counts for saline water with an average standard deviation ($\sigma_{background}$) close to 34 ± 3 counts. For the images presented in this article, intensity was scaled to range from -3$\sigma_{background}$ to maximum intensity with a jet color map, in order to highlight light emission of interest in the image.

For analysis of the light emission ICCD images, a threshold was chosen for distinguishing background and pixels that captured the light emission. A threshold of 9 $\sigma_{background}$ was chosen, thus the bright pixels above threshold are statistically significant and correspond to light emission signals. Due to the stochastic influences in the cavitation formation and collapse not all singularities had the same brightness. Indeed one of the twenty trials did not have light emission exceeding the 9$\sigma_{background}$ threshold (see Figure 39a). Also, cosmic rays and similar induced excitations could randomly induce ICCD camera signal over limited pixel regions. However, such observed signals did not correlate with the expected location of the singularity nor the timing from the clutch release, as was the case for light emission during the cavitation collapse, which is shown in Figure 39b.

5.3. Distilled Water with Argon Doping

Since no light emission was observed in distilled water tank without gas doping, argon was doped into the freshly opened distilled water via a bubbling disk for 30 minutes to ensure that the solubility of argon in the water tank was saturated. It is well known that the volume ratio of argon in air is 0.93%, which is the largest among all noble gasses. Argon was chosen initially due to its accessibility, known excitation emission spectra in the visible light range, a larger polytropic exponent at bubble collapse and effective use in single bubble sonoluminescence experiments.

The argon doping test statistics are presented in Figure 44a, twenty nine hydrophone-triggered images were taken, then the location of all pixels with an intensity significantly above background were cataloged; a probability distribution histogram of average above-threshold pixel intensities is demonstrated, the average light emission pixel intensities of two trials buried in background were below the $9\sigma_{background}$ threshold. The location of these above-threshold pixels (corresponding to cavitation luminescence sites) are presented in Figure 44b, superimposed on a reference image to show the consistency of the first singularity position. The argon-doped first singularity positions had no distinctive difference from the air-doped saline water cavitation positions.

There was one trial above-threshold average intensity brighter than other trials, indicating a mode change for the light emission. The light emission image captured by ICCD can been seen in Figure 45a, which the maximum intensity detected is above 2000 counts.

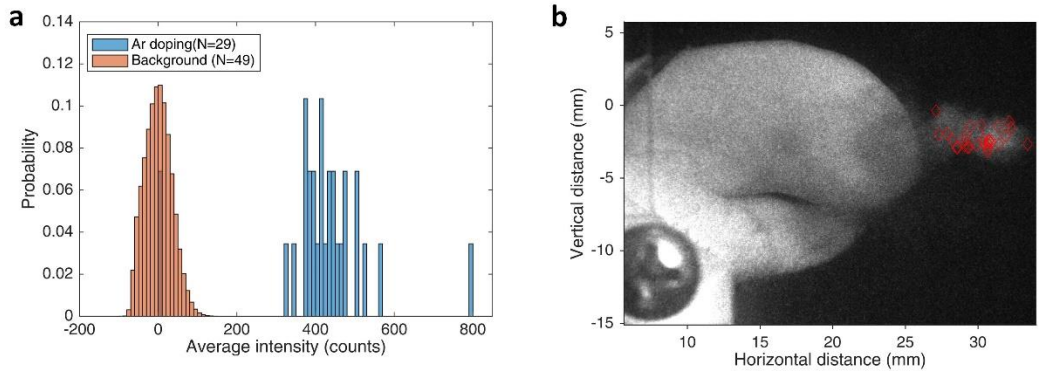

Figure 44 Light emission imaging and brightness statistics for the device operating in distilled water with argon doping at 100 µs exposure time (*12*). (a) Probability distribution of the average intensity of pixels above threshold (9σ) for different trials, bin width = 10. (b) Cavitation locations (marked by red diamond) relative to claw, regarding the pivot axis of dactyl plunger as origin.

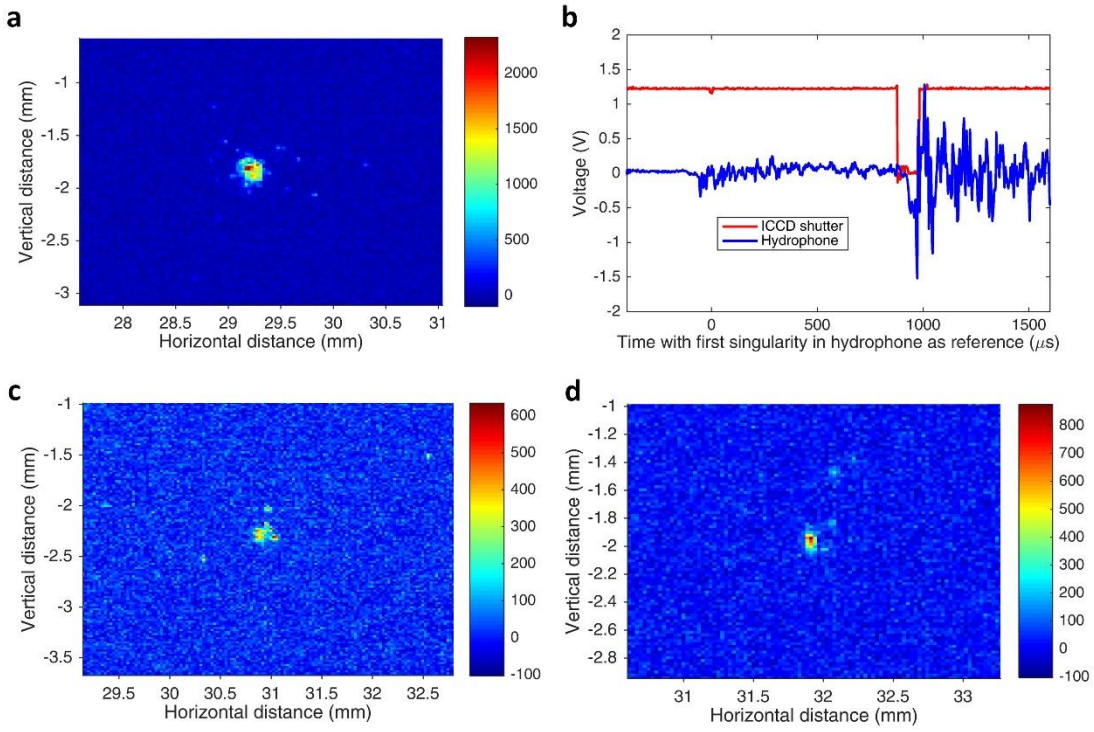

Figure 45 Light emission in ICCD images (100 µs exposure time) (*12*). (a) Trial #1 ICCD image. (b) Trial #1 oscilloscope data, the ICCD shutter signal are scaled to 1/5 for better data visualization. (c) Trial #21 ICCD image. (d) Trial #29 ICCD image.

5.4. Distilled Water with Air Doping

In order to simulate the shrimp's living condition in shallow ocean waters, air doping was applied to distilled water and saline water respectively to compare the light emission detection experiment result. Similar to argon doped case, compressed air was doped into the freshly opened distilled water via a bubbling disk for 30 minutes to ensure that the solubility of air in the water tank was saturated.

The air doped distilled water test statistics are shown in Figure 46a, eighteen hydrophone-triggered ICCD images were taken, then the locations of maximum pixel intensity were recorded; a probability distribution histogram of average above-threshold pixel intensities is demonstrated, the average light emission pixel intensities of one trial is buried in background was below the $9\sigma_{background}$ threshold. The location of these above-threshold pixels of maximum intensities (corresponding to cavitation luminescence sites) can be seen in Figure 46b, superimposed on a reference image to distilled water show the consistency of the first singularity position. The air-doped first singularity positions had no distinctive difference from the air-doped saline water and argon-doped distilled water experiments. Similarly, as presented in Figure 47a, there was one trial (trial #8) above-threshold average intensity brighter than other trials, indicating the same trend of a mode change for the cavitation luminescence. The diameter of the luminescence area captured in trial #8 is around 184 μm.

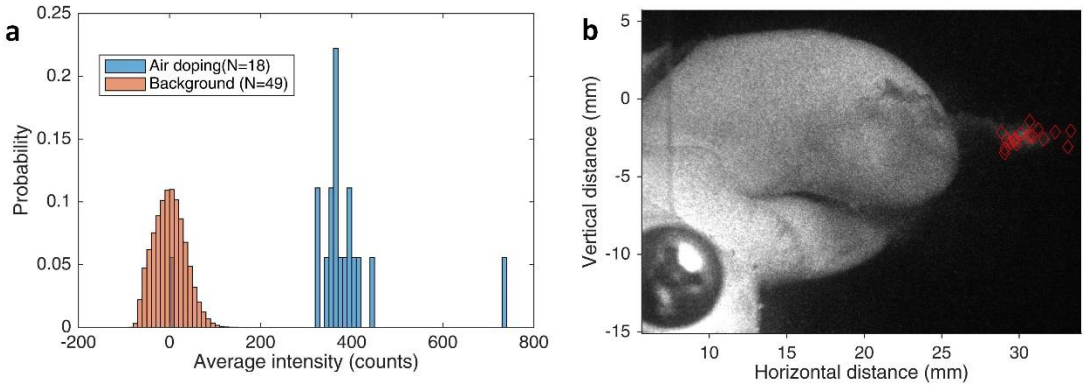

Figure 46 Light emission imaging and brightness statistics for the device operating in distilled water with air doping at 100 µs exposure time (*12*). (a) Probability distribution of the average intensity of pixels above threshold (9σ) for different trials, bin width = 10. (b) Cavitation locations (marked by red diamond) relative to claw, regarding the pivot axis of dactyl plunger as origin.

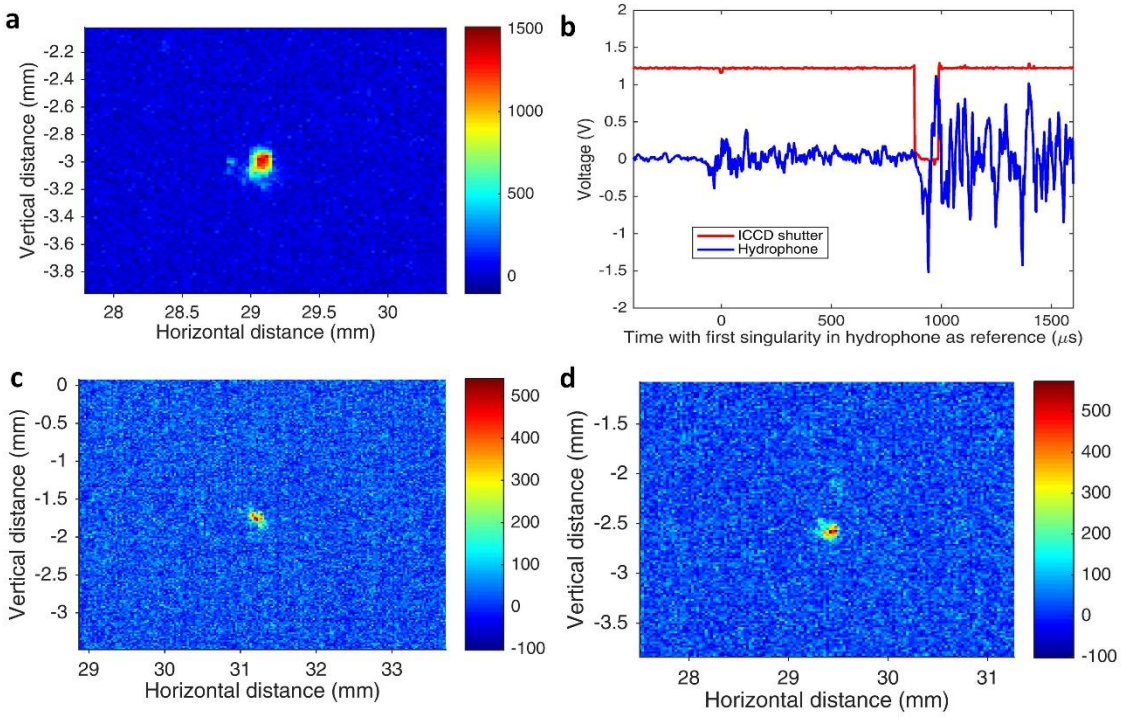

Figure 47 Light emission in ICCD images (100 µs exposure time) (*12*). (a) Trial #8 ICCD image. (b) Typical oscilloscope data, the ICCD shutter signal are scaled to 1/5 for better data visualization. (c) Trial #41 ICCD image. (d) Trial #11 ICCD image.

5.5. Summary

Based on all results from this experiment, an interesting trend emerged which suggests that a single coherent cavitation site enhance the light emission phenomenon and improve energy focusing compared to collapsing cases with tiny bubble fragments flashing at multiple cavitation sites, indicating of hydrodynamics instabilities during cavitation collapse. Similar discoveries of the multiple flashing bubble fragments in a single collapsing event were also spotted in the bigclaw snapping shrimp (*Alpheus heterochaelis*) (*7*) and laser-induced cavitation luminescence (*104*). The double weak torsion spring configuration with the releasing angle 2 setting was proved to produce cavitation luminescence successfully. Similar results and trends were also observed using distilled water with argon doping and distilled water with air doping. Light emissions in 3 cases 1) argon in distilled water, 2) air in distilled water and 3) air in saline case were observed.

6. CAVITATION CONVERSION EFFICIENCY*

> There is grandeur in this view of life, with its several powers, having been originally breathed into a few forms or into one; and that, whilst this planet has gone cycling on according to the fixed law of gravity, from so simple a beginning endless forms most beautiful and most wonderful have been, and are being, evolved.
>
> --- Charles Darwin (*165*)

6.1. The Bioinspired Mechanical Device Cavitation Conversion Efficiency

The shrimp's plasma generation technique using energy focusing may be very efficient due to evolutionary pressure (162–165). The shrimp's cavitation generation technique is more efficient than human designed devices by acoustics, electricity and light. This chapter will focus on the discussion of cavitation conversion efficiency of different cavitation generation methods: the bioinspired mechanical device, SBSL, laser-induced cavitation, and electric-induced cavitation.

Cavitation efficiency is defined as the ratio of the largest cavitation potential energy over input energy,

---

* Part of the data reported in this chapter is reprinted with permission from "Bioinspired mechanical device generates plasma in water via cavitation" by Tang, X., & Staack, D. (2019). Science advances, 5(3), eaau7765, © The Authors, some rights reserved; exclusive licensee American Association for the Advancement of Science. Distributed under a Creative Commons Attribution NonCommercial License 4.0 (CC BY-NC) http://creativecommons.org/licenses/by-nc/4.0/.

$$\eta = \frac{E_{pot1}}{E_{input}} \tag{54}$$

in which E_{pot1} presents the maximum cavitation effective radius potential energy and E_{input} represents the input energy for inducing the cavitation. We estimate the potential energy of a spherical cavitation bubble (*166*, *167*) as

$$E_{pot} = \int_0^R 4\pi r^2 \Delta p dr = \frac{4\pi}{3} R^3 \Delta p, \tag{55}$$

in which, R is the cavitation radius and Δp represents the pressure difference between the liquid pressure p_∞ and internal pressure p of the cavitation. Therefore the largest potential energy for cavitation is estimated at the maximum radius for a spherical bubble and cavitation or effective radius for certain types of ellipsoidal ones.

$$E_{pot} = \int_0^{R_{max}} 4\pi r^2 \Delta p dr = \frac{4\pi}{3} R_{max}^3 \Delta p \tag{56}$$

With this definition, the conversion efficiency for different cavitation generation techniques can be estimated and compared. The input energy for mechanical-induced cavitation in this project is the torsion springs, as defined below.

$$E_{torsion} = \frac{1}{2} k\theta^2 \tag{57}$$

in which k is the torsion spring coefficient and the deflection angle of the torsion spring is θ. With the aforementioned parameters for weak torsion spring, the bioinspired device cavitation conversion efficiency is presented in Table 4. The deflection angle of the torsion spring were from ~96.5° to 25°, and the maximum volumetric equivalent radius for the ellipsoidal cavitations were estimated from the high frame rate videos recorded during

bioinspired device operations with different type of torsion spring configurations. The cavitation conversion efficiency was up to 20%, and the double weak torsion spring configuration was empowered with better collapsing shape (closer to spherical cavitation) and decent cavitation conversion efficiency at the same time.

Table 4 Cavitation conversion efficiency for different torsion spring configuration

Spring type	k [N*m/rad]	Input Energy [mJ]	R_{max} [mm]	Bubble energy [mJ]	Conversion efficiency
Single 1	0.0770	102	3.17	13.2	13.0%
Double 1	0.1541	204	4.63	41.2	20.2%
Single 2	0.1060	140	4.05	27.5	19.6%
Double 2	0.2120	280	5.24	59.7	21.3%
Single 3	0.1541	204	4.58	39.8	19.5%

6.2. SBSL Cavitation Conversion Efficiency

The circuit driving energy for a typical cycle of single bubble sonoluminescence (SBSL) can be estimated by

$$E_{SBSL} = \frac{P}{f} = \frac{V_{p-p} I_{p-p} cos\theta}{8f} \tag{58}$$

where V_{p-p} is the peak-to-peak drive voltage on the piezoelectric transducers, I_{p-p} stands for peak-to-peak drive current, $cos\theta$ is power factor of the AC circuit in which θ is the phase difference by which the current lags the voltage. According to those parameters mentioned in Barber's dissertation (*168*), $f = 25.2\ kHz$, $I_{p-p} = 80\ mA$, $cos\theta = cos8° = 0.99$, the corresponding cavitation maximum radius $R_{max} = 45\ \mu m$, and $V_{p-p} \approx$

$700\,V$, the SBSL cavitation conversion efficiency is around 0.014%, neglecting other energy losses in the circuit.

6.3. Laser-induced Cavitation Conversion Efficiency

For the laser-induced cavitation, the input energy (E_{pulse}) is usually the laser pulse energy, which varies depending on the laser utilized for the experiment. From literature (*104*, *146*, *147*, *169–172*), the maximum laser-induced cavitation conversion efficiency ($\eta_{laser} = \frac{E_{pot1}}{E_{pulse}}$) is less than 19.3%. Considering the wall-plug efficiency around 30% for laser systems with extra cooling, the laser-induced cavitation conversion efficiency is less than 5.8%. The wall-plug efficiency of different type of lasers are listed in NRL Plasma Formulary (*173*). A summary of the cavitation conversion efficiency for laser-induced cavitation is listed in Table 5.

Table 5 Cavitation conversion efficiency for laser-induced cavitation without wall-plug efficiency

	Laser type	Pulse duration (ns)	Energy per pulse (mJ)	R_{max} (mm)	Cavitation potential energy (mJ)	Fluid	Efficiency
Lauterborn(1975) (*169*)	Q-switch ruby	30-50	100-1000	2	3.32	Water	0.33%-3.3%
Lauterborn(1997) (*170*)	Nd:YAG	8	10	1.5	1.40	Silicone oil	14.0%
	Q-switch ruby	30-50	100-1000	2	3.32	Water	0.33-3.3%
Baghdassarian(1999) (*104*)	Nd:YAG	6	600	1.1	0.55	Water	0.09%
Akhatov(2001) (*171*)	Nd:YAG (1064 nm)	8	400	0.5	0.052	Water	0.01%
			400	3	11.2		2.8%
Brujan(2001) (*172*)	Nd:YAG (1064 nm)	6	8	1.55	1.54	Water	19.3%
Tinguely(2012) (*167*)	Nd:YAG (532nm)	8	55		2.2	Water	4%
			230		10.2		4.4%
Lazic(2013) (*146*, *147*)	Nd:YAG (1064 nm)	6.5	140	3.6	19.35	Water	13.8%

6.4. Electric-induced Cavitation Conversion Efficiency

Electric pulse technology has been utilized in a variety of industrial applications like drilling, recycling, and demolition for decades. The methods of electric pulsed technologies are electrohydraulic (*18*) in liquids, electrodynamic or internal electric breakdown inside solid dielectrics (*19*), plasma blasting or the use of dielectric material surface flashover (*20*), and electric explosion of wires on the surface of a dielectric (*21*). The cavitation conversion efficiency of electric-induced cavitation in this section focuses on the electrohydraulic in liquids.

6.4.1. Spark discharge with two electrodes setup

A pulsed power circuit experimental setup diagram is presented in Figure 48, a high voltage DC power supply (Spellman SL300) was connected with a 40 MΩ ballast resistor to an adjustable length spark gap switch in parallel with a 1 nF capacitor. The ballast resistor protected the power supply from voltage reversal. The adjustable length spark gap controlled the breakdown voltage across the capacitor. A two electrodes spark gap was placed inside a water tank to induce cavitation.

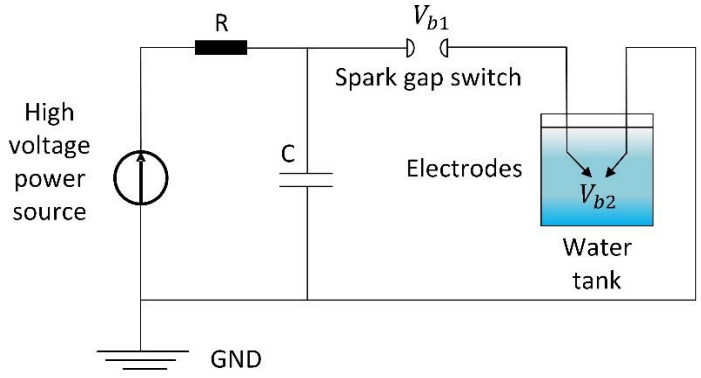

Figure 48 Schematic diagram of the pulsed power circuit for spark discharge

For the diagnostic of the circuit, a current monitor (Pearson, model 5046) was used to measure the current sustaining the pulsed underwater discharge, it was placed before the underwater spark electrodes and after the spark gap switch in the circuit, as demonstrated in Figure 49a. A high voltage probe (North Star PVM-4) was placed near the same position to get voltage data simultaneously for the pulsed spark discharge. Both signals were acquired by the oscilloscope which was triggered by the current pulse. With the help of circuit diagnostics, the electric energy for a single pulse of underwater spark discharge can be estimated accurately with the correction of probe delay between current and voltage probes. The electrodes were made of 1 mm diameter stainless steel covered by circular silicone rubber insulation which can rated up to 40 kV high voltage. A schematic diagram of spark discharge schlieren imaging setup and the photo of the setup can be seen in Figure 49a and b respectively.

The total energy input for this pulsed power circuit can be estimated by the energy stored in the resistor-capacitor (RC) circuit, using the following equation

$$E_{capacitor} = \frac{1}{2} C V_b^2 \tag{59}$$

where C is the capacitance (1 nF) and V_b is the breakdown voltage of the air spark gap switch. The spark gap distance was carefully tuned so that the breakdown voltage was set at -20.2 kV. Thus the total input energy was ~204 mJ which is equal to the shrimp-inspired device with double weak torsion spring configuration.

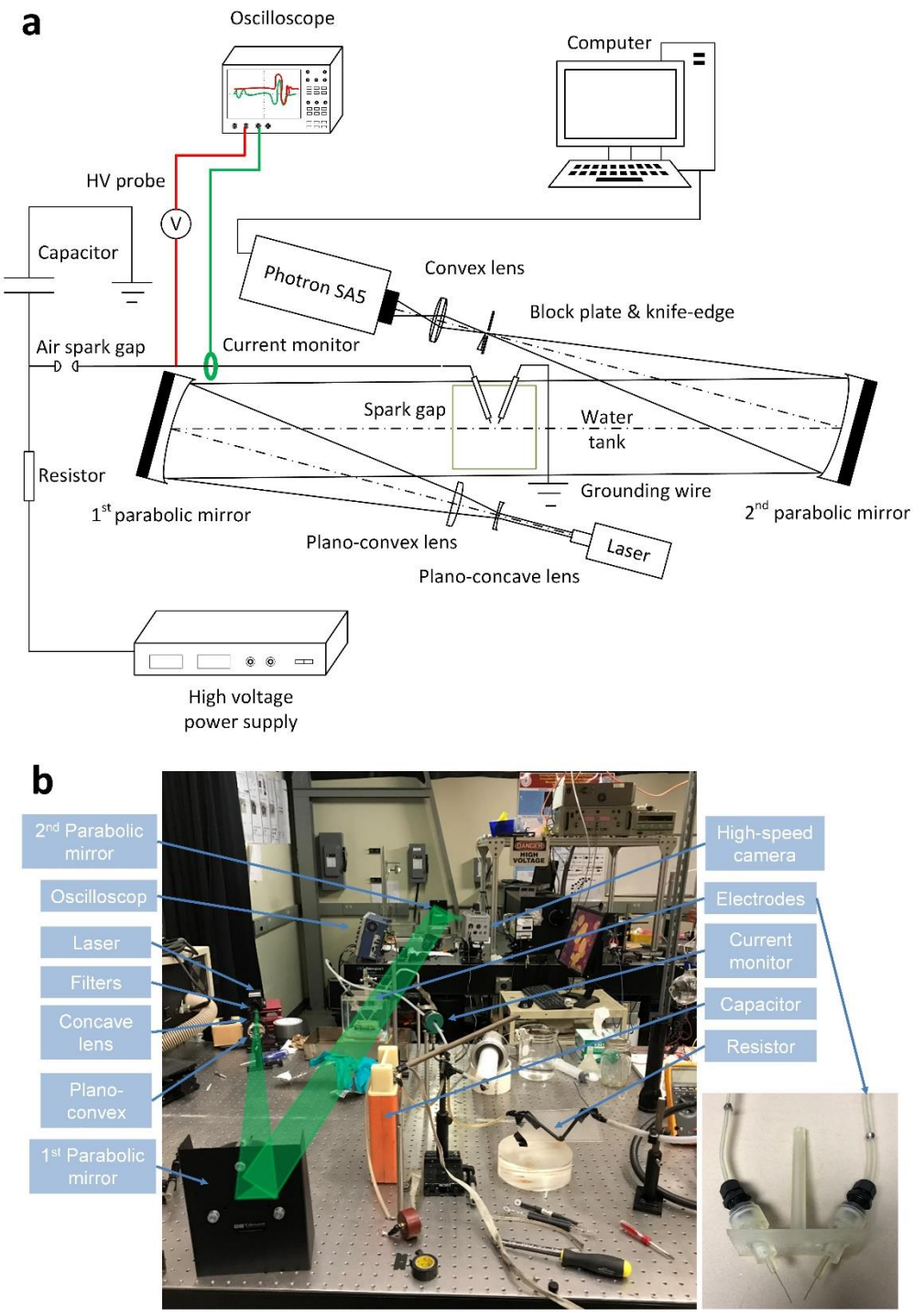

Figure 49 Pulsed electric discharge setup . (a) Schematic diagram of spark discharge schlieren imaging setup. (b) Experimental setup photo.

The oscilloscope traces of voltage probe and current monitor are displayed in Figure 50a, the rise time of the voltage was approximately 100 ns, and the overall discharge time was around 440 ns. When the breakdown happened in the air spark gap switch, the voltage after the spark gap switch was suddenly jumped to -16.25 kV from 0 kV, and was then dropped down to -0.79 kV after depositing energy into the spark discharge in water. The energy per pulse of the water spark discharge can be calculated by numerical integration of voltage and current with probe delay adjustment. The spark discharge energy can be estimated by

$$E_{Spark} = \int_0^{t_o} V(t)I(t)dt \tag{60}$$

, in which $V(t)$ and $I(t)$ are voltage trace and current trace acquired by the oscilloscope during the discharge time t_o. After the discharge time, the energy per pulse remained at a constant value. As shown in Figure 50b, the energy per pulse for spark discharge in water was 56.47 mJ, indicating 27.7% of total input energy was deposited into the underwater spark discharge, and 72.3% of total input energy was dissipated in the air spark switch.

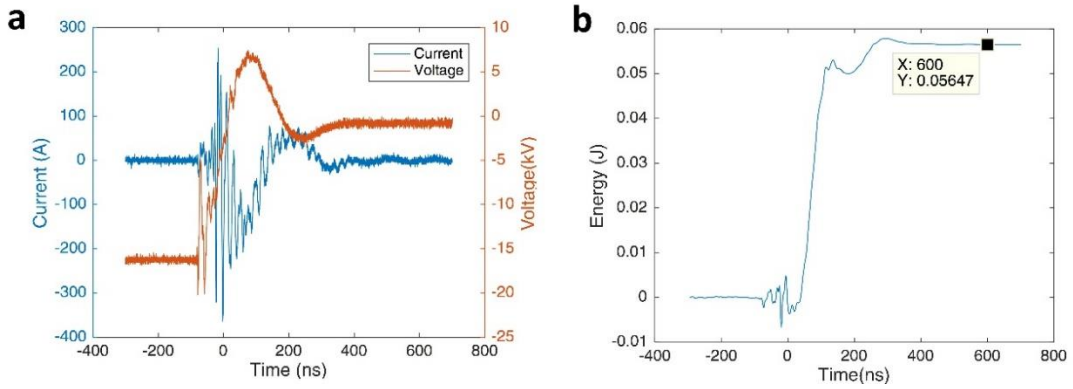

Figure 50 Spark discharge energy per pulse. (a) Scope traces of voltage and current. (b) Energy per pulse evaluated by cumulative trapezoidal numerical integration.

To estimate the energy per pulse measurement accurately, the probe delay between the high voltage probe and current transformer need to be considered. Each of these probes has its own characteristic propagation delay. The difference in these two delays, known as skew, causes inaccurate timing measurements and distorted power waveforms. The high voltage probe utilized a 15 ft BNC cable with 50 Ω termination value. The current probe employed different length of 50 Ω BNC cable according to different setup configuration and reduction of electromagnetic interference (EMI) on diagnostic systems. The probe delay measurement for different length of current probe cables are demonstrated in box plots presented in Figure 51. If the probe delay value was positive, it means the current signal was leading, vice versa. The 'averaged' stands for traces recorded with 100 events averaged, and the 'pos' or 'neg' in the figure indicated the direction of the current transformer was the same of the electron direction or the opposite. The probe delay values measured from the start of the current and voltage traces and those values measured at the half maximum of the current and voltage rise ramp were close for the 50 ft current cable, thus 5 ns probe delay was chosen.

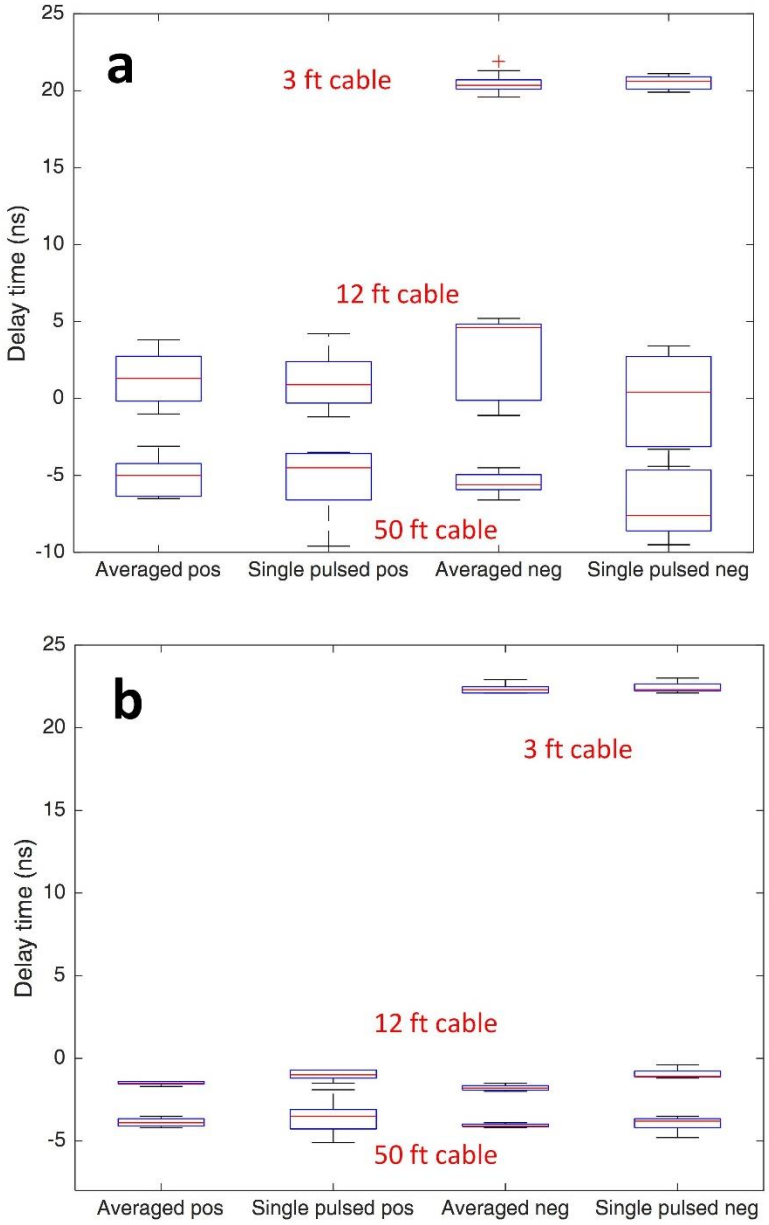

Figure 51 Probe delay between the voltage probe and current probe. (a) Probe delay measured at the beginning of pulse event. (b) Probe delay measured at the half maximum during the signal ramp.

The electric-induced cavitation bubble dynamics and corresponding stills from high frame rate video with underwater spark discharge are illustrated in Figure 52 and

Figure 53 respectively. For the energy partition and efficiency analysis, the maximum radius of the cavitation bubble recorded in Figure 52 before the first singularity was ~2.78 mm, and the cavitation bubble mechanical energy at the maximum volume was 8.91 mJ. Therefore the cavitation conversion efficiency for the spark discharge in water was around 4.4%. The air spark switch dissipated ~60% total input energy, Between the first and second singularities, the maximum radius of the second oscillating cycle was ~1.71 mm, which obtained the cavitation mechanical energy of 1.13 mJ, indicating 7/8 of the total cavitation potential energy went into non-adiabatic processes: heat and mass transfer, fluid flow, shock waves, and light emission.

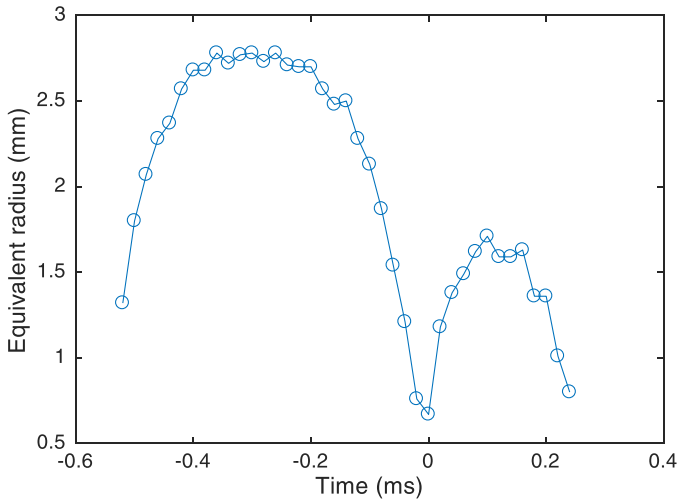

Figure 52 Bubble dynamics of the spark-induced cavitation bubble

From the selected video frames, as shown in Figure 53, the electrolysis process with 'bush-shaped' bubble initiated first from the cathode and reached anode electrode before the spark discharge was fully developed. When the braches of the bush-like bubble reached the anode through the 2.5 mm gap distance, a spark discharge streamer bridged

through the gas phase and formed a plasma channel to deposit the electric energy into the form of resistive heating, shock wave and photon emissions. Both the shock waves and light emission can be spotted on the -0.52 ms frame. The first singularity was close to 0.00 ms where the collapsing cavitation just transferred to exploding shock waves. The whole life time of the electric-induced cavitation bubble before first singularity was approximately 520 μs, and the subsequent second cycle was around 280 μs.

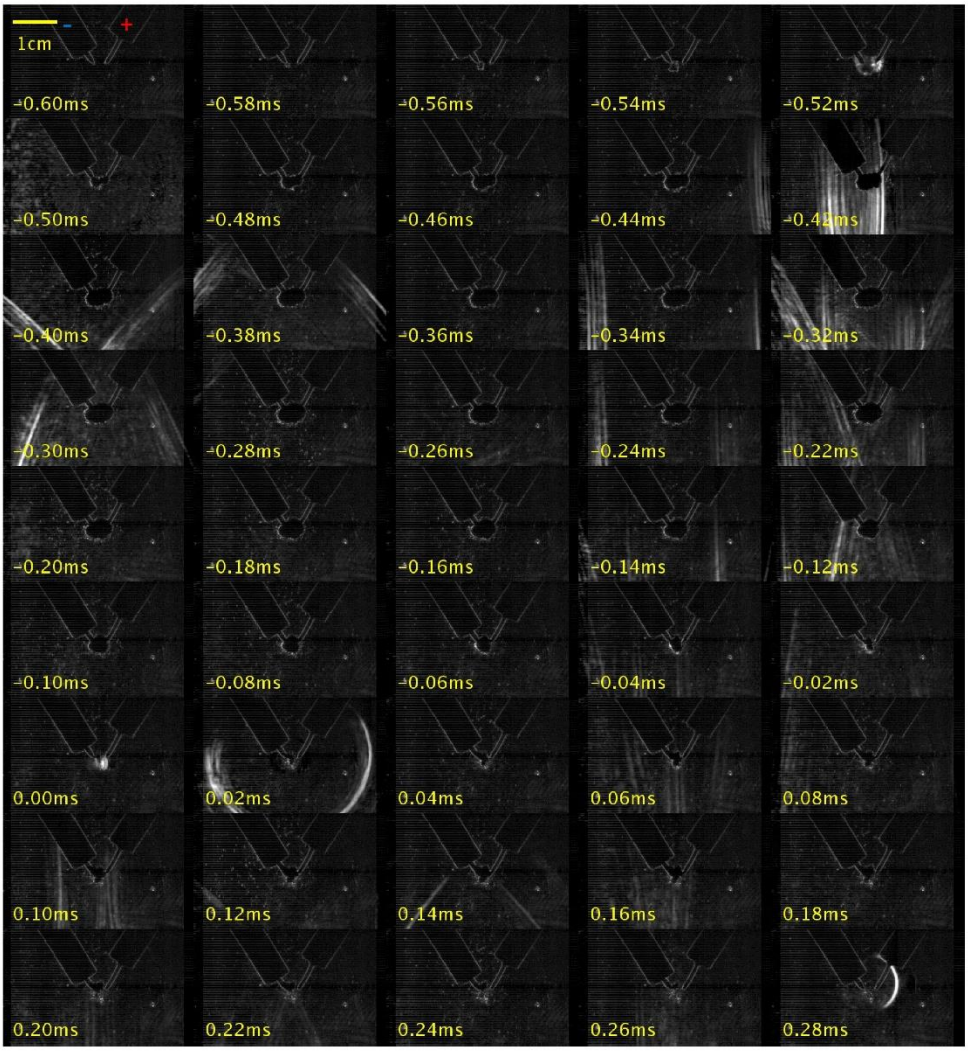

Figure 53 Selected video frames during spark discharge, emphasizing cavitation evolution. Recorded at 100,000 fps with t=0.00 ms corresponding to the first singularity.

6.4.2. Corona discharge with single electrodes

For the corona discharge configuration, a single electrode was set up with a grounding strap touching the water body in the tank, as shown in Figure 54. Since the shape of the bubble generated is non-spherical, only the maximum volume cavitation frames of negative and positive polarities are displayed in Figure 55 a and b respectively.

For the negative polarity, the bubble was bush-like shape with a maximum radius approximately 0.7 mm with cavitation potential energy ~1.4 mJ. The cavitation conversion efficiency was 0.7%. As for the positive polarity corona discharge, the bubble was branch-like shape at sub-millimeter level radius. Spherical expanding shock waves were spotted at the end of the branch-like filaments. Though the accurate radius for the filament was unable to be identified in the high frame rate video stills, the cavitation conversion efficiency in this case was definitely smaller than the negative polarity case.

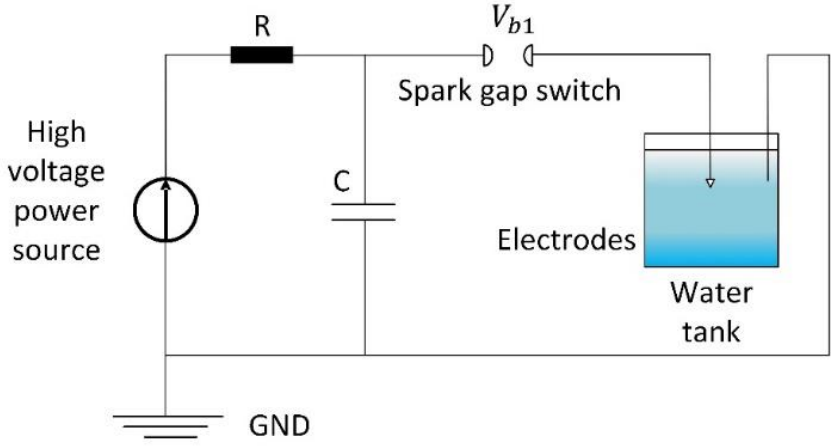

Figure 54 Schematic diagram of the pulsed power circuit for corona discharge

For spherical bubble generation, Xiao's paper (*143*) provided an estimation for input energy of micro-plasma generated cavitation bubble with single-spark-gap (103.1

mJ) and double-spark-gap (0.552 mJ) respectively. Comparing to the maximum radius of the cavitation generated with single-spark-gap ($R_{max} = 130$ μm) and double-spark-gap ($R_{max} = 88$ μm), the corresponding cavitation conversion efficiencies were around 0.009% and 0.058%, respectively.

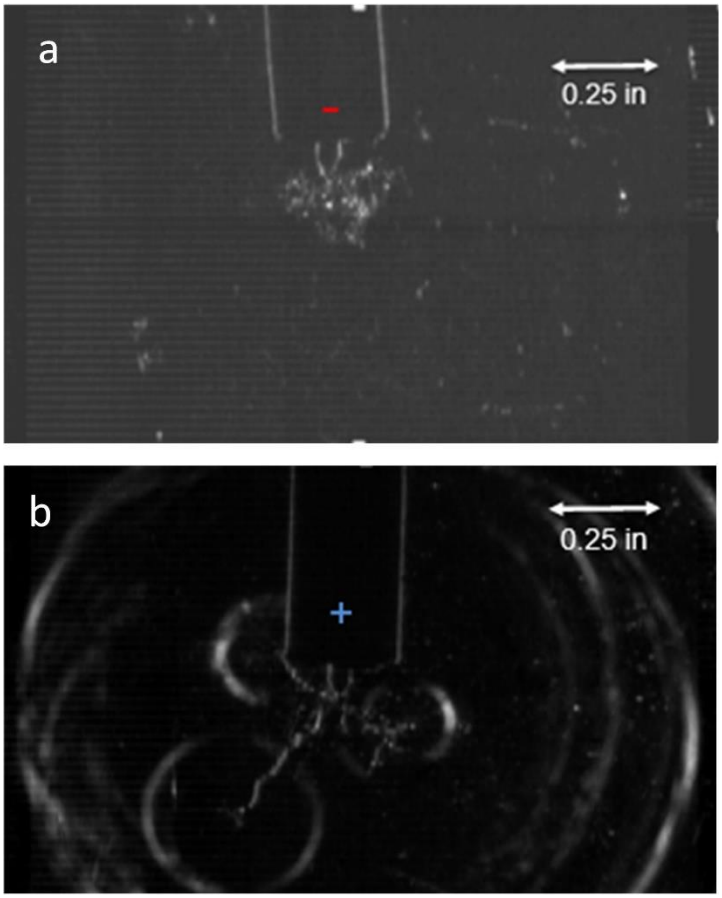

Figure 55 Schlieren image of the corona discharge induced cavitation at maximum volume. (a) Negative polarity (cathode) discharge at 20 kV. (b) Positive polarity (anode) discharge at 24.8 kV.

6.5. Summary

This chapter discussed the cavitation conversion efficiency employing three different methods of cavitation generation: by hydrodynamics with shrimp-inspired

mechanical device, by sound, and by light. Since these plasmas were generated in the manner of collapsing cavitation, unlike the conventional plasma induced by electricity, the translational energies of gas molecules and atoms inside the cavitation increase first with thermodynamic polytropic compression, followed by the increase of vibrational energies, rotational energies in nanosecond time scale with photon emissions. Therefore, the overall plasma generation efficiency, which is unable to be estimated with the experimental data so far, is directly related with the cavitation conversion efficiency for these type of plasmas.

The cavitation conversion efficiency of the bioinspired mechanical device was up to approximately 20% with volumetric equivalent radius estimation. It is so far better than SBSL, electric-induced cavitation and laser-induced cavitation. This also indicated that the mechanical device is more efficient in generating underwater shock waves, which proves that those snapping shrimps have developed an efficient mechanism due to evolution pressure.

7. PLASMA TEMPERATURE INSIDE THE COLLAPSING CAVITATION

What is the states inside the luminescing cavitation? Based on the similarity between SBSL to “shrimpoluminescence”, it could be highly probable a LTE plasma with a broadband light emission. However, the cavitation luminescence light emission of the shrimp-inspired device and the snapping shrimp are both too dim to be detected with un-aided eyes as well as spectrometers.

The mechanism of a typical small spectrometer is illustrated in Figure 56. Light signal at the detectable level of the spectrometer is collected through lens or optical fibers and then it is collimated by a collimating mirror. The reflected light beam is then directed to a diffraction grating or other type of gratings to split the photons at different wavelength and guide them into a pre-calibrated detector. The detector converted the photons into electric signals and plot the spectrum with some software.

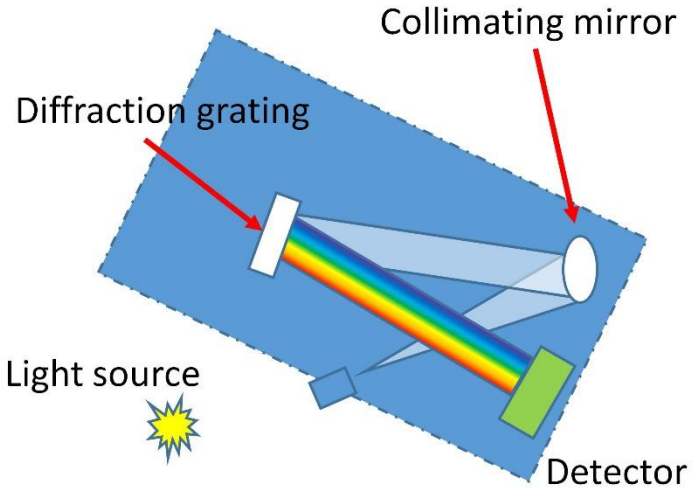

Figure 56 Typical optical spectrometer

The same idea of the spectrometer mechanism is used here to establish a similar system as a spectrograph in water hammer cavitation luminescence case (*82*). The difference is a precisely triggered ICCD is employed instead of a spectrograph with high-gain image intensifier. With well-timed trigger, shutter and high-gain intensifier in ICCD, a spectrum of each event of cavitation luminescence will be recorded on the ICCD for post processing.

7.1. Experimental Setup for Spectrum Measurement

The experimental setup for spectrum measurement is demonstrated in Figure 57. Similar to previous light emission detection system in dark room, the bioinspired device was immersed within a glass water tank with hydrophone monitoring the sound pressure in water to trigger the ICCD before the cavitation luminescence event, as illustrated in Figure 57a. The light emission was collected by a plano-convex achromatic lens (VIS-NIR Coated, 75 mm diameter, 100 mm focal length), and focused to the ICCD intensifier, passing through a UV transmission grating (Edmund optics 85291, 300 groove per mm, 8.6 ° blaze angle, 25 mm*25 mm*2 mm) for light diffraction, seen in Figure 57b. The lens and grating were carefully positioned to record the 0 mode and +1 mode simultaneously. With amenable preset delay time and exposure time during the snap operation, the ICCD then recorded the spectrum.

For calibration purpose, an optical fiber with one end pointed at a mercury lamp and the other end right near the light emission spot of the collapsing cavitation on a 3D printed optical fiber holder as shown in Figure 58a. The 3D printed optical fiber was

designed with a male SMA connector (as displayed in Figure 58b) compatible with the SMA optical fiber (as presented in Figure 58c) used for calibration. Since the collapsing event happened within a range of 3 mm based on previous light emission data, therefore calibration was also conducted at different horizontal positions to devoid the collapsing event position jitter caused by turbulence and hydrodynamic instabilities.

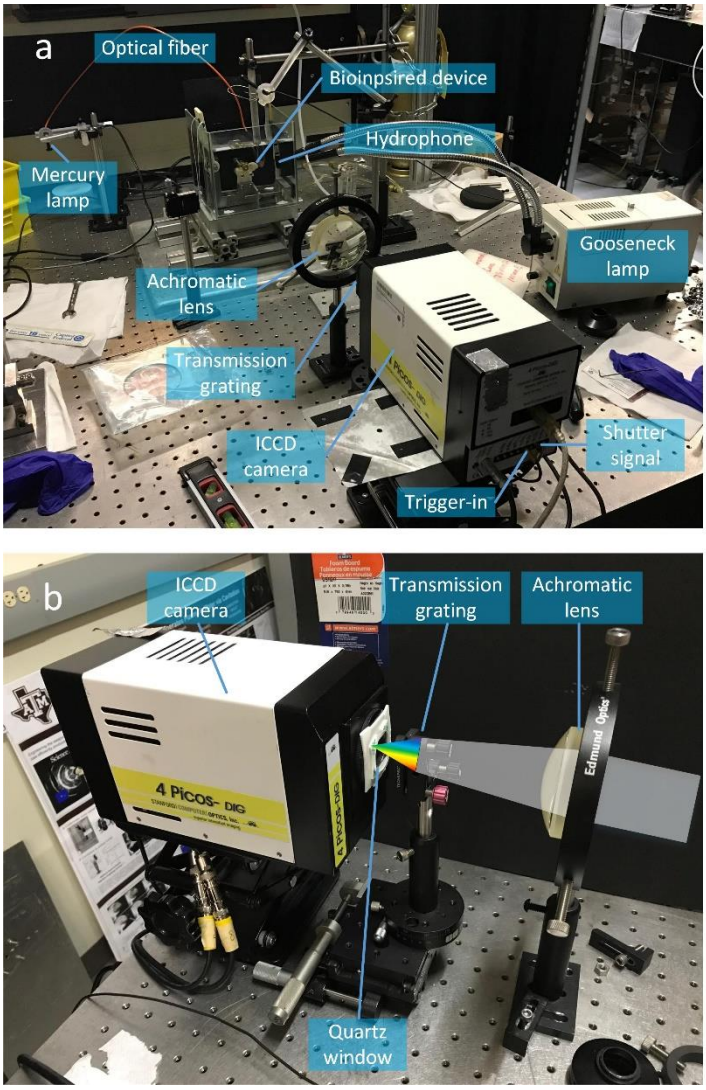

Figure 57 Experimental setup for cavitation luminescence spectrum measurement
(a) Spectrum recording system in dark room. (b) Transmission grating position.

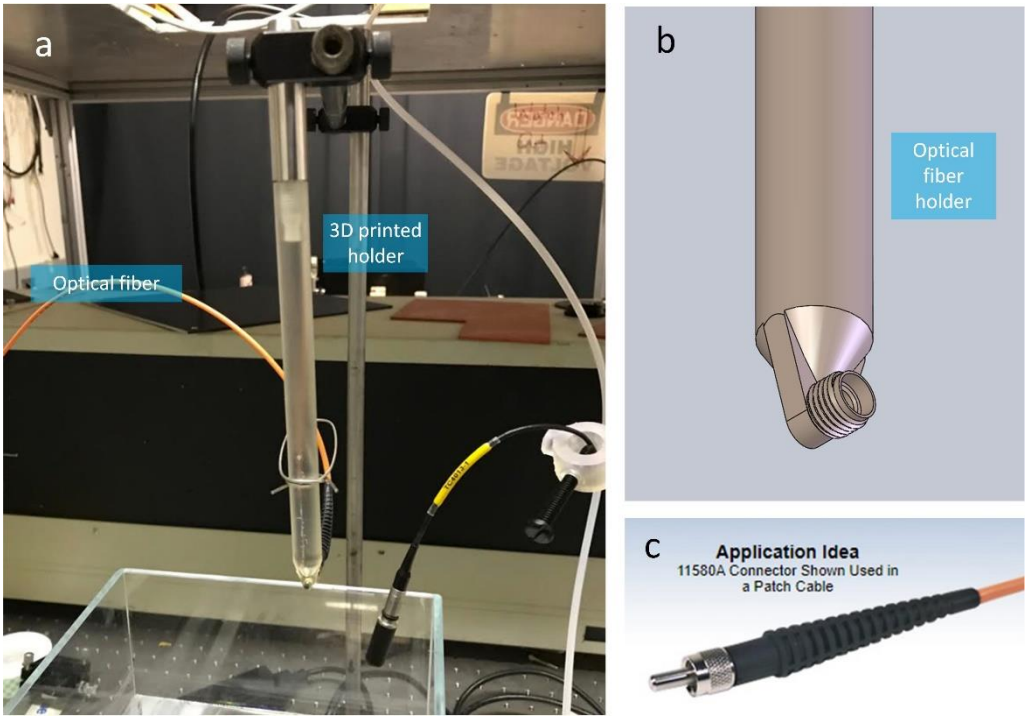

Figure 58 Mercury lamp calibration system with optical fiber holder near cavitation site. (a) Optical fiber holder assembly. (b) CAD model of the optical fiber holder. (c) SMA connector of the optical fiber.

Before starting experiment, hydrophone signal triggered ICCD were tested first by carrying out repetitive snaps with hydrophone signal and ICCD shutter signal monitored by the oscilloscope (WaveRunner 204MXi 2 GHz, 10 GS/s, produced by Teledyne LeCroy company). Then the video mode of ICCD was turned on to ensure the closed snapper claw tip was placed properly so that the light emission spot (0 order) and smeared out optical fiber tip (+1 mode) due to diffraction were included in the ROI. Calibration using mercury light was conducted at different positions afterwards for post processing. Gas doping is used to promote the light emission intensity. Compressed air or argon was

doped into the distilled water or saline water with the same bubbling stone for 30 min to ensure the saturation of the doping gas.

The mercury light emission lines detected by a portable spectrometer with water tank glass and no glass are compared Figure 59. These data demonstrated that the tank glass blocked most UV lines except the 365.0158 nm line which later absorbed by other optical devices. The 576.961 nm line and 579.067 nm line are too close to be resolved by the instrumentation and light dot size from the optical fiber.

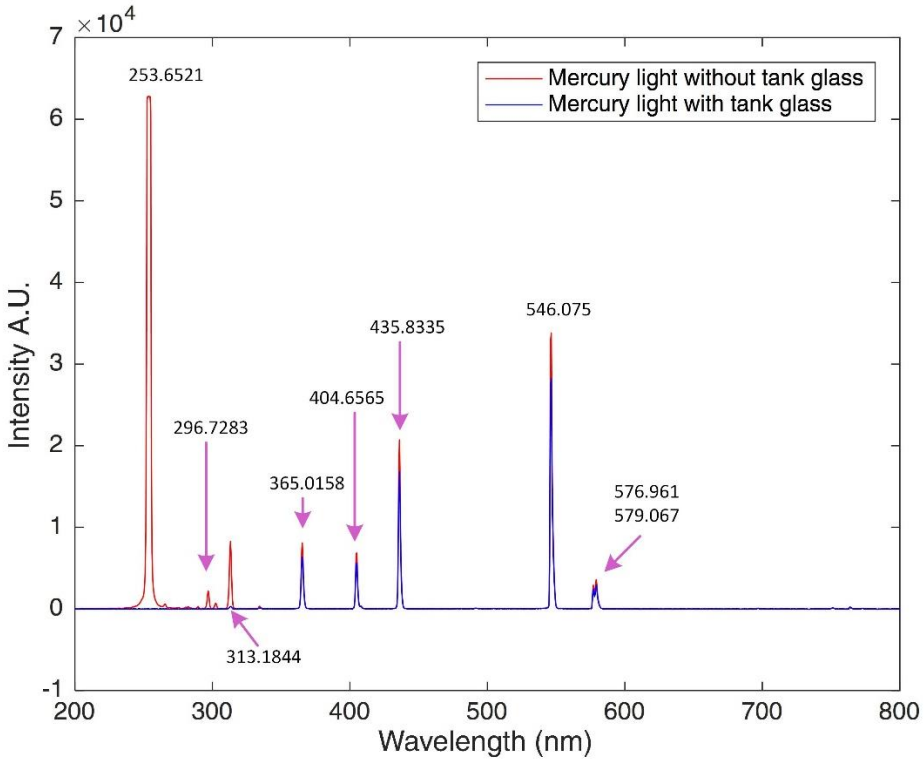

Figure 59 Mercury light emission lines with tank glass vs. no glass

For the calibration in different positions as illustrated in Figure 60a, only four mercury emission lines were observed in +1 order on ICCD calibration images: 404.6565

nm, 435.8335 nm, 546.075 nm, and 576.961 nm lines. The corresponding peak positions together with the zero order are shown in Figure 60b.

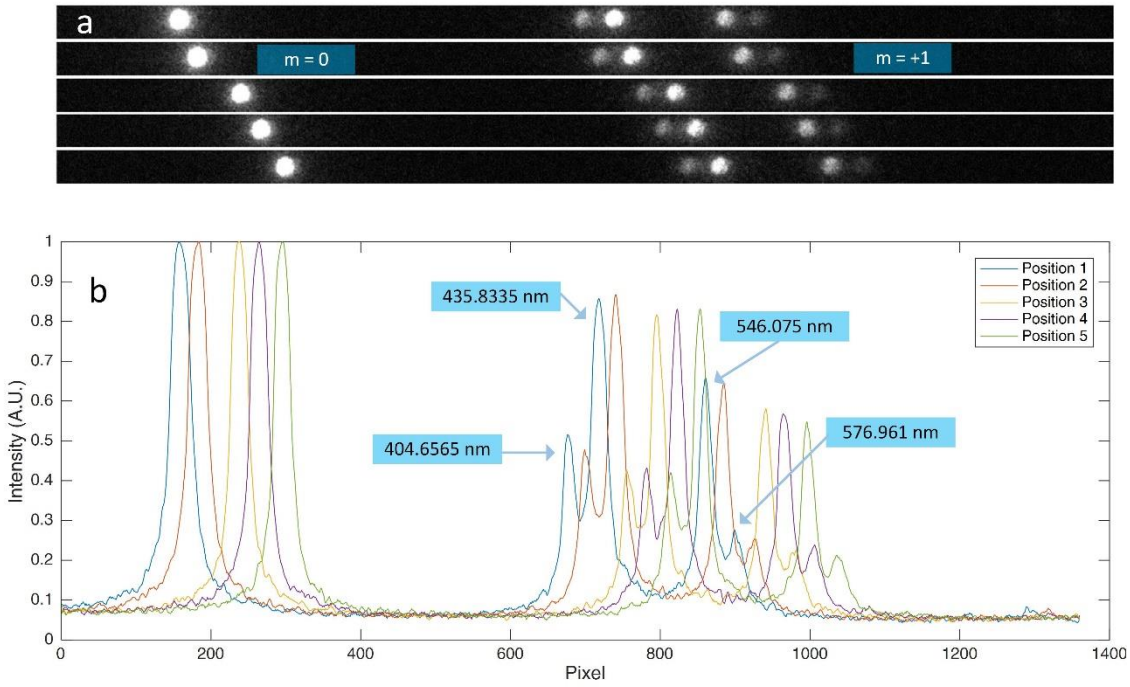

Figure 60 Mercury lamp calibration at different positions.
(a) ICCD calibration images with mercury lamp. (b) The mercury emission lines at different positions.

The peak intensity pixel position relationship are plotted in Figure 61 and fitted with linear regression for latter calibration purpose with cavitation luminescence spectrum. The linear trend line indicated that the position change of the zero order will not affect the pixel distance between each first positive order emission lines. Therefore the conversion ratio of pixel distance over wavelength distance can be treated as a constant for the optical system.

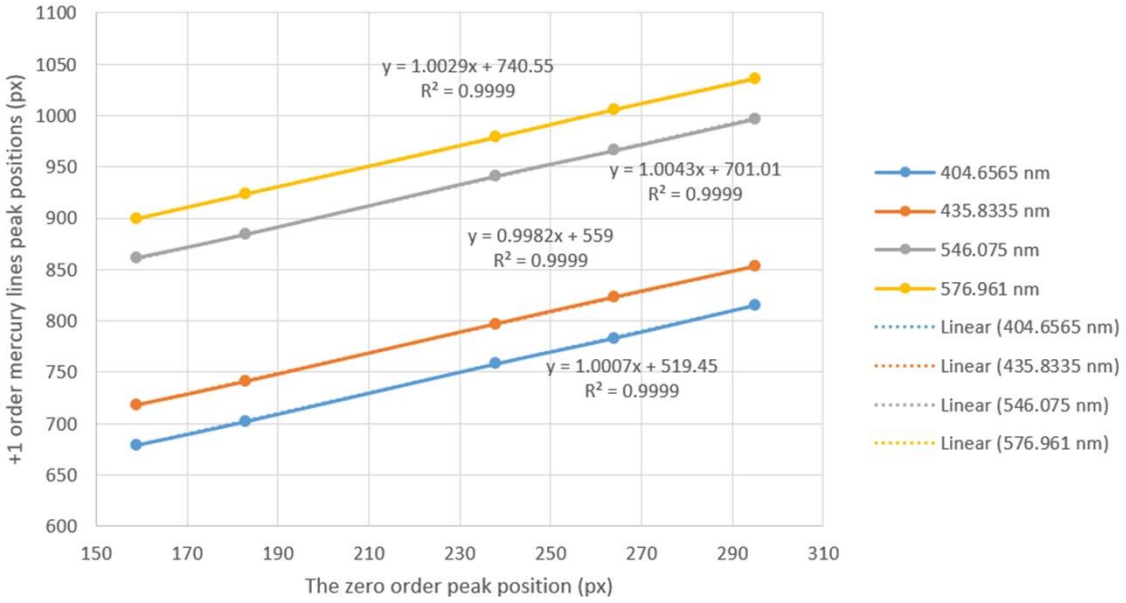

Figure 61 Mercury lamp the zero order peak position vs. first positive order emission lines peak positions

7.2. Efficiencies of the Optical System

Even though spectrum can be acquired with the experimental setup, is the real spectrum shape still maintain from the cavitation luminescence to the recorded ICCD images? Every optical component has its own effective efficiency, for example, the achromatic lens coatings will only allow photons within a narrow range passing through with different transmission coefficient depending on the photon wavelength. This section the overall efficiency of the optical system will be discussed and estimated.

Water: the distilled water or saline water can absorb all the light with wavelength below 200 nm, which is also called the UV cutoff of water.

Water tank glass: the glass wall is 1/8 inch thickness unknown glass which absorbs all UV lines from 200 nm ~350 nm, and with certain transmission for the visible spectrum.

The transmission coefficient is calculated based on spectrometer experimental data with UV, F/A standard light source from color assessment cabinet.

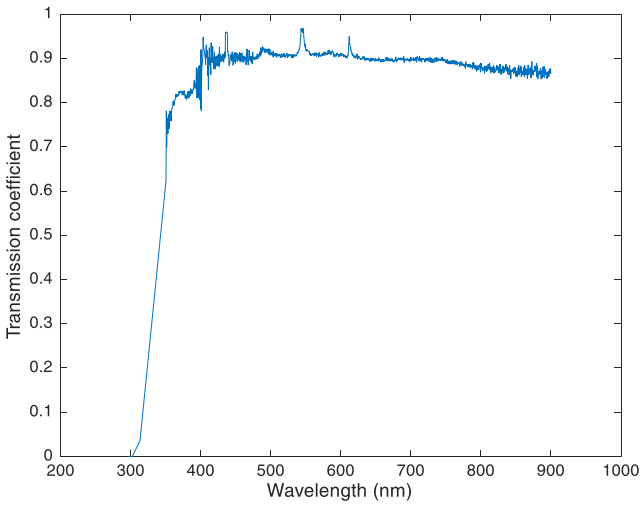

Figure 62 Water tank glass transmission coefficient based on standard light source

UV transmission grating: the transmission efficiency data for the zero order and first positive order were provided by the Edmund Optics customer service for #85291 (300/8.6 degree UV Tx grating), see Appendix.

Achromatic lens: only anti-reflection coating curve is provided by the vendor, Edmund optics, and they mentioned that the absorption of the lens material is negligible. For the detailed VIS-NIR coating reflectance data, please see the Appendix.

Quantum efficiency of the ICCD: this ICCD intensifier photoelectric quantum efficiency is a curve based on a non-orthogonal coordinate system, as shown in Figure 63, only several points can be extracted accurately based the information provided in the manual of the camera. The ICCD intensifier used in spectrum recording is curve B = S20 UV (Q).

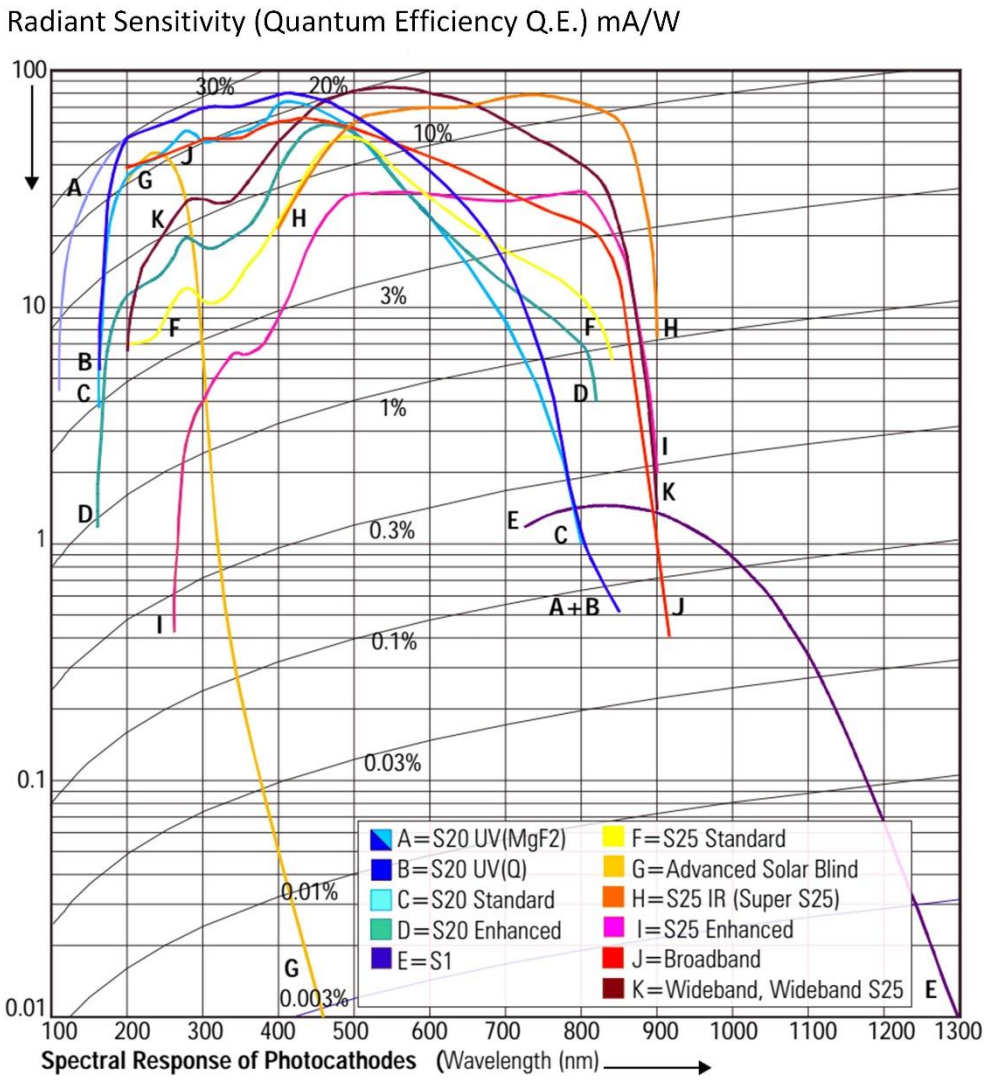

Figure 63 Different intensifiers quantum efficiency from camera vendor, curve B is the intensifier utilized in the ICCD

Due to the quantum efficiency data from the ICCD is limited and hard to extract from the curve that the vendor provided, thus a standard light source D65 is employed for overall efficiency estimation of the optical system. The spectrum of the D65 light source spectrum and the corresponding blackbody radiation curve are demonstrated in Figure 64. Since D65 represents white light, the name suggests that the correlated color temperature

(CCT) should be 6500 K, while in fact it is closer to 6504 K. This discrepancy is due to the scientific community's revision of the constants in Planck's law after the definition of the illuminant.

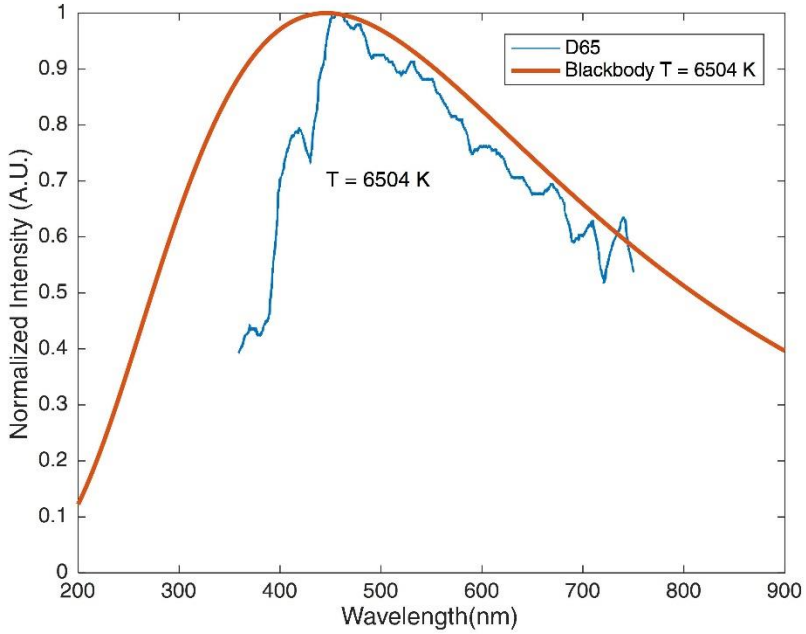

Figure 64 Standard D65 light source and corresponding blackbody radiation curve

With the standard D65 light source, the overall optical system efficiency can be estimated to reveal the actual shape of cavitation luminescence spectrum including every optical components in the spectrum recording setup. The overall efficiency is estimated by estimating the ratio of recorded spectrum over the standard light source data at varying wavelength by scaling at one known efficiency point, as demonstrated in Figure 65. The chosen point is the 456 nm with ICCD quantum efficiency ~20%, and coupled with other optical components, the overall efficiency is ~ 8.36% for the 456 nm data. After scaling

the 456 nm of the recorded data to the 8.36% of the normalized intensity of D65 data, the overall efficiency can be estimated accordingly.

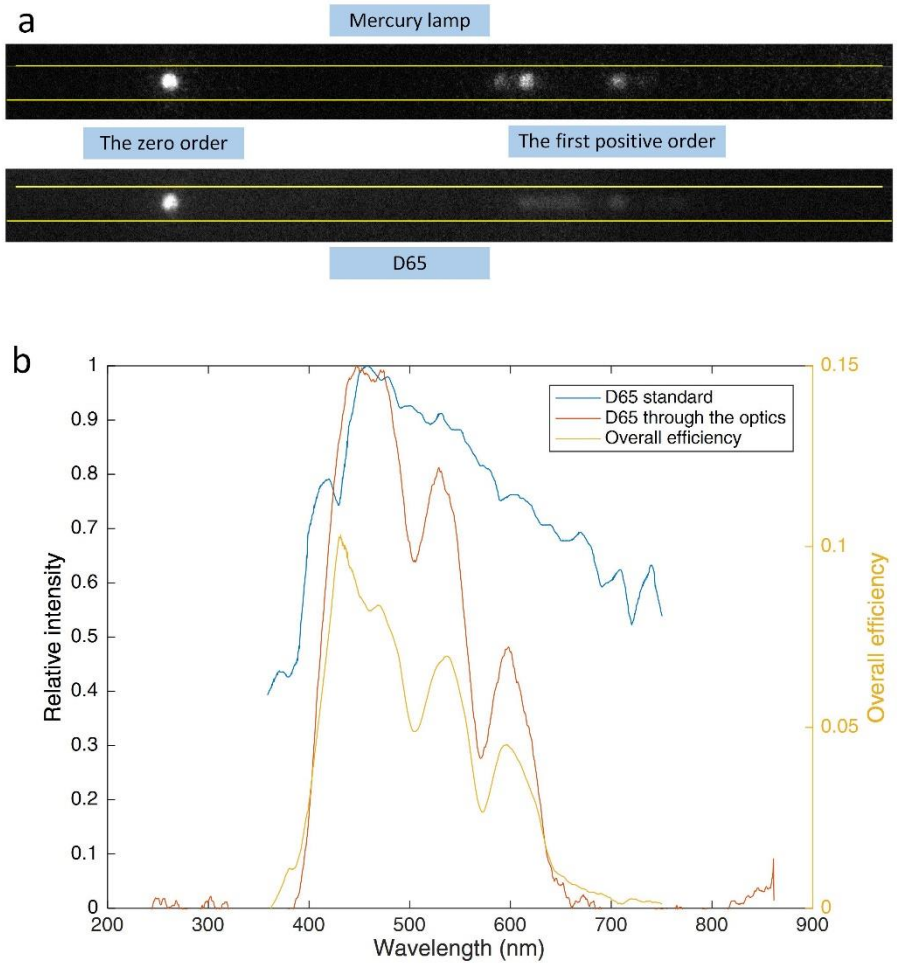

Figure 65 Overall efficiency of the optical system
(a) Mercury lamp vs. D65 light source through the optical system. (b) Overall efficiency.

7.3. Broad Band Spectrum and Plasma Temperature

Based on the literature reviews for SBSL, the spectrum is highly probable a featureless spectrum for aqueous solutions (*42*). As mentioned in previous chapter, gas doping is needed for promoting the light emission. Similarly, argon and air were utilized

respectively for shrimp-inspired device induced cavitation luminescence spectrum experiments. The gas doping procedure was the same as the light emission detection experiments. However, only the argon doped water case revealed spectrum which can be further processed, the air doped case light emission is too dim for spectrum analysis.

7.3.1. Argon Doped Distilled Water

With the ICCD exposure time set at 200 μs, gain voltage at 1000 Volts, a typical trial of the luminescing cavitation at first singularity is demonstrated in Figure 66a. The upper one is the ICCD grey scale image recorded at 12 bit (intensity 0-4095 counts), the lower one is the processed image with jet color map in Matlab for better visualization of the zero order and the first positive order. Since the first positive order is diffracted over a limited space range, a smearing light band with less brightness can be observed as shown in the processed color image. Compared with the mercury lamp calibration image at different position shown in Figure 66b, the spectrum can be extracted from the ICCD image with background subtracted.

The spectrum of the trial 14 cavitation luminescence is shown in Figure 67a, it is labeled as 'Experiment' and normalized. The actual spectrum excluding the effects of the optical system is dashed line labeled with 'Experiment with efficiency correction'. Since the overall efficiency in the wavelength range (smaller than 400 nm and larger than 650 nm) is too small, large uncertainties will be introduced into the spectrum conversion. Four blackbody radiation curve at T_{BB} = 1200K, 2400K, 4800K, 9600K, 19200K, and 38400K are illustrated along the converted spectrum with efficiency correction including a

potential curve with T_{BB}=14400K in dark blue dashed line. All curves are scaled to match at the 456 nm position, where the quantum efficiency of the intensifier can be measured accurately (20%). A zoom-in version of the graph can be seen in Figure 67b, in which the experimental data with efficiency correction located in the region between T_{BB} = 9600K curve and T_{BB} = 19200K curve, the potential T_{BB}=14400K curve seems to be in good agreement with the corrected spectrum.

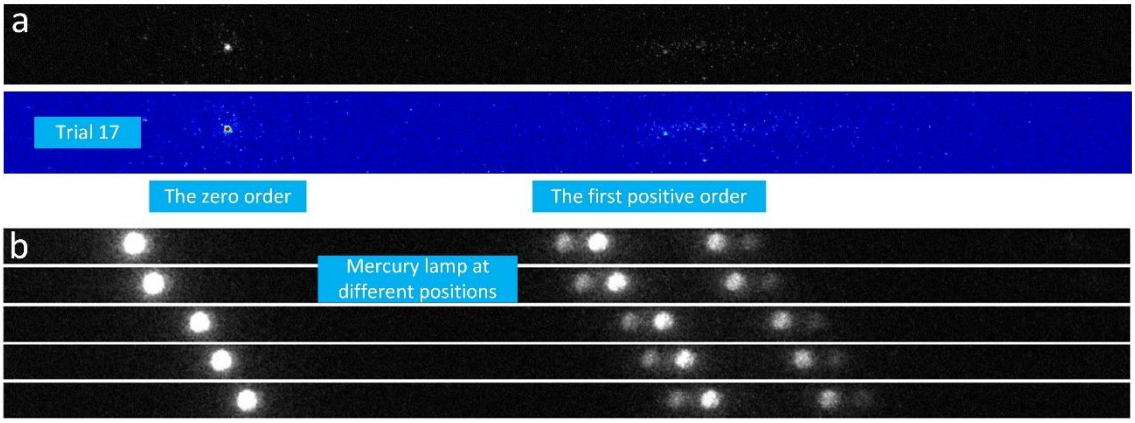

Figure 66 Typical trial of argon doped in distilled water
(a) Trial #14. (b) The mercury lamp calibration lines.

Due to the stochastic collapsing behavior of non-spherical cavitations, there were brighter light emission events compared to others. The average of all 21 useful spectra recorded in ICCD images could reveal the plasma temperature formed inside the collapsing cavitation induced by the shrimp-inspired mechanical device. As displayed in Figure 68, the blackbody temperature T_{BB} = 12,000 K radiation curve is in close agreement to the averaged spectrum estimation. The uncertainty of this method is relatively large compared to the two-line plasma pyrometer, the major constraints is the

quantum efficiency of the ICCD intensifier, with the maximum only reached 20% in the recorded data range.

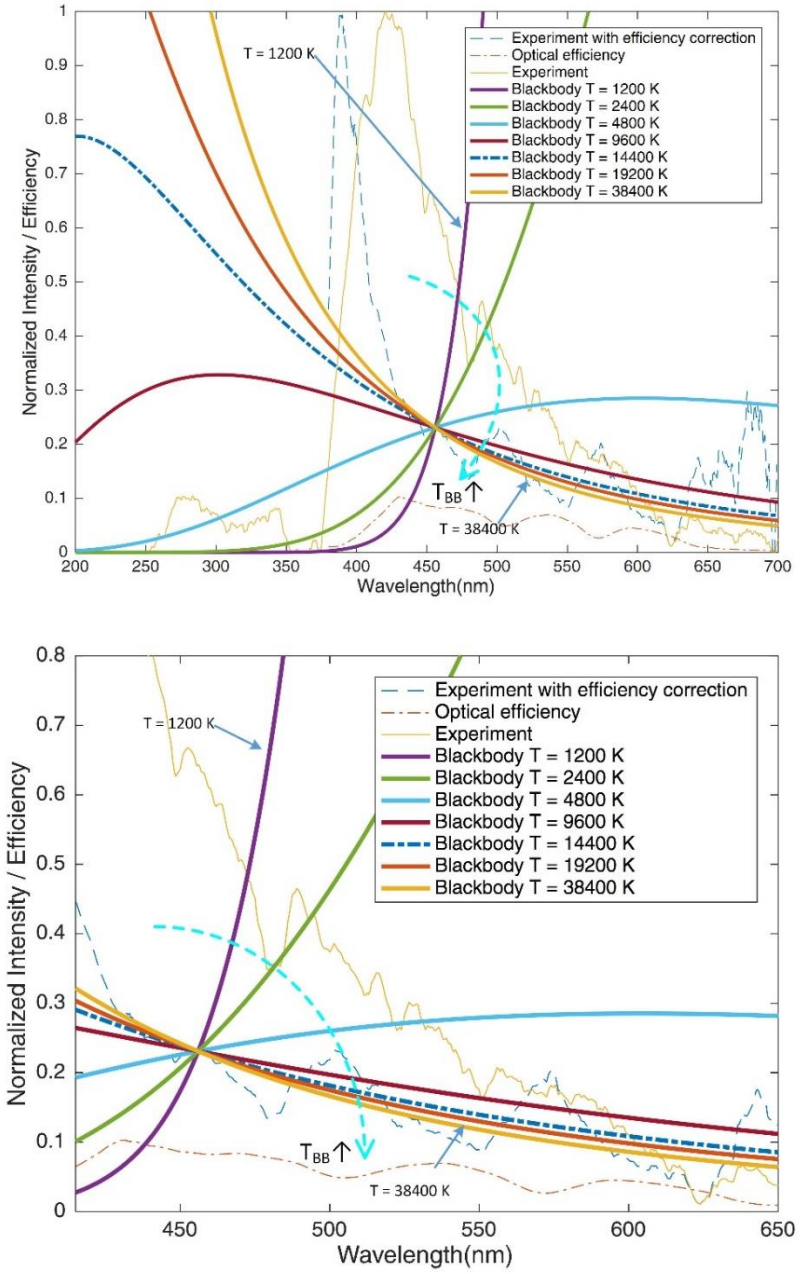

Figure 67 Trial 14 compared with blackbody radiation at different temperatures

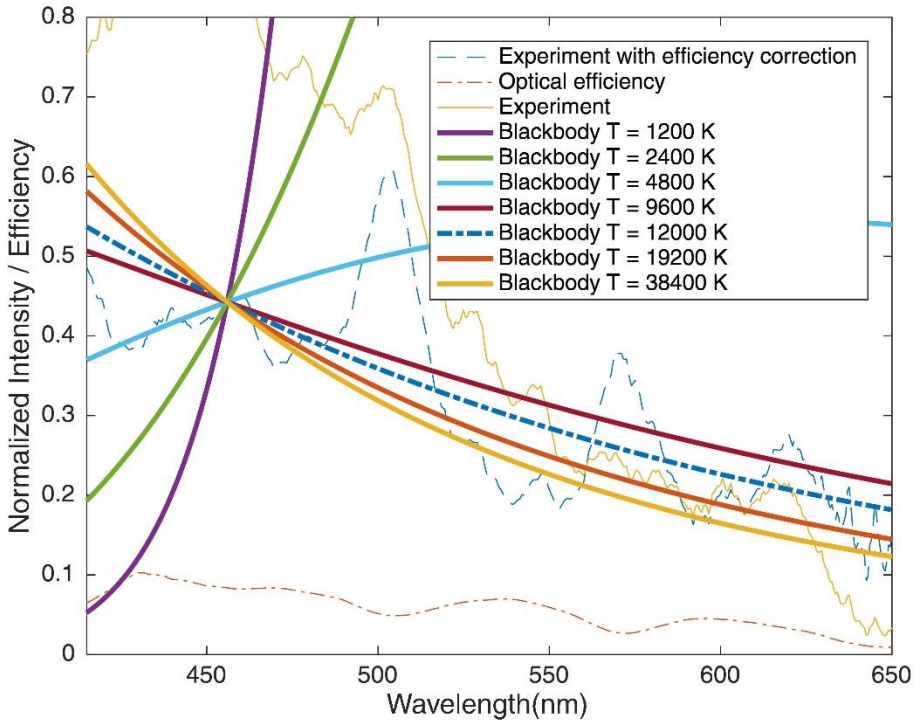

Figure 68 Averaged cavitation luminescence spectrum compared with blackbody radiation curves

For featureless broad band spectrum, the traditional way to estimate inner pressure of the plasma is using blackbody temperature from fitted curve coupled with complicated equations including bubble dynamics equation, heat mass transfer equation, equation of state and chemical kinematic equations numerical simulation for pressure or number density estimation. With the acquired argon plasma temperature data, and together with the number density predicted in literature n~10^{28} m^{-3}, the ionization degree of inside argon cavitation during first singularity is shown in Figure 69. The number density of 10^{28} m^{-3}

are labeled for each temperature condition. From rough estimation, the ionization degree for argon doped cavitation luminescence case is approximately 0.11%-2.3%.

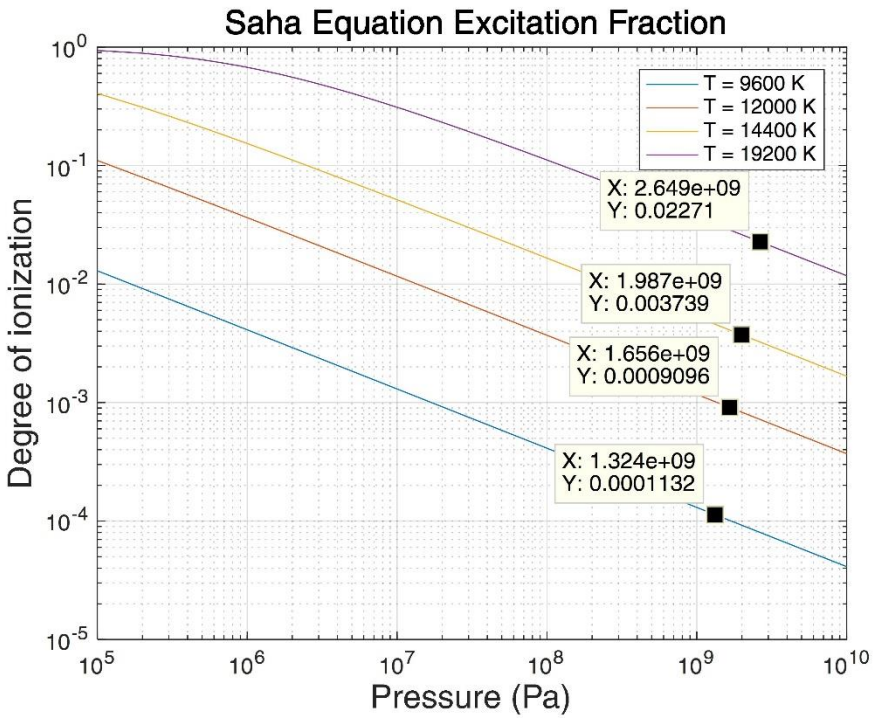

Figure 69 Degree of ionization for argon cavitation luminescence

7.4. Summary

The shrimp-inspired device generates broad band light emission, the 21 trials averaged spectrum has a blackbody temperature around 12000K (0.83-1.65 eV, 1eV ~ 11604.5 K), the ionization degree for the argon plasma is 0.11%-2.3% based on the number density at the order of n~10^{28} m^{-3}. Therefore, the estimated electron density is n_e~10^{25} or 10^{26} m^{-3}. Based on the optical system overall efficiency and solid angle of the achromatic lens occupied, the total number of photons emitted is ~10^6 for argon doped distilled water case.

The cavitation luminescence plasma regime is labeled in the red ellipse illustrated in Figure 70. It is on the edge of uncorrelated classical plasma and the strongly coupled plasmas. The estimation of plasma parameter Λ ranges from the order of 10^{-2} to 10^{2} further verified the classification of this plasma regime. In the rotating water hammer device combined with pulsed lasers targeting at the luminescing cavitation near singularities, Dr. Putterman's group (*39*) already provided experimental evidence for opaque plasma formation during cavitation luminescence. This opaque plasma could be a strongly coupled plasma due to the increase of Coulomb interactions.

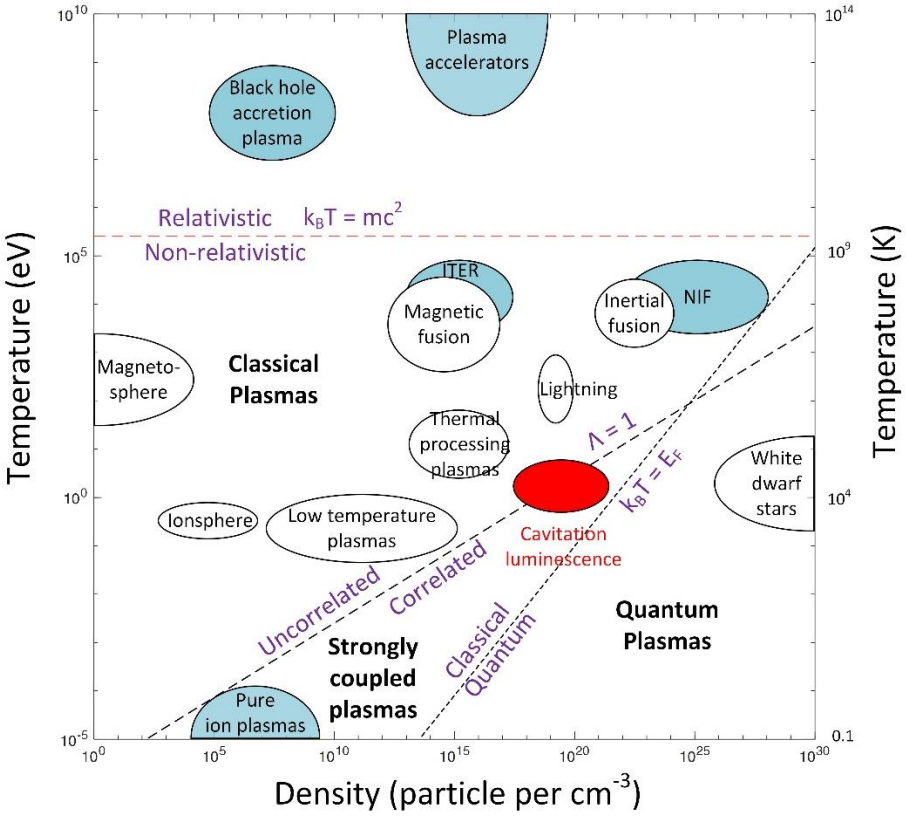

Figure 70 Plasmas generated during cavitation luminescence compared to other plasmas. (New areas of study since 1990 are indicated in blue, cavitation luminescence is indicated in red, x-axis density refers to electron/ion density) (*174*)

The cavitation luminescence phenomenon also shed light on the inertial confined fusion (ICF) research. For cavitation luminescence, the blackbody energy at the first singularity of the collapsing cavitation can be estimated based on the dimension of the cavitation luminescence in the zeroth order displayed in Figure 66a. The radius of the plasma generated indicated in the light emission image was around 100 μm, therefore the spherical volume of the first singularity was approximately $V = \frac{4}{3}\pi R_{min}^3 = 4.189 \times 10^{-12}$ m^3. Assuming the intracavity number density $n_o \sim 10^{28}$ $\#/m^3$, the mass inside the cavitation during first singularity can be estimated as $m_{cav} = n_o m_u M_{molecule} V = 1.26 \sim 2.8\ \mu g$, where m_u is the atomic mass, $M_{molecule}$ represents the molecule molar mass. The estimated blackbody energy is $E_b = m_{cav} C_v \Delta T \approx 25.2\ to\ 56\ mJ$ with the temperature difference $\Delta T \sim 20{,}000\ K$ and constant volume heat capacity $C_v \sim 2\ J/(g * K)$. In sum, the energy density of the blackbody inside cavitation first singularity is around $1.34 \times 10^{10}\ J/m^3$. For ICF, the energy density was on the order of $3.62 \times 10^{12}\ J/m^3$ based on the experimental data (eight 0.35 μm wavelength Nova laser with total energy 20 kJ, the target hohlraum has a diameter of 1.6 mm and a length of 2.75 mm) from Hsing and Hoffman (*175*) in 1997. According to the most recent public information of National Ignition Facility (NIF), the 192 laser beam energy achieved 2.15 MJ in 2018, the hohlraum cylinder with 9 mm height and 5 mm diameter, therefore the energy density of NIF was $3.04 \times 10^{12}\ J/m^3$.

Based on the estimations, the energy density of cavitation luminescence phenomenon is only 2 to 3 order of magnitude less than ICF. The total cost of achieving cavitation luminescence in laboratory condition (atmospheric pressure, room temperature)

is tiny compared to ICF, thus an alternative low cost method using cavitation luminescence could be implemented for ICF research. And another interesting topic in common for both research fields are the hydrodynamic instability such as Rayleigh-Taylor instability on the energy focusing efficiency for approaching higher energy density inside the hohlraum.

8. OPERATING IN OTHER LIQUIDS AND SCALE UP MORE

> We can think of nature as a designer and distill design rules accordingly. The central reason for the study of bioinspired engineering is to expand the design space of possible engineering solutions.
>
> --- Christopher Jenkins (*173*)

This chapter will discuss some interesting research directions for the shrimp-inspired device. The operation of the device in other liquids, for example organic liquids, and effects of viscosity, surface tension change for the cavitation behavior. Additionally, a 25 times of scaled up shrimp-inspired device is presented to push the limits of the bioinspired design where no such size snapping shrimp exists in nature as far as we know.

8.1. Shrimp-inspired Device in Other Liquids

As mentioned in the previous chapter, one of the advantages of shrimp-inspired device is that it can operate in liquids where the living snapping shrimp cannot. A typical example is shown in Figure 71 to demonstrate the operation of the mechanical device in pure glycerin/Glycerol ($C_3H_8O_3$). With the density 1260 kg/m^3, viscosity 950 mPa*s, (as listed in Table 6), viscous forces play a more important role in pure glycerin operation. The Reynolds Number between the two liquids assuming same device at same flow speed, $\frac{Re_w}{Re_g} = \frac{\rho_w \mu_g}{\rho_g \mu_w}$ ~750, therefore the turbulent flow in water could be laminar flow with the same fluid velocity.

Figure 71 Shrimp-inspired device operating in pure glycerin with double 1 angle 3 torsion spring configuration

Due to the dominance of viscous drag, the double 1 angle 3 configuration did not generate a cavitation with a larger closure time $t_{closure}$~3.8 milliseconds. This is an interesting test to show the ability of the shrimp-inspired device though no cavitation is generated.

Another typical example is the device operation in 99% ethanol, the property ethanol is listed in Table 6. Assuming the same device operating at the same flow velocity, the Reynolds Number of these two cases are almost matching with $\frac{Re_w}{Re_e} = \frac{\rho_w \mu_e}{\rho_e \mu_w}$ ~1.48. Based on the high frame rate video stills, similar cavitation was observed compared to same spring setup and releasing angle in water. However, the cavitation bubble seems

cloudier after the first singularity compared to that in water, indicating the effects of surface tension (σ_e/σ_w~0.3036).

Table 6 Liquid properties comparison

Liquid name	Formula	Density [kg/m^3]	Viscosity [mPa*s]	Vapor pressure [Pa]	Surface tension [mN/m]	Flash point [°C]
Water	H_2O	998	1.0016	2338@20°C	72.8	-
Ethanol	C_2H_5OH	789	1.1734	5826@20°C	22.1	14
Glycerin	$C_3H_8O_3$	1260	950	0.01@25°C	64.0	176

The two example fluids presented here are combustible, with auto-ignition temperature 393 °C and 383 °C for glycerin and ethanol respectively. Though the compression process of the collapsing cavitation increases the ethanol temperature inside over the auto-ignition temperature, it is still safe from combustion due to no oxygen available near the ethanol cavitation.

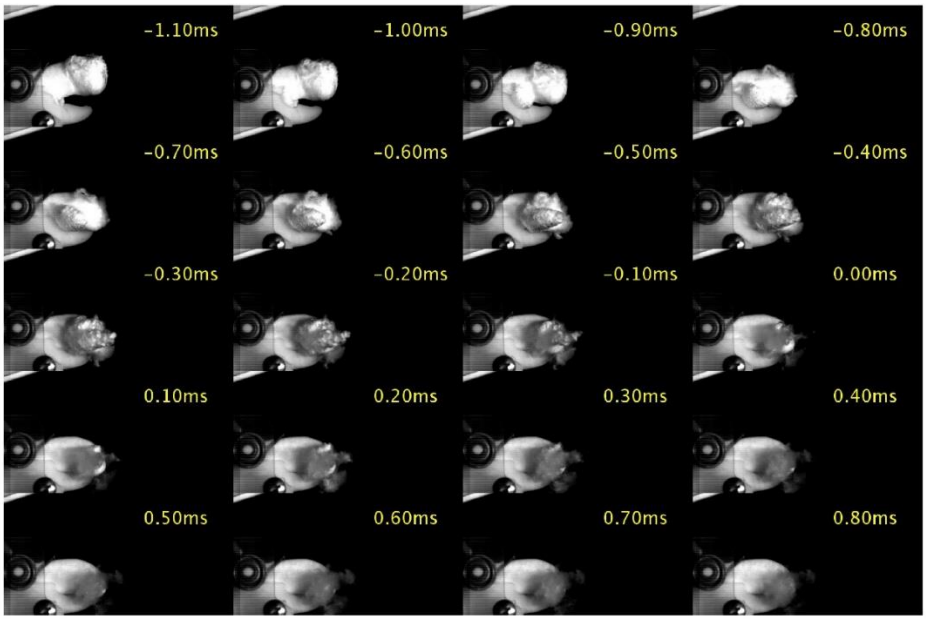

Figure 72 Shrimp-inspired device operating in 99% ethanol with double 1 angle 3 torsion spring configuration

8.2. 25X Scaled-up Large Claw Device

This section will discuss the scale-up effect on the shrimp-inspired device. The aforementioned shrimp-inspired mechanical device was designed based on the of 5 times scaled-up accurate claw morphology, whereas a new 25 times scaled-up shrimp-claw device will be introduced. The interesting question is whether the hydrodynamic flow induced cavitaion mechanism is still effective or not.

The essential geometry of the shrimp claw was inherited but the size is scaled up to the level a living snapping shrimp can never achieve so far. This 25 folds size difference is in exceed of the shrimp's interspecies size variation between the fully grown shrimp. As far as we know, there is no such size of snapping shrimp that can have a dactyl plunger at the length of ~ 120 mm. The CAD design model of the 25X shrimp claw is shown in Figure 73a, and the 3D printed device with a 122 mm dactyl plunger is demonstrated in Figure 73b.

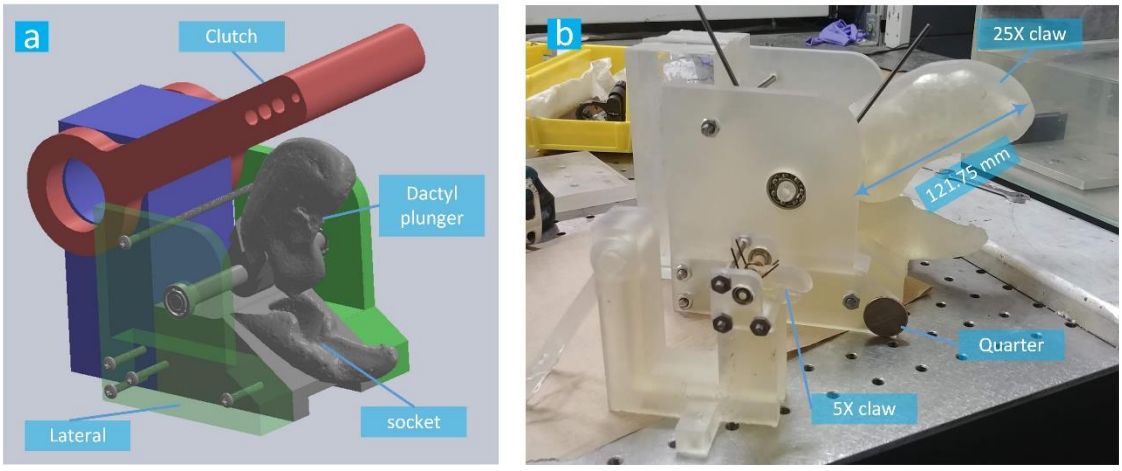

Figure 73 Scaled-up 25 times large claw design
(a) CAD design. (b) 3D printed 25X claw compared to 5X claw.

8.2.1. Atmospheric Pressure Operation

The cavitation generation process of the 25X shrimp-inspired device with two torsion springs (9271K115 and 9271K116 from McMaster-Carr with torsion spring constant around 2.466 N*m/rad) are shown in the high frame rate video stills in Figure 74. The closing time of the claw at this condition is approximately 21 ms, which is hard to see in the high frame rate video due to the enormous size exceeding the camera lens at 50,000 fps. A large solitary cavitation bubble was generated by the high-speed jet issued from the socket can be spotted and later collapsed and rebounded several times. This proved that our 25X scaled up shrimp-inspired design can operate with cavitation generation successfully, and the physics behind is exactly the same as our 5X device.

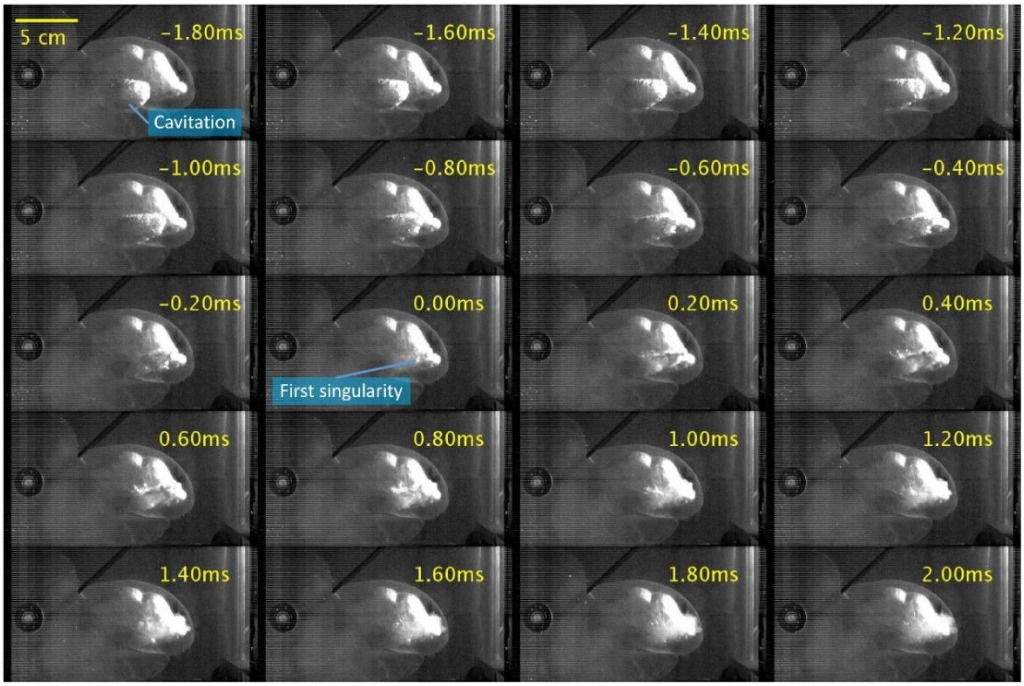

Figure 74 Scaled-up large claw device operation in tap water and 1 atm pressure with double 2 (single spring constant κ = 2.466 N*m/rad) torsion spring

Another modification introduced for the new design is making the dactyl plunger hollow which reduces the momentum inertia value which is one of the major parameters in the simplified ODE model for design guidance. Due to the large size of the claw, gravity and buoyancy forces should also be included for the modeling. With the stills from the high frame rate video, the cavitation bubble dynamics can be extracted for further analysis. Different time varying radius data are plotted in Figure 75.

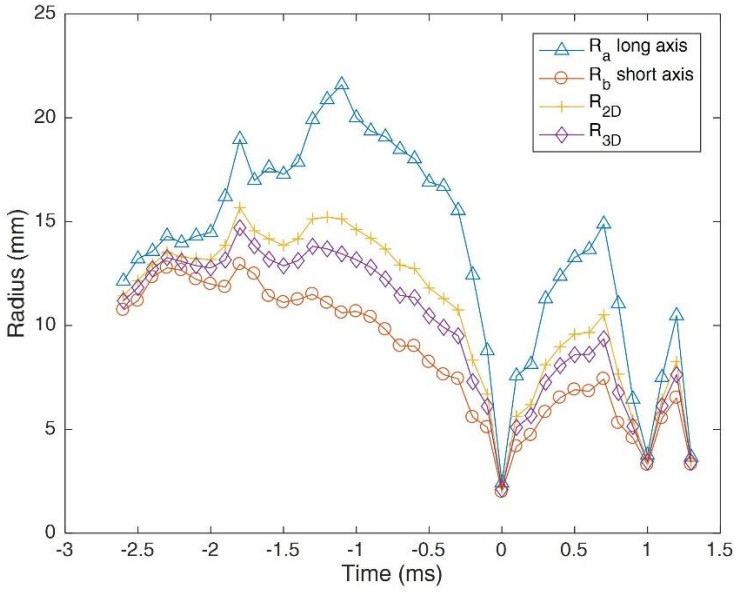

Figure 75 Scaled-up shrimp device cavitation bubble dynamics at 1 atm

In the figure legend, R_a is half the length of the major axis which assuming the cavitation shape observed from side view is an ellipse. And R_b is the half length of minor axis, R_{2D} represents the area equal equivalent radius and R_{3D} is the volumetric equal equivalent radius which assuming the other half length of the axis $R_a = R_c$. Since no extra high speed camera was available to record the top view and side view operation at the

same time, thus there could be extra discrepancy in R_{3D} data. However, the overall trend of the cavitation bubble dynamics can be deduced.

Another crucial parameter is the cavitaion front speed, which can be employed to estimate the speed of the water jet for cavitation generation. The time varying cavitation front position is labeled with red cross marker to reveal the trace of the tracking point, as illustrated in Figure 76a. With the coordinates of the tracking point positions, the cavitation front speed is exhibited in Figure 76b, with a maximum speed around 32 m/s.

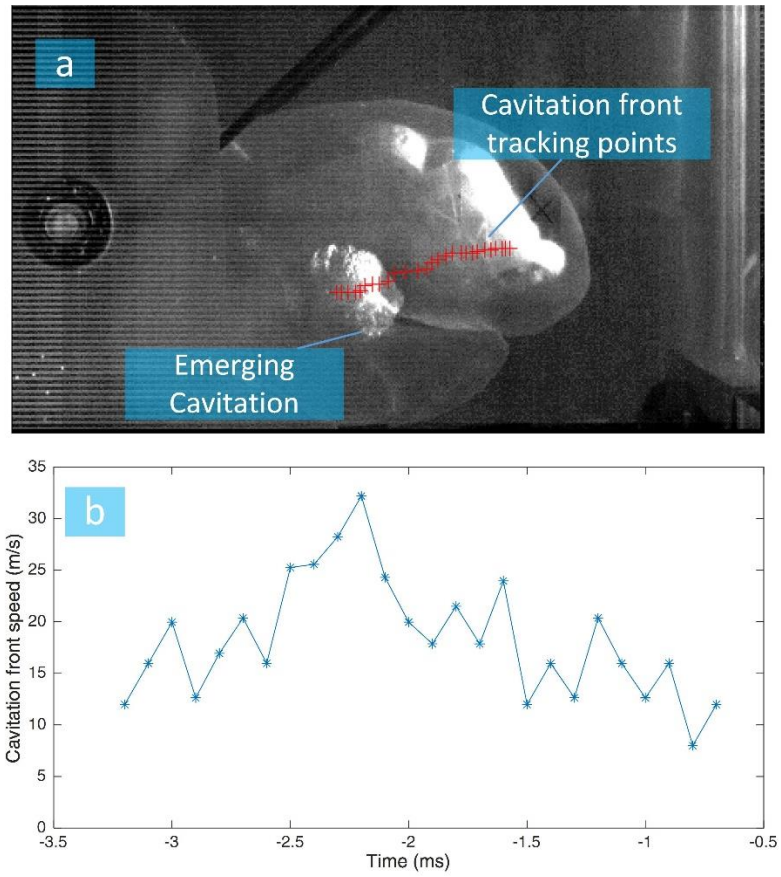

Figure 76 Cavitation front speed at 1 atm
(a) Cavitation front track. (b) Cavitation front speed.

Though the speed of the cavitation front is no longer larger than the critical speed ~14 m/s to initiate the cavitation in atmospheric condition, the cavitation still existed till the final collapse. The corresponding Cavitation Number is estimated in Figure 77.

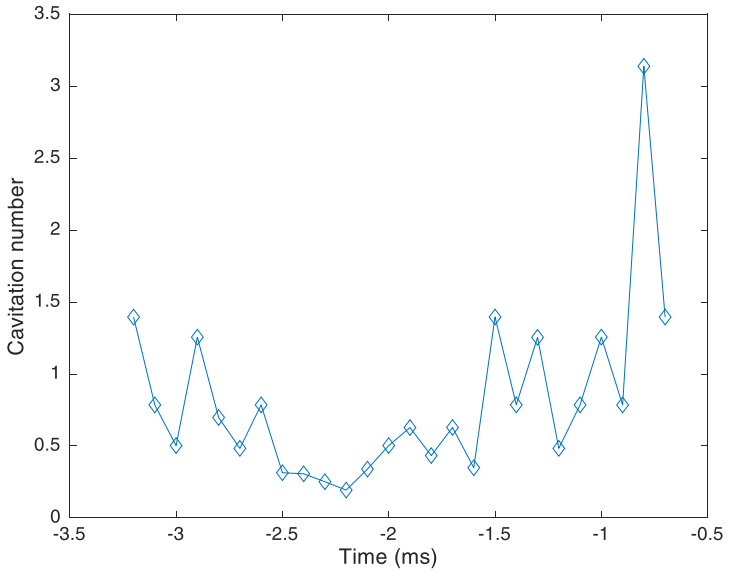

Figure 77 Cavitation Number for 25X shrimp claw device with double 2 torsion spring (single spring constant κ = 2.466 N*m/rad) configuration at 1 atm

8.2.2. Lower Pressure Operation

In atmospheric pressure operation, the onset of cavitation happens at Cavitation Number $Ca = (p - p_{vap})/(0.5\rho v^2) = 1$, at which the flow velocity approaching ~14.08 m/s. Based on the shrimp device design guiding principle, the crucial Cavitation Number need to be lower than one for the jet-induced cavitation to form. One of the easy access is reducing the pressure difference between local pressure and liquid vapor pressure. Changing vapor pressure involves changing temperature or liquid itself which is relatively expensive compared to changing the ambient pressure. Therefore an easy proof of concept

low pressure chamber was manufactured with a metal plate and proper sealing (silicone gasket and vacuum grease) on top of an acrylic tank inherited from undergraduate senior design project. A quick-clamp vacuum feedthrough was attached to the metal plate together with a mechanical vacuum gauge, as shown in Figure 78.

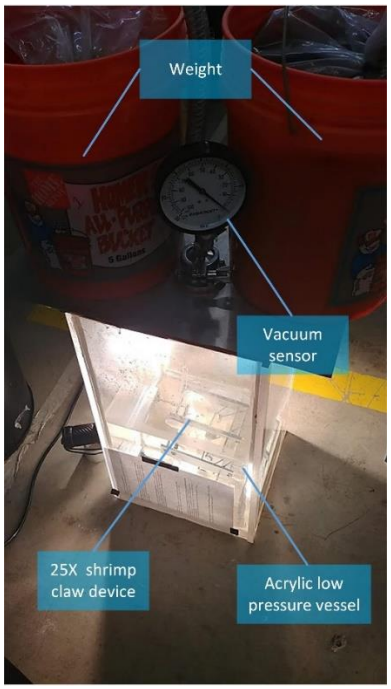

Figure 78 Vacuum vessel for low pressure operation

Before operation of the large claw device in low pressure vessel, vacuum pump was turned on to make the vessel inner pressure at ~45 kPa. A long string attached to the clutch was pulled out of the acrylic vessel through the gasket and sealed with vacuum grease and pressured silicone rubber. When inner pressure stabilized at setting point, the high frame rate camera was set at filming status with a high power front-lit high frequency LED light source. Right after the camera start recording, the string was pulled to release the clutch for cavitation recording. Heavy weight was needed for improving the seal of

the low pressure vessel. A typical low pressure operation trial of the shrimp-inspired large claw device at 45 kPa is demonstrated in Figure 79. Since the viscosity of water was almost the same, the closure time of the claw was also remained ~ 21 ms. And side cavitation on the rotating dactyl plunger was also observed due to the cavitation onset flow speed changed to 9.25 m/s at 45 kPa.

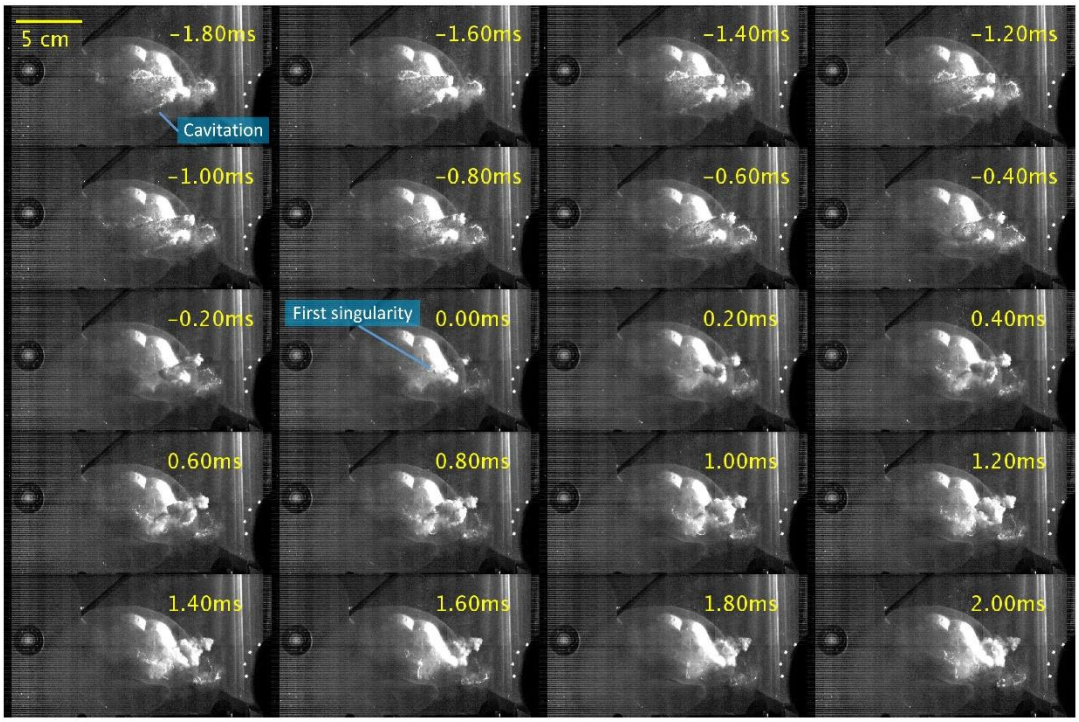

Figure 79 Scaled-up large claw device operation in tap water at 45 kPa with double 2 torsion spring recorded at 50,000 fps.

The cavitation bubble size was larger based on the cavitation bubble dynamics shown in Figure 80. The different methods of bubble radius estimation resulted into different cavitation bubble dynamics curves for the non-spherical collapsing cavitation. Based on the R_{3D} estimation which employed the volumetric equivalent radius of the ellipsoidal cavitation shape assuming two equal short axis, the cavitation conversion

efficiency was 20.9% for atmospheric pressure operation and 15.2% for 45 kPa low pressure operation with double 2 torsion spring configuration, as listed in Table 7.

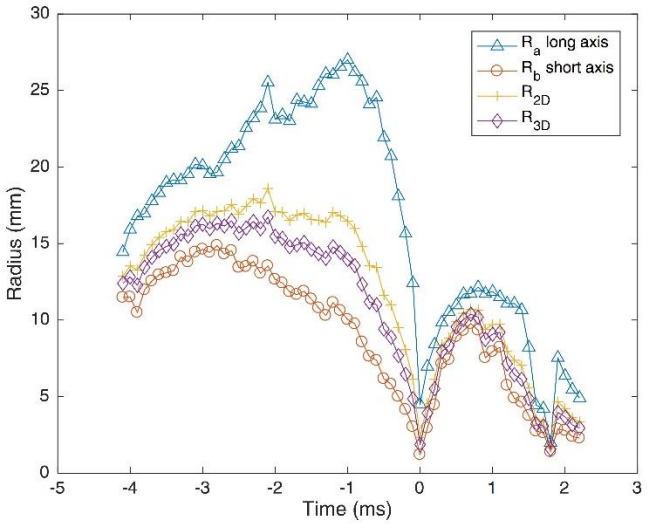

Figure 80 Scaled-up shrimp device cavitation bubble dynamics at 45 kPa

Table 7 Cavitation conversion efficiency for 25X shrimp device

Pressure	k [N*m/rad]	Input Energy [J]	R_{max} [mm]	Bubble energy [J]	Conversion efficiency
1 atm	2.466	6.31	14.7	13.2	20.9%
45 kPa	2.466	6.31	17.5	0.96	15.2%

The cavitation front trace and instantaneous speed of the low pressure operation in side view is displayed in Figure 81a and b respectively. And due to the change of pressure, the Cavitation Number Ca plotted in Figure 82 is relatively smaller than $Ca = 1$ for longer time. This also correlated to the lifetime of the cavitation (from showing up in the nozzle-shaped channel to the first singularity) in low pressure (~ 5.5 ms) is longer compared to atmospheric pressure case (~7.1 ms). The duration of the cavitaion before first singularity data were estimated from the high frame rate videos for both cases.

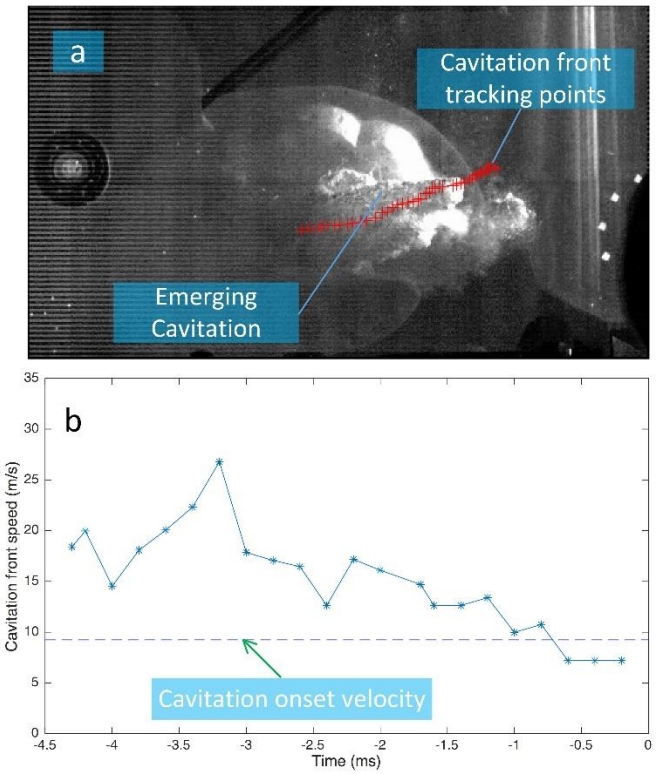

Figure 81 Cavitation front speed at 45 kPa
(a) Cavitation front track. (b) Cavitation front speed.

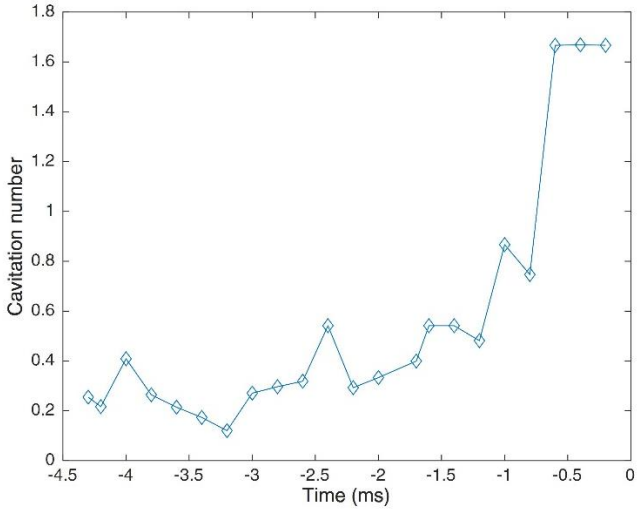

Figure 82 Cavitation Number for 25X shrimp claw device with two intermediate torsion spring configuration at 45 kPa

To sum up the 25X large claw device section, the same methodology of bioinspired design is still successful on the scale-up 25X device. By reducing the ambient pressure, the cavitation size increased about 1.7 time in volume with the pressure reduced to 44.4% of original pressure. The compression ratio of maximum volume to minimum volume captured in the high frame rate video data is on the order of 1000, the actual compression ratio is indeed higher and it could be estimated with the light emission volume during the first singularity. With the large cavitaion size, the moving cavitation with ripple-like perturbations on the interface of water vapor and liquid water can be observed in further detail, and this Kelvin-Helmholtz type instability will break the cavitation into several smaller ones during the collapse. Due to the water vapor and liquid flow velocity is hard to measure, this is an interesting research topic for two-phase flow CFD simulation on large non-spherical cavitation collapse.

9. CONCLUSIONS

9.1. Overall Summary

Looking back to the dissertation statement of Chapter 1, the experimental results presented in this dissertation prove that the bioinspired design methodology fulfil the design purpose successfully. With the shrimp-inspired synthetic device, the cavitation generation, underwater shock wave formation, and light emission are all reproduced by the mechanical device compared to the living shrimp's cavitation luminescence phenomenon. There are definitely better range of the design parameter space that can contribute to better hydrodynamic cavitation, and further result in stronger light emission, indicating of higher plasma temperature achieved inside the collapsing cavitation bubble.

Extensive literature review in Chapter 2 on cavitation luminescence laid out the foundation for this dissertation. In general, the cavitation luminescence phenomenon can be divided into the following categories: hydrodynamic flow induced cavitation luminescence, ultrasonic sound induced sonoluminescence, laser-induced cavitation luminescence in liquid, and electric discharge induced cavitation luminescence. The scope of this dissertation is the hydrodynamic flow induced cavitation luminescence, whereas experimental and theoretical studies in other categories still have a lot in common. Chapter 3 summarized the details of the design process, revealing guiding principles of the bioinspired design of the shrimp claw device. And Chapter 4 focused on the cavitation bubble dynamics with variation of parameters such as torsion spring constant, releasing angle. And the underwater shock wave using schlieren imaging technique verified the source of the snap noise actually comes from the energy focusing process, which is the

collapsing cavitation, not the snapper claw impact. The first direct photo of shrimp cavitation luminescence was demonstrated in Chapter 5 with the shrimp device at the same living condition of the shrimp. The high efficiency of the bioinspired device on cavitation conversion make it special for applications where high efficiency is one of the major priority. Chapter 6 compared the cavitation conversion efficiency among different techniques and demonstrated the bioinspired mechanical device is 3~2000 times way more efficient, which is benefitted from evolutionary pressure for the long natural history since the existence of the snapping shrimp species. Chapter 7 focused on the temperature measurement of the inertially confined plasma inside the imploding cavitation bubble with the non-intrusive OES method. And Chapter 8 explores more in design space with different liquids and larger scale-up factors. The interesting results will lead to new ideas for continuing and future work.

9.2. Guiding Principle for the Bioinspired Design

As mentioned in Chapter 3, the failed experience of similar clutch device with 2D claw design based on mid-plane curve did not result in expected results. The high-speed water jet induced cavitation was not spotted. This addressed the prominent effects of the snapper claw morphology. The simplified ODE model for practical prediction can be used for design iteration guidance. It also reveals several major physical parameters for the time varying dactyl tip speed or angular velocity, for example, the momentum inertia of the rotating dactyl plunger, the fluid drag, and torsion spring driving force. Reducing the

momentum inertia can reduce the spring load and improve the integrity of the device, this is also the reason we make the 25X dactyl plunger partially hollow.

The level of the biomimicry in our morphologically accurate device is relatively high compared to other bioinspired functional structures and devices like the 2D version claw shrimp device (*148*) and the Ninjabot (*149*). However, it is relatively lower than the biohybrid morphing wings with bird feathers (*176*). This suitable small level of the paradigm shift is key to the success for reproducing the snapping shrimp's cavitation generation process. Traditional bioinspired distilled design using microscale/macroscale structures or mechanism in nature will not always end up with fruitful results due to the paradigm shift is too large. Based on the lessons learned from successful design of our device, we can move on to more distilled version of bioinspired design paradigm (lower level of biomimicry) with better chance of success.

Another important aspect of the design is the complex geometry was only feasible with the development of additive manufacturing, as known as the 3D printing technology. Studies on the material characterization and composition structures (*154*, *177*, *178*) of snapping shrimp snapper claw and mantis shrimp appendage (*5*) reveal the secret of the biomaterial chitin and keratin with high impact endurance as a different branch of bioinspired engineering for material science. Whereas we proved that even with ordinary 3D printing material such as white strong plastic on Shapeways, the morphologically accurate mechanical device can still work successfully alongside with cavitaton impact in which a high temperature plasma was inertially confined. The ODE model for predicting

plunger tip speed and angular velocity was a legitimate simplification which addresses the free body diagram during the dactyl plunger snap shut process.

The limitations on the 3D printed bioinspired device are also related to the materials. For operating in different liquid, the spring music wire material and the 3D printed socket and plunger material need to be compatible with the liquid.

9.3. Cavitation Bubble dynamics and the Plasma Characterization

Since the major cavitation is non-spherical, estimating the cavitation volume precisely is always challenging with only one high speed camera. The maximum volume of the cavitation during bubble dynamics is essential for energy focusing since the mechanical potential energy of the bubble is the input energy. If the collapsing cavitation will collapse at a single site and it is not affected by other neighboring cavitations, the larger maximum radius before first singularity at same ambient conditions, the more intense collapsing will occur at the first singularity. Additionally, for non-spherical collapsing cavitation, the topology of the cavitation shape and the instabilities on the liquid-vapor interface may break the cavitation and reduce the energy focused in the imploding bubble, such as the Rayleigh-Taylor instability and the Kelvin-Helmholtz instability on the cavitation interface.

The LTE plasma formed inside the cavitation of aqueous liquid is mostly broad band emission. One non-intrusive method of probing the plasma temperature is the optical emission spectroscopy method. A blackbody temperature for the optical thick plasma can be acquired with the luminescing cavitation spectrum. If emission lines are observed, the

intensity ratio of the two emission lines can be used as a plasma pyrometer to measure plasma temperatures and the broadening and shift of emission lines to estimate the pressure of the plasma. The experimental results indicated that the blackbody temperature of the plasma for argon doped distilled water is ~12,000 K.

The limitation for this plasma characterization technique in this case is the dim light challenge. And the overall optical system efficiency is relatively low, especially the photocathodes quantum efficiency of the ICCD intensifier. Possible methods for improving the light emission are using different liquids and doped gas for better signal-to-noise ratio, collecting large amount of dim light spectrum images over a long time for spectrum analysis. The jitter of the collapsing event in space and time may make the image data process more sophisticated. With the plasma temperature data, the pressure can be estimated with numerical modeling of RPE together with complicated chemical kinetics, mass diffusion model, and microscale thermodynamics for the gas mixture during the bubble dynamics.

Based on what we have learned and observed from this dissertation research, I would like to conclude this research topic with a few points below:

1. We have proposed a methodology based on bioinspired engineering design to reproduce the snapping shrimp's plasma generation technique, and eventually the experimental results provided solid proof that the methodology is successful.
2. Collapsing cavitation is an effective energy focusing process, in this dissertation research, we have reported, to our knowledge, the world's first

direct imaging of the luminescing cavitation generated by the shrimp-inspired device at its first singularity.

3. The cavitation bubble dynamics, schlieren imaging of the underwater shock wave provided direct proof of where the snap noises come from. The hydrodynamic flow induced cavitation also revealed more details of the shrimp snapping behavior.
4. The imploding bubble confined plasma light emission spectrum is broad band, and the black body radiation temperature of the spectrum indicated a thermal plasma was generated.
5. The cavitation conversion efficiency of our bioinspired device is 3~2000 times higher than other type of cavitation generation methods, by sound, electricity, and laser light. For this type of LTE plasma generation, the plasma efficiency is directly dependent on the cavitation conversion efficiency, therefore this thermal plasma generation efficiency is also high.
6. The bioinspired device provided application possibilities in a broad range of disciplines: chemistry, physics, material processing, etc.

9.4. Future and Continuing Work

The successful methodology of learning from nature's design and distill it for different engineering applications just open the door for a large scope of science and engineering applications. Here we sum up several potential research directions for future and continuing work.

9.4.1. Automatic Snapping Device: the robotic shrimp

In order to enable the shrimp-inspired device operating under different gas content, different liquid, and various pressures, a robotic shrimp device with the ability of generating cavitation in 0.83 Hz was designed and manufactured, as shown in Figure 83.

For the design of an automatic snapping device, a snapping shrimp robot, the plunger material strength is the main constriction for the pinion gear to actuate dactyl gear. The impact strength from the pinion gear cam and the dactyl gear may fail after 30 mins continuous snapping with 3D printed plastic. The 3D printed aluminum dactyl gear part suffered from mechanical wear due to the stress endured is larger than the material yield limit and carbon steel plunger need stronger torsion springs to produce similar size cavitation. Titanium is ideal for this case and worth trying, however, the price of 3D printed titanium is expensive.

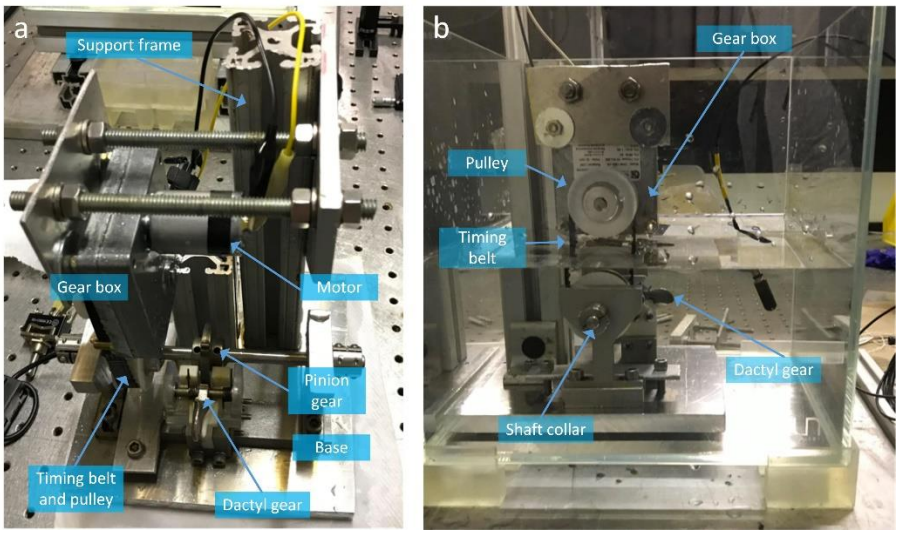

Figure 83 Robotic snapping claw device. (a) Top angle view of the automatic snapping device. (b) Side view of the device running under water

With this automatic snapping robot, a large number of repetitions and long-time operation are available, therefore water treatment and material synthesis using bioinspired device is practical. This device will also help the shrimp plasma characterization for temperatures and pressures inside the collapsing cavitation measurement. Another interesting research direction is the cavitation behavior in different pressures, a way of changing the Cavitation Number, the robotic shrimp can produce a more spherical and huge size cavitation in low pressure. One typical example of the device operating in low pressure can be seen in the Figure 84.

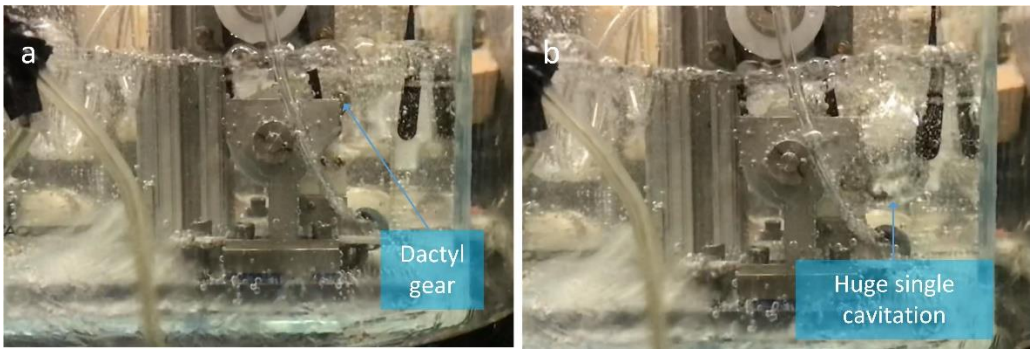

Figure 84 Huge cavitation generated by the shrimp robot at low pressure test
(a) Dactyl plunger at cocked position. (b) Huge cavitation generated by the robotic claw.

9.4.2. Distilled Design with Artificial Morphology

The long dactyl plunger of the snapper claw is useful for the shrimp, however, it may not be crucial for single solitary cavitation bubble generation due to the cavitation onset at the tip or near side of the rotating dactyl part. To move on to a lower level of biomimicry, which means more distilled design, artificial streamlined shape or topology

other than the snapper claw dactyl morphology can also work and produce larger cavitation with shorter length and smaller momentum inertia.

This part of design work definitely need three-dimensional CFD simulations to guide the streamlined shape design and a lot of fluid dynamics research could be done on this direction.

9.4.3. Promoting the Light Emission Signal for OES

The shrimp plasma characterizations are interesting, however the dim light emitted from the shrimp cavitation luminescence is still challenge for using OES as an effective plasma pyrometer. Despite of this, different liquids can be used for characterization of the inertially confined plasma inside the imploding bubble. Potential liquids we can try in the future for promoting the light emission signal is Dibutyl phthalate since the cavitation luminescence intensity (photons per flash) is four orders of magnitude stronger than water based on the water hammer device cavitation luminescence experiment from Chakravarty et al. (*82*).

REFERENCES

1. A. Piel, *Plasma physics: An introduction to laboratory, space, and fusion plasmas* (2010).
2. I. Langmuir, Oscillations in Ionized Gases. *Proc. Natl. Acad. Sci.* **14**, 627–637 (1928).
3. A. Fridman, *Plasma Physics and Engineering* (CRC Press, 2004).
4. D. J. Flannigan, K. S. Suslick, Inertially confined plasma in an imploding bubble. *Nat. Phys.* **6**, 598–601 (2010).
5. M. P. Brenner, S. Hilgenfeldt, D. Lohse, Single-bubble sonoluminescence. *Rev. Mod. Phys.* **74**, 425 (2002).
6. Y. P. Raizer, *Physics of Gas Discharge* (Springer Verlag. Berlin., 1991; http://www.springer.com/jp/book/9783642647604#aboutBook).
7. D. Lohse, B. Schmitz, M. Versluis, Snapping shrimp make flashing bubbles. *Nature*. **413**, 477–478 (2001).
8. C. Camara, S. Putterman, E. Kirilov, Sonoluminescence from a single bubble driven at 1 megahertz. *Phys. Rev. Lett.* **92**, 124301 (2004).
9. D. J. Flannigan, K. S. Suslick, Plasma line emission during single-bubble cavitation. *Phys. Rev. Lett.* **95**, 44301 (2005).
10. M. Versluis, B. Schmitz, A. von der Heydt, D. Lohse, How snapping shrimp snap: through cavitating bubbles. *Science*. **289**, 2114–2117 (2000).
11. D. J. Flannigan, S. D. Hopkins, C. G. Camara, S. J. Putterman, K. S. Suslick,

Measurement of pressure and density inside a single sonoluminescing bubble. *Phys. Rev. Lett.* **96** (2006), doi:10.1103/PhysRevLett.96.204301.

12. X. Tang, D. Staack, Bioinspired mechanical device generates plasma in water via cavitation. *Sci. Adv.* **5**, eaau7765 (2019).
13. S. L. Miller, A production of amino acids under possible primitive earth conditions. *Science (80-.).* **117**, 528–529 (1953).
14. F. Fraunberger, *Illustrierte Geschichte der Elektrizität* (Aulis-Verl. Deubner, 1985).
15. H. Bradt, Supplement to Chapter 4 of Astrophysics processes: the physics of astronomical phenomena (2009), (available at http://homepages.spa.umn.edu/~kd/Ast4001-2015/NOTES/n052-saha-bradt.pdf).
16. S. Samukawa *et al.*, The 2012 Plasma Roadmap. *J. Phys. D. Appl. Phys.* **45**, 253001 (2012).
17. P. J. Bruggeman *et al.*, Plasma–liquid interactions: a review and roadmap. *Plasma Sources Sci. Technol.* **25**, 053002 (2016).
18. V. V. Rzevskii, Y. I. Protasov, *Electrical Methods of Rocks Destruction* (Nedra, Moscow, 1972).
19. A. A. Vorobiev, G. A. Vorobiev, Electric breakdown and destruction of solid dielectrics. *Vyshaya Shkola Moscow* (1966).
20. S. Pronko, G. Schofield, M. Hamelin, F. Kitzinger, in *Ninth IEEE International Pulsed Power Conference* (IEEE, 1993; http://ieeexplore.ieee.org/document/512866/), p. 15.

21. I. V. Lisitsyn, T. Muraki, H. Akiyama, Wire Induced Flashover as a Source of Shock Waves for Destruction of Solid Materials. *Jpn. J. Appl. Phys.* **36**, 1258–1263 (1997).

22. V. Lazic, S. Jovićević, Laser induced breakdown spectroscopy inside liquids: Processes and analytical aspects. *Spectrochim. Acta Part B At. Spectrosc.* **101**, 288–311 (2014).

23. J. Thornycroft, S. W. Barnaby, Torpedo-boat destroyers. *Minutes Proc. Inst. Civ. Eng.* **122**, 51–69 (1895).

24. Lord Rayleigh, VIII. On the pressure developed in a liquid during the collapse of a spherical cavity. *London, Edinburgh, Dublin Philos. Mag. J. Sci.* **34**, 94–98 (1917).

25. B. P. Barber, S. J. Putterman, Observation of synchronous picosecond sonoluminescence. *Nature*. **352**, 318–320 (1991).

26. R. Johnson, *Handbook of fluid dynamics* (CRC Press, ed. 2nd, 2016).

27. P. Jarman, Sonoluminescence: A discussion. *J. Acoust. Soc. Am.* **32**, 1459–1462 (1960).

28. P. D. Jarman, K. J. Taylor, Light emission from cavitating water. *Br. J. Appl. Phys.* **15**, 321 (1964).

29. F. B. Peterson, T. P. Anderson, Light emission from hydrodynamic cavitation. *Phys. Fluids*. **10**, 874–879 (1967).

30. K. Weninger, C. Camara, S. Putterman, Physical acoustics of ultrasound-assisted lipoplasty. *Clin. Plast. Surg.* **26**, 463–79, ix (1999).

31. J. H. J. van der Meulen, in *Joint ASCE/ASME Conference on Cavitation in Hydraulic Structures and Turbomachinery* (American Society of Mechanical Engineers, New York, 1986; https://ci.nii.ac.jp/naid/80002972133/), pp. 149–159.

32. J. H. J. Van der Meulen, Y. Nakashim, in *Proc. 2nd Int. Conf. on Cavitation* (Institution of Mechanical Engineers, London, UK, 1983; https://ci.nii.ac.jp/naid/20000217461/), pp. 13–19.

33. T. G. Leighton, M. Farhat, J. E. Field, F. Avellan, Cavitation luminescence from flow over a hydrofoil in a cavitation tunnel. *J. Fluid Mech.* **480**, 43–60 (2003).

34. M. Farhat, A. Chakravarty, J. E. Field, in *Proceedings of the Royal Society A: Mathematical, Physical and Engineering Sciences* (Royal Society, 2011), vol. 467, pp. 591–606.

35. C. Kranenburg, Gas Release During Transient Cavitation in Pipes. *J. Hydraul. Div.* **100**, 1383–1398 (1974).

36. M. Mitosek, Study of Transient Vapor Cavitation in Series Pipe Systems. *J. Hydraul. Eng.* **126**, 904–911 (2000).

37. J. Schmid, Kinematographische Untersuchung der Einzelblasen-Kavitation. *Acta Acust. united with Acust.* **9**, 321–326 (1959).

38. C.-K. Su, C. Camara, B. Kappus, S. J. Putterman, Cavitation luminescence in a water hammer: Upscaling sonoluminescence. *Phys. Fluids*. **15**, 1457–1461 (2003).

39. S. Khalid, B. Kappus, K. Weninger, S. Putterman, Opacity and transport measurements reveal that dilute plasma models of sonoluminescence are not

valid. *Phys. Rev. Lett.* **108** (2012), doi:10.1103/PhysRevLett.108.104302.

40. L. A. Crum, R. A. Roy, Sonoluminescence. *Phys. Today*. **47**, 22–30 (1994).

41. S. J. Putterman, K. R. Weninger, Sonoluminescence: How bubbles turn sound into light. *Annu. Rev. Fluid Mech.* **32**, 445–476 (2000).

42. K. S. Suslick, D. J. Flannigan, Inside a collapsing bubble: sonoluminescence and the conditions during cavitation. *Annu.Rev.Phys.Chem.* **59**, 659–683 (2008).

43. H. Frenzel, H. Schultes, Luminescenz im ultraschallbeschickten Wasser. *Zeitschrift für Phys. Chemie*. **27B** (1934), doi:10.1515/zpch-1934-0137.

44. R. W. Perry, A. Kantrowitz, The production and stability of converging shock waves. *J. Appl. Phys.* **22**, 878–886 (1951).

45. K. Taylor, P. Jarman, The spectra of sonoluminescence. *Aust. J. Phys.* **23**, 319 (1970).

46. F. R. Young, Sonoluminescence from water containing dissolved gases. *J. Acoust. Soc. Am.* **60**, 169–172 (1976).

47. A. J. Walton, G. T. Reynolds, Sonoluminescence. *Adv. Phys.* **33**, 595–660 (1984).

48. K. S. Suslick, E. B. Flint, Sonoluminescence from non-aqueous liquids. *Nature*. **330**, 553–555 (1987).

49. E. B. Flint, K. S. Suslick, Sonoluminescence from Nonaqueous Liquids: Emission from Small Molecules. *J. Am. Chem. Soc.* **111**, 6987–6992 (1989).

50. W. B. McNamara, Y. T. Didenko, K. S. Suslick, Sonoluminescence temperatures during multi-bubble cavitation. *Nature*. **401**, 772–775 (1999).

51. E. B. Flint, K. S. Suslick, The temperature of cavitation. *Science (80-.).* **253**,

1397–1399 (1991).

52. W. B. McNamara, Y. T. Didenko, K. S. Suslick, Pressure during Sonoluminescence. *J. Phys. Chem. B.* **107**, 7303–7306 (2003).

53. K. S. Suslick, D. A. Hammerton, R. E. Cline, Sonochemical hot spot. *J. Am. Chem. Soc.* **108**, 5641–5642 (1986).

54. D. J. Flannigan, K. S. Suslick, Emission from electronically excited metal atoms during single-bubble sonoluminescence. *Phys. Rev. Lett.* **99** (2007), doi:10.1103/PhysRevLett.99.134301.

55. V. Kamath, A. Prosperetti, F. N. Egolfopoulos, A theoretical study of sonoluminescence. *J. Acoust. Soc. Am.* **94**, 248–260 (1993).

56. A. Tauber, G. Mark, H. P. Schuchmann, C. Von Sonntag, Sonolysis of tert-butyl alcohol in aqueous solution. *J. Chem. Soc. Perkin Trans. 2*, 1129–1135 (1999).

57. E. J. Hart, C. H. Fischer, A. Henglein, Sonolysis of hydrocarbons in aqueous solution. *Int. J. Radiat. Appl. Instrumentation. Part*. **36**, 511–516 (1990).

58. R. Tourin, Spectroscopic gas temperature measurement: pyrometry of hot gases and plasmas (1966).

59. K. S. Suslick, S. B. Choe, A. A. Cichowlas, M. W. Grinstaff, Sonochemical synthesis of amorphous iron. *Nature*. **353**, 414–416 (1991).

60. K. S. Suslick, E. B. Flint, M. W. Grinstaff, K. A. Kemper, Sonoluminescence from metal carbonyls. *J. Phys. Chem.* **97**, 3098–3099 (1993).

61. S. Y. Ch'en, M. Takeo, Broadening and shift of spectral lines due to the presence of foreign gases. *Rev. Mod. Phys.* **29**, 20–73 (1957).

62. N. Allard, J. Kielkopf, The effect of neutral nonresonant collisions on atomic spectral lines. *Rev. Mod. Phys.* **54**, 1103–1182 (1982).

63. H. Griem, *Principles of Plasma Spectroscopy* (Cambridge University Press, New York, 1997; https://ci.nii.ac.jp/naid/10004635866/).

64. D. F. Gaitan, L. A. Crum, C. C. Church, R. A. Roy, Sonoluminescence and bubble dynamics for a single, stable, cavitation bubble. *J. Acoust. Soc. Am.* **91**, 3166–3183 (1992).

65. R. Hiller, S. J. Putterman, B. P. Barber, Spectrum of synchronous picosecond sonoluminescence. *Phys. Rev. Lett.* **69**, 1182 (1992).

66. R. Hiller, K. Weninger, S. J. Putterman, B. P. Barber, Effect of noble gas doping in single-bubble sonoluminescence. *Science*. **266**, 248–250 (1994).

67. Y. T. Didenko, W. B. McNamara III, K. S. Suslick, Molecular emission from single-bubble sonoluminescence. *Nature*. **407**, 877–879 (2000).

68. D. J. Flannigan, K. S. Suslick, Plasma formation and temperature measurement during single-bubble cavitation. *Nature*. **434**, 52–55 (2005).

69. L. Crum, G. T. Reynolds, Sonoluminescence produced by "stable" cavitation. *J. Acoust. Soc. Am.* **78**, 137–139 (1985).

70. D. F. Gaitan, thesis, University of Mississippi (1990).

71. B. P. Barber, R. Hiller, K. Arisaka, H. Fetterman, S. Putterman, Resolving the picosecond characteristics of synchronous sonoluminescence. *J. Acoust. Soc. Am.* **91**, 3061–3063 (1992).

72. V. Q. Vuong, A. J. Szeri, D. A. Young, Shock formation within

sonoluminescence bubbles. *Phys. Fluids*. **11**, 10–17 (1999).

73. V. Q. Vuong, A. J. Szeri, Sonoluminescence and diffusive transport. *Phys. Fluids*. **8**, 2354–2364 (1996).

74. C. C. Wu, P. H. Roberts, A model of sonoluminescence. *Proc. R. Soc. A Math. Phys. Eng. Sci.* **445**, 323–349 (1994).

75. B. D. Storey, A. J. Szeri, Water vapour, sonoluminescence and sono chemistry. *Proc. R. Soc. A Math. Phys. Eng. Sci.* **456**, 1685–1709 (2000).

76. J. B. Young, J. A. Nelson, W. Kang, Line emission in single-bubble sonoluminescence. *Phys. Rev. Lett.* **86**, 2673 (2001).

77. D. Hammer, L. Frommhold, Spectra of sonoluminescent rare-gas bubbles. *Phys. Rev. Lett.* **85**, 1326–1329 (2000).

78. G. Vazquez, C. Camara, S. Putterman, K. Weninger, Sonoluminescence: nature's smallest blackbody. *Opt. Lett.* **26**, 575–577 (2001).

79. S. Hilgenfeldt, S. Grossmann, D. Lohse, A simple explanation of light emission in sonoluminescence. *Nature*. **398**, 402–405 (1999).

80. Y. T. Didenko, T. V Gordeychuk, Multibubble sonoluminescence spectra of water which resemble single-bubble sonoluminescence. *Phys. Rev. Lett.* **84**, 5640 (2000).

81. K. R. Weninger, H. Cho, R. A. Hiller, S. J. Putterman, G. A. Williams, Sonoluminescence from an isolated bubble on a solid surface. *Phys. Rev. E*. **56**, 6745–6749 (1997).

82. A. Chakravarty, T. Georghiou, T. E. Phillipson, A. J. Walton, Stable

sonoluminescence within a water hammer tube. *Phys. Rev. E*. **69**, 8 (2004).

83. D. J. Flannigan, K. S. Suslick, Molecular and atomic emission during single-bubble cavitation in concentrated sulfuric acid. *Acoust.Res.Lett.Online*. **6**, 157–161 (2005).

84. W. C. Moss, D. B. Clarke, D. A. Young, Calculated pulse widths and spectra of a single sonoluminescing bubble. *Science (80-.).* **276**, 1398–1401 (1997).

85. D. W. Jones, W. L. Wiese, L. A. Woltz, Ion broadening of Ar i lines in a plasma. *Phys. Rev. A.* **34**, 450–456 (1986).

86. D. W. Jones, W. L. Wiese, Asymmetry patterns of plasma-broadened isolated lines (Cr). *Phys. Rev. A.* **30**, 2602–2608 (1984).

87. M. S. Plesset, A. Prosperetti, Bubble dynamics and cavitation. *Annu. Rev. Fluid Mech.* **9**, 145–185 (1977).

88. A. Prosperetti, in *Sonochemistry and Sonoluminescence* (Springer Netherlands, 1999), pp. 39–62.

89. A. Prosperetti, Y. Hao, Modelling of spherical gas bubble oscillations and sonoluminescence. *Philos. Trans. R. Soc. A Math. Phys. Eng. Sci.* **357**, 203–223 (1999).

90. J. B. Keller, M. Miksis, Bubble oscillations of large amplitude. *J. Acoust. Soc. Am.* **68**, 628–633 (1980).

91. J. B. Keller, I. I. Kolodner, Damping of underwater explosion bubble oscillations. *J. Appl. Phys.* **27**, 1152–1161 (1956).

92. C. Herring, *Theory of the pulsations of the gas bubble produced by an underwater*

explosion (Columbia Univ. Div. of National Defense Research, New London Conn., 1941).

93. L. Trilling, The collapse and rebound of a gas bubble. *J. Appl. Phys.* **23**, 14–17 (1952).

94. G. J. Lastman, R. A. Wentzell, On two equations of radial motion of a spherical gas-filled bubble in a compressible liquid. *J. Acoust. Soc. Am.* **71**, 835–838 (1982).

95. G. J. Lastman, R. A. Wentzell, Comparison of five models of spherical bubble response in an inviscid compressible liquid. *J. Acoust. Soc. Am.* **69**, 638–642 (1981).

96. Gompf, Pecha, Mie scattering from a sonoluminescing bubble with high spatial and temporal resolution. *Phys. Rev. E. Stat. Phys. Plasmas. Fluids. Relat. Interdiscip. Topics*. **61**, 5253–6 (2000).

97. R. Löfstedt, K. Weninger, S. Putterman, B. P. Barber, Sonoluminescing bubbles and mass diffusion. *Phys. Rev. E*. **51**, 4400–4410 (1995).

98. B. P. Barber, R. A. Hiller, R. Löfstedt, S. J. Putterman, K. R. Weninger, Defining the unknowns of sonoluminescence. *Phys. Rep.* **281** (1997), pp. 65–143.

99. W. C. Moss, D. B. Clarke, J. W. White, D. A. Young, Hydrodynamic simulations of bubble collapse and picosecond sonoluminescence. *Phys. Fluids*. **6**, 2979–2985 (1994).

100. C. C. Wu, P. H. Roberts, Shock-wave propagation in a sonoluminescing gas bubble. *Phys. Rev. Lett.* **70**, 3424–3427 (1993).

101. H. P. Greenspan, A. Nadim, On sonoluminescence of an oscillating gas bubble. *Phys. Fluids A.* **5**, 1065–1067 (1992).

102. C. D. Ohl, O. Lindau, W. Lauterborn, Luminescence from Spherically and Aspherically Collapsing Laser Induced Bubbles. *Phys. Rev. Lett.* **80**, 393–396 (1998).

103. C. D. Ohl, Luminescence from acoustic-driven laser-induced cavitation bubbles. *Phys. Rev. E - Stat. Physics, Plasmas, Fluids, Relat. Interdiscip. Top.* **61**, 1497–1500 (2000).

104. O. Baghdassarian, B. Tabbert, G. A. Williams, Luminescence characteristics of laser-induced bubbles in water. *Phys. Rev. Lett.* **83**, 2437 (1999).

105. O. Baghdassarian, H. C. Chu, B. Tabbert, G. A. Williams, Spectrum of luminescence from laser-created bubbles in water. *Phys. Rev. Lett.* **86**, 4934–4937 (2001).

106. K. Yasui, Alternative model of single-bubble sonoluminescence. *Phys. Rev. E - Stat. Physics, Plasmas, Fluids, Relat. Interdiscip. Top.* **56**, 6750–6760 (1997).

107. C. Gong, D. P. Hart, in *American Society of Mechanical Engineers, Fluids Engineering Division (Publication) FED* (ASME, 1997), vol. 4.

108. B. D. Storey, A. J. Szeri, in *Proceedings of the Royal Society of London A: Mathematical, Physical and Engineering Sciences* (The Royal Society, 2000), vol. 456, pp. 1685–1709.

109. W. C. Moss *et al.*, Computed optical emissions from a sonoluminescing bubble. *Phys. Rev. E*. **59**, 2986 (1999).

110. V. P. (Van P. . Carey, *Liquid-vapor phase-change phenomena equipment* (Hemisphere, Washington, D.C., 1 st., 1992).

111. I. W. Eames, N. J. Marr, H. Sabir, The evaporation coefficient of water: A review. *Int. J. Heat Mass Transf.* **40**, 2963–2973 (1997).

112. U. Maas, J. Warnatz, Ignition processes in hydrogenoxygen mixtures. *Combust. Flame*. **74**, 53–69 (1988).

113. W. C. Gardiner, in *Combustion Chemistry* (Springer New York, 1984), pp. 1–19.

114. R. Löfstedt, B. P. Barber, S. J. Putterman, Toward a hydrodynamic theory of sonoluminescence. *Phys. Fluids A.* **5**, 2911–2928 (1992).

115. B. P. Barber, R. A. Hiller, R. Löfstedt, S. J. Putterman, K. R. Weninger, Defining the unknowns of sonoluminescence. *Phys. Rep.* **281** (1997), pp. 65–143.

116. A. Prosperetti, Thermal effects and damping mechanisms in the forced radial oscillations of gas bubbles in liquids. *J. Acoust. Soc. Am.* **61**, 17–27 (1977).

117. S. Hilgenfeldt, S. Grossmann, D. Lohse, Sonoluminescence light emission. *Phys. Fluids*. **11**, 1318–1330 (1999).

118. R. Toegel, B. Gompf, R. Pecha, D. Lohse, Does Water Vapor Prevent Upscaling Sonoluminescence? *Phys. Rev. Lett.* **85**, 3165–3168 (2000).

119. R. Toegel, S. Hilgenfeldt, D. Lohse, Suppressing Dissociation in Sonoluminescing Bubbles: The Effect of Excluded Volume. *Phys. Rev. Lett.* **88**, 4 (2002).

120. B. D. Storey, A. J. Szeri, A reduced model of cavitation physics for use in sonochemistry. *Proc. R. Soc. A Math. Phys. Eng. Sci.* **457**, 1685–1700 (2001).

121. T. K. Saksena, W. L. Nyborg, Sonoluminescence from stable cavitation. *J. Chem. Phys.* **53**, 1722–1734 (1970).

122. L. Frommhold, A. A. Atchley, Is sonoluminescence due to collision-induced emission? *Phys. Rev. Lett.* **73**, 2883–2886 (1994).

123. D. Hammer, L. Frommhold, Sonoluminescence: How bubbles glow. *J. Mod. Opt.* **48** (2001), pp. 239–277.

124. L. S. Bernstein, M. R. Zakin, Confined electron model for single-bubble sonoluminescence. *J. Phys. Chem.* **99**, 14619–14627 (1995).

125. B. Gompf, R. Günther, G. Nick, R. Pecha, W. Eisenmenger, Resolving sonoluminescence pulse width with time-correlated single photon counting. *Phys. Rev. Lett.* **79**, 1405 (1997).

126. R. A. Hiller, S. J. Putterman, K. R. Weninger, Time-Resolved Spectra of Sonoluminescence. *Phys. Rev. Lett.* **80**, 1090–1093 (1998).

127. M. J. Moran, D. Sweider, Measurements of Sonoluminescence Temporal Pulse Shape. *Phys. Rev. Lett.* **80**, 4987–4990 (1998).

128. A. Buzukov, V. T.-J. Lett, undefined 1971, Sonoluminescence following focusing of laser radiation into a liquid. *jetpletters.ac.ru* (available at http://www.jetpletters.ac.ru/ps/1628/article_24883.pdf).

129. O. Baghdassarian, B. Tabbert, G. A. Williams, Luminescence from laser-created bubbles in cryogenic liquids. *Phys. B Condens. Matter*. **284**–**288**, 393–394 (2000).

130. O. Baghdassarian, B. Tabbert, G. A. Williams, Luminescence from laser-created bubbles in cryogenic liquids. *Phys. Rev. E - Stat. Nonlinear, Soft Matter Phys.* **75**,

066305 (2007).

131. E. A. Brujan, D. S. Hecht, F. Lee, G. A. Williams, Properties of luminescence from laser-created bubbles in pressurized water. *Phys. Rev. E - Stat. Nonlinear, Soft Matter Phys.* **72**, 066310 (2005).

132. E. A. Brujan, G. A. Williams, Luminescence spectra of laser-induced cavitation bubbles near rigid boundaries. *Phys. Rev. E - Stat. Nonlinear, Soft Matter Phys.* **72**, 016304 (2005).

133. E. M. Englert, A. McCarn, G. A. Williams, Luminescence from laser-induced bubbles in water-glycerol mixtures: Effect of viscosity. *Phys. Rev. E - Stat. Nonlinear, Soft Matter Phys.* **83**, 046306 (2011).

134. H. C. Chu, S. Vo, G. A. Williams, Precursor luminescence near the collapse of laser-induced bubbles in alkali-salt solutions. *Phys. Rev. Lett.* **102**, 204301 (2009).

135. O. Supponen, D. Obreschkow, P. Kobel, M. Farhat, Luminescence from cavitation bubbles deformed in uniform pressure gradients. *Phys. Rev. E*. **96**, 033114 (2017).

136. C. H. M. Jenkins, *Bio-inspired engineering* (Momentum Press, 2011).

137. S. A. Velcro, Improvements in or relating to a method and a device for producing a velvet type fabric. *Swiss Pat.* (1955).

138. M. G. De, Velvet type fabric and method of producing same (1955).

139. S. N. Patek, W. L. Korff, R. L. Caldwell, Biomechanics: deadly strike mechanism of a mantis shrimp. *Nature*. **428**, 819–820 (2004).

140. S. N. Patek, R. L. Caldwell, Extreme impact and cavitation forces of a biological

hammer: strike forces of the peacock mantis shrimp Odontodactylus scyllarus. *J. Exp. Biol.* **208**, 3655–3664 (2005).

141. F. A. Everest, R. W. Young, M. W. Johnson, Acoustical characteristics of noise produced by snapping shrimp. *J. Acoust. Soc. Am.* **20**, 137–142 (1948).

142. J. Herberholz, B. Schmitz, Signaling via water currents in behavioral interactions of snapping shrimp (Alpheus heterochaelis). *Biol. Bull.* **201**, 6–16 (2001).

143. P. Xiao, D. Staack, Microbubble generation by microplasma in water. *J. Phys. D. Appl. Phys.* **47**, 355203 (2014).

144. J. A. Cook, A. M. Gleeson, R. M. Roberts, R. L. Rogers, A spark-generated bubble model with semi-empirical mass transport. *J. Acoust. Soc. Am.* **101**, 1908–1920 (1997).

145. S. Buogo, G. B. Cannelli, Implosion of an underwater spark-generated bubble and acoustic energy evaluation using the Rayleigh model. *J. Acoust. Soc. Am.* **111**, 2594–2600 (2002).

146. V. Lazic, J. J. Laserna, S. Jovicevic, Insights in the laser-induced breakdown spectroscopy signal generation underwater using dual pulse excitation—Part I: Vapor bubble, shockwaves and plasma. *Spectrochim. Acta Part B At. Spectrosc.* **82**, 42–49 (2013).

147. V. Lazic, J. J. Laserna, S. Jovicevic, Insights in the laser induced breakdown spectroscopy signal generation underwater using dual pulse excitation—Part II: Plasma emission intensity as a function of interpulse delay. *Spectrochim. Acta Part B At. Spectrosc.* **82**, 50–59 (2013).

148. D. Hess, C. Brücker, F. Hegner, A. Balmert, H. Bleckmann, Vortex formation with a snapping shrimp claw. *PLoS One*. **8**, e77120 (2013).

149. S. M. Cox, D. Schmidt, Y. Modarres-Sadeghi, S. N. Patek, A physical model of the extreme mantis shrimp strike: kinematics and cavitation of Ninjabot. *Bioinspir. Biomim.* **9**, 16014 (2014).

150. A. Anker, S. T. Ahyong, P. Y. Noël, A. R. Palmer, Morphological phylogeny of alpheid shrimps: parallel preadaptation and the origin of a key morphological innovation, the snapping claw. *Evolution (N. Y).* **60**, 2507–2528 (2006).

151. A. Anker, C. Hurt, N. Knowlton, Revision of the Alpheus formosus Gibbes, 1850 complex, with redescription of A. formosus and description of a new species from the tropical western Atlantic (Crustacea: Decapoda: Alpheidae). *Zootaxa*. **1707**, 1–22 (2008).

152. P. Cignoni *et al.*, in *Eurographics Italian Chapter Conference*, V. Scarano, R. De Chiara, U. Erra, Eds. (The Eurographics Association, 2008).

153. M. Corsini, P. Cignoni, R. Scopigno, Efficient and flexible sampling with blue noise properties of triangular meshes. *IEEE Trans. Vis. Comput. Graph.* **18**, 914–924 (2012).

154. P. Alam *et al.*, The snapping shrimp dactyl plunger: a thermomechanical damage-tolerant sandwich composite. *Zoology*. **126**, 1–10 (2018).

155. H. Lamb, *Hydrodynamics* (Cambridge University Press, 1932).

156. P. R. N. Childs, *Rotating flow* (Elsevier, 2010).

157. S. F. Hoerner, *Fluid-dynamic drag: practical information on aerodynamic drag*

and hydrodynamic resistance (Hoerner Fluid Dynamics Midland Park, NJ, 1965).

158. D. of W. R. University of California, “Underwater noise caused by snapping shrimp” (San Diego, 1946), (available at https://escholarship.org/uc/item/30z3x42w).

159. G. K. Taylor, R. L. Nudds, A. L. R. Thomas, Flying and swimming animals cruise at a Strouhal number tuned for high power efficiency. *Nature*. **425**, 707–711 (2003).

160. O. Supponen *et al.*, Shock waves from non-spherical cavitation bubbles (2017), doi:10.1103/PhysRevFluids.2.093601.

161. S. J. Kline, F. A. McClintock, Describing uncertainties in single-sample experiments. *Mech. Eng.* **75**, 3–8 (1953).

162. R. J. Moffat, Describing the uncertainties in experimental results. *Exp. Therm. Fluid Sci.* **1**, 3–17 (1988).

163. D. H. Cato, M. J. Bell, Ultrasonic ambient noise in Australian shallow waters at frequencies up to 200 kHz (1992), p. No. MRL-TR-91-23.

164. G. S. Settles, *Schlieren and shadowgraph techniques: visualizing phenomena in transparent media* (Springer Science & Business Media, ed. 1., 2012).

165. C. Darwin, *On the origin of species by means of natural selection. 1859* (1968).

166. D. Obreschkow *et al.*, Cavitation bubble dynamics inside liquid drops in microgravity. *Phys. Rev. Lett.* **97**, 94502 (2006).

167. M. Tinguely *et al.*, Energy partition at the collapse of spherical cavitation bubbles. *Phys. Rev. E*. **86**, 46315 (2012).

168. B. P. Barber, thesis (1992).

169. W. Lauterborn, H. Bolle, Experimental investigations of cavitation-bubble collapse in the neighbourhood of a solid boundary. *J. Fluid Mech.* **72**, 391–399 (1975).

170. W. Lauterborn, C.-D. Ohl, Cavitation bubble dynamics. *Ultrason. Sonochem.* **4**, 65–75 (1997).

171. I. Akhatov *et al.*, Collapse and rebound of a laser-induced cavitation bubble. *Phys. Fluids*. **13**, 2805–2819 (2001).

172. E.-A. Brujan, K. Nahen, P. Schmidt, A. Vogel, Dynamics of laser-induced cavitation bubbles near an elastic boundary. *J. Fluid Mech.* **433**, 251–281 (2001).

173. C. Jenkins, *Bio-Inspired Engineering* (2011).

174. N. R. Council, *Plasma science: Advancing knowledge in the national interest* (National Academies Press, 2008).

175. W. W. Hsing, N. M. Hoffman, Measurement of feedthrough and instability growth in radiation-driven cylindrical implosions. *Phys. Rev. Lett.* **78**, 3876–3879 (1997).

176. E. Chang, L. Y. Matloff, A. K. Stowers, D. Lentink, Soft biohybrid morphing wings with feathers underactuated by wrist and finger motion. *Sci. Robot.* **5**, eaay1246 (2020).

177. S. Amini, M. Tadayon, J. Q. I. Chua, A. Miserez, Multi-scale structural design and biomechanics of the pistol shrimp snapper claw. *Acta Biomater.* **73**, 449–457 (2018).

178. Z. Qian *et al.*, Structure, mechanical properties and surface morphology of the snapping shrimp claw. *J. Mater. Sci.* **53**, 10666–10678 (2018).

APPENDIX A

EFFICIENCY OF OTHER OPTICAL COMPONENTS

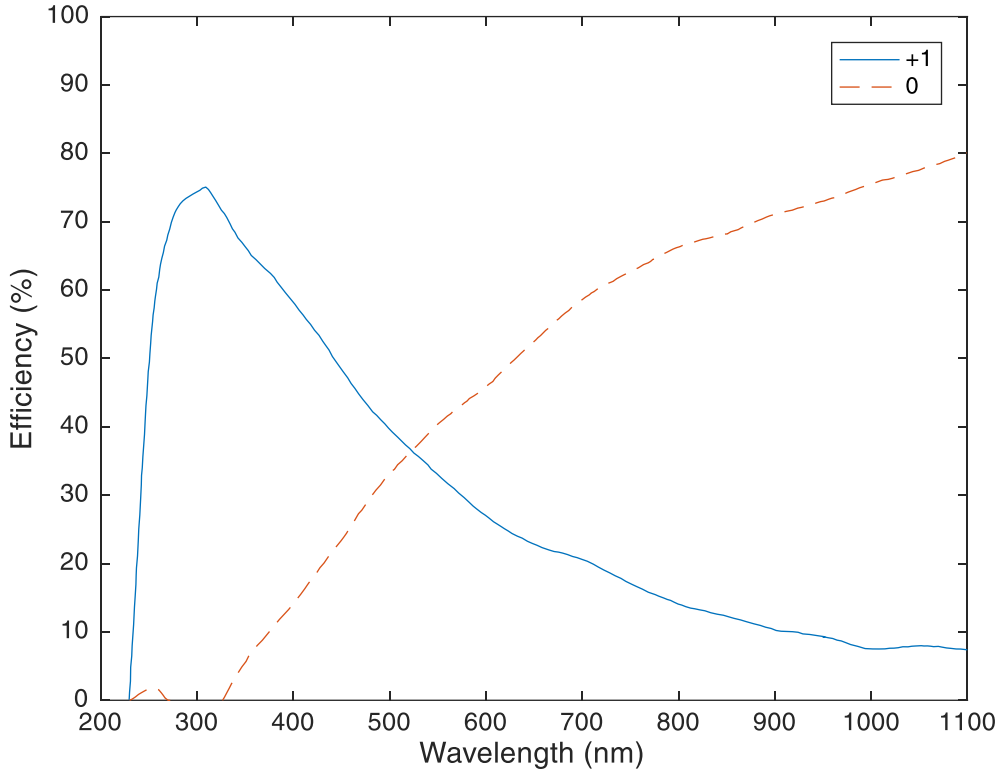

Figure 85 UV transmission grating efficiency.
Edmund Optics #85291 300/8.6 degree.

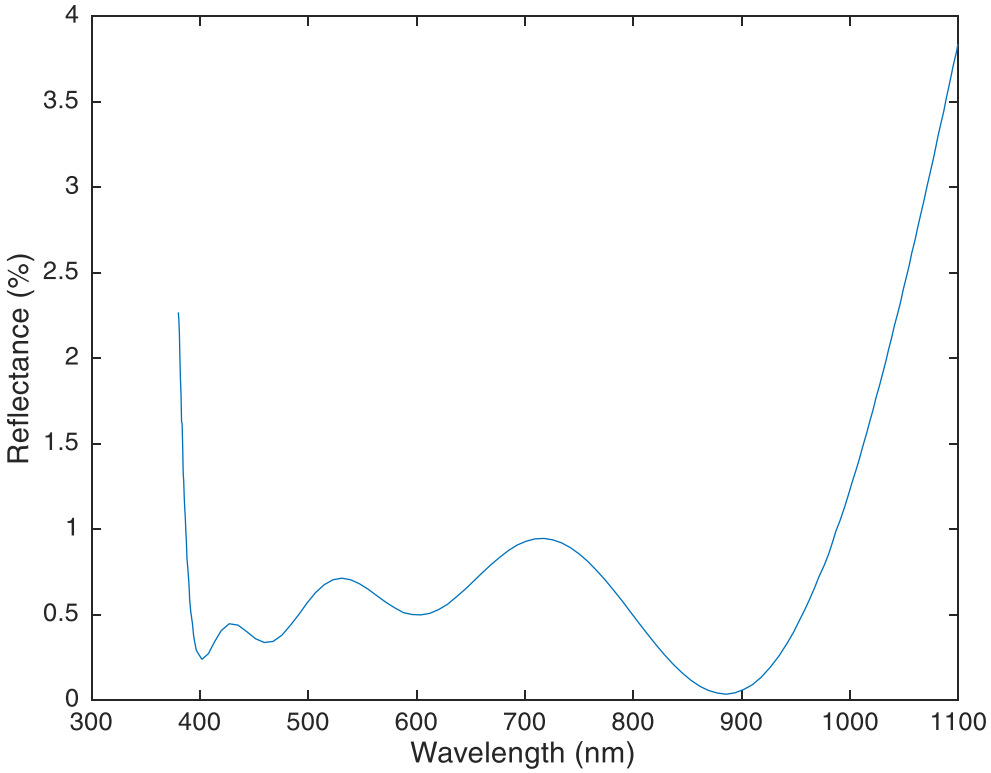

Figure 86 Edmund Optics Achromatic lens VIS-NIR [400-1000nm] anti-reflection Coating performance.

APPENDIX B

MATLAB CODE FOR CAVITATION LUMINESCENCE IMAGE PROCESSING

```
close all
clear all
clc
%%
background_subtract = 1; % 0 -> no, 1-> yes
%% Background average
cd('D:\Bionic Device Video\ICCD and hydro\background...
images\0923_1st_exposure 100');
addpath(genpath('D:\Mathworks\ICCD'));
fn = dir('*.tif');
b = {fn.name};
num = length(b);
% num = 41;ima
B_3D(:,:,1) = double(imread(b{1}));
B_3D_old(:,:,1) = double(imread(b{1}));
% B_avg = double(imread(b{1}));
B_std = double(imread(b{1}));
B_3Dmax = zeros(num,1);
B_3D_sub_min = zeros(num,1);
B_3Dmean = zeros(num,1);
B_3Dstd = zeros(num,1);
% Read in all background image and merge them into one 3D matrix,
convert integer to double
for i = 1:num
    B_3D(:,:,i) = double(imread(b{i}));
    B_3D_old(:,:,i) = double(imread(b{i}));
end

B_3D_old_avg = mean(B_3D_old,3);
L = size(B_3D,1);
H = size(B_3D,2);
pixx = [1:H];
pixy = [1:L];
[pixxm,pixym] = meshgrid(pixx,pixy);

% Choose the largest std value among overall image std, row vector std
and column vector std;
n = 3; % number of times of std value n*sigma
bad_max =
[mean2(B_3D_old_avg)+n*std2(B_3D_old_avg),max(mean(B_3D_old_avg)+n*std(
B_3D_old_avg)),max(mean(B_3D_old_avg')+n*std(B_3D_old_avg'))];

% Bad pixel of B_3D_old_avg, as reference of A_sub
[Xb,Yb] = find(B_3D_old_avg>= max(bad_max));

% Bad pixel of each background image B_3D_old(:,:,i)
for i = 1:num
    % get the location of bad pixels on each BG images
```

```
    [Xb_BG,Yb_BG] = find(B_3D_old(:,:,i)>= max(bad_max));
    bad_pixel_intensity = zeros(size(Xb_BG,1),1);
    for j = 1:size(Xb_BG,1)
    bad_pixel_intensity(j) = B_3D_old_avg(Xb_BG(j),Yb_BG(j));
    end
    % substitute the bad pixel with 0
    for ib = 1:size(Xb_BG,1)
        for jb = 1:size(Yb_BG,1)
            B_3D(Xb_BG(ib),Yb_BG(jb),i)= 0;
        end
    end
end
% % show intensity values of bad pixels in B_3D_old_avg

for i = 1:size(Xb,1)
    bad_pixel_intensity(i) = B_3D_old_avg(Xb(i),Yb(i));
end

DoBGStuff = 1;
if DoBGStuff


for i = 1:num
    B_3Dmax(i) = max(max(B_3D(:,:,i)));
    B_3Dmean(i) = mean2(B_3D(:,:,i));
    B_3Dstd(i) = std2(B_3D(:,:,i));
end

    save BGStuff_without_bad_pixel.mat
else
    load BGStuff_without_bad_pixel.mat
end

% Average of each location for all background image
B_3D_avg = mean(B_3D,3);

% Standard deviation of each location for all background image
B_3D_std = std(B_3D,0,3);

% Background image subtract average background, set the overall
background noise level to 0
B_3D_sub(:,:,1) = B_3D_avg;
B_3D_sub_mean = zeros(num,1);
for i=1:num
    B_3D_sub(:,:,i) = B_3D(:,:,i) - B_3D_avg;
    B_3D_sub_min(i) = min(min(B_3D_sub(:,:,i)));
    B_3D_sub_max(i) = max(max(B_3D_sub(:,:,i)));
    B_3D_sub_mean(i) = mean2(B_3D_sub(:,:,i));
end
% Average (Background) of each location for all background image after
BC subtract
B_3D_sub_avg = mean(B_3D_sub,3);
```

```
B_3D_sub_std = std(B_3D_sub,0,3);
TH = 9*mean(mean(B_3D_std)); % 9 sigma threshold for light emission
for i=1:num
    B_SS(i) = sum(sum(B_3D_sub(:,:,i)));
    B_SS2(i) = sum(sum(B_3D_sub(:,:,i).*(B_3D_sub(:,:,i)>TH)));
    B_xm(i) =
sum(sum(B_3D_sub(:,:,i).*(B_3D_sub(:,:,i)>TH).*pixxm))/B_SS2(i);
    B_ym(i) =
sum(sum(B_3D_sub(:,:,i).*(B_3D_sub(:,:,i)>TH).*pixym))/B_SS2(i);
    B_xm2(i) = pixxm(find(B_3D_sub(:,:,i)==B_3D_sub_max(i)));
    B_ym2(i) = pixym(find(B_3D_sub(:,:,i)==B_3D_sub_max(i)));
end

% Background image average
imagesc(B_3D_avg),colormap(gray);
colorbar;
title('Background Average without bad pixels')
xlabel('X (pixels)');
ylabel('Y (pixels)');

%%
cd('D:\Bionic Device Video\ICCD and hydro\ICCD_image\160923\Air near
singularity')
a = dir('16_09_23_air_ICCD_expo100_delay880_gain1000_*.tif');
c = {a.name};
Intensity_max = zeros(1,length(c));
Intensity_AvgBright = zeros(1,length(c));
% threshold = 200;
% Initialize arrary for storing number of pixels above threshold
pixel_num = zeros(length(c),1);
%% Case 1 only_statistic
for k = 1 : length(c)
    if background_subtract
        A = imread(c{k});
        A_sub = double(A) - double(B_3D_avg);
        % set world coordinates
        xWorldLimits = [5.6417 34.0046];
        yWorldLimits = [-15.1078 5.7472];
        RA = imref2d(size(A_sub),xWorldLimits,yWorldLimits);
        for ib = 1:size(Xb,1)
            for jb = 1:size(Yb,1)
                A_sub(Xb(ib),Yb(jb))= 0;
            end
        end
        [X,Y] = find(A_sub(:,:)>= TH);
        Intensity_AvgBright(k)= mean(A_sub(A_sub(:,:)>= threshold)); %
Average intensity for A_sub pixels above threshold
        pixel_num(k) = size(X,1);
        Intensity_max(k) = max(max(A_sub));
        A_SS(k) = sum(sum(A_sub));
        A_SS2(k) = sum(sum(A_sub.*(A_sub>TH)));
        A_xm(k) =
sum(sum(A_sub(:,:).*(A_sub(:,:)>TH).*pixxm))/A_SS2(k);
```

```
        A_ym(k) =
sum(sum(A_sub(:,:).*(A_sub(:,:)>TH).*pixym))/A_SS2(k);
        A_xm2(k) = pixxm(find(A_sub==Intensity_max(k)));
        A_ym2(k) = pixym(find(A_sub==Intensity_max(k)));

% % Comparison of raw images and pixels above threshold logical images
        if pixel_num(k) > 1
%             figure('Position',[300 300 600 400]);
%             figure('Position',[208 467 1086 329])
%             h1 = subplot(1,2,1);
            figure;
%             imagesc(A_sub(:,:,1),[-3*mean2(B_3D_std)
Intensity_max(k)]),colormap(jet);colorbar;
            imshow(flipud(A_sub(:,:,1)),RA,[-3*mean2(B_3D_std)
Intensity_max(k)],'Colormap',jet);colorbar eastoutside;
            axis xy
            set(gca,'box','off');
%             caxis([-3*mean2(B_3D_std),max(Intensity_max)]);
            title(strrep(c{k},'_',' '))
%             xlim([1150 1300])
%             ylim([300 450])
            hold on
%             plot(A_xm2(k),A_ym2(k),'ko')
            daspect([1 1 1])
            xlabel('Horizontal distance (mm)');
            ylabel('Vertical distance (mm)');
            OuterPosition = get(gca,'OuterPosition');
            set(gca,'OuterPosition',[OuterPosition(1)+0.1
OuterPosition(2)+0.1 OuterPosition(3)-0.1 OuterPosition(4)-0.1]);
            %             h2 = subplot(1,2,2);
            %
imagesc(A_sub(:,:,1)>=threshold),colormap(jet);colorbar;
            %             linkaxes([h1 h2])
            %             title(['Number of pixels above threshold,
N=',num2str(pixel_num(k))])
            %             xlabel('X (pixels)');
            %             ylabel('Y (pixels)');
        end
    else
        A = imread(c{k});
        Intensity_max(k) = max(max(A));
    end
end
%% plot the pixel numbers above threshold for all ICCD images
figure;
bar(0:length(c)-1,pixel_num);hold on;
plot([-1 length(c)],[mean(pixel_num) mean(pixel_num)]);
% plot([-1 length(c)],[mean(pixel_num)+std(pixel_num)
mean(pixel_num)+std(pixel_num)]);
% title('Number of pixels above threshold');
legend('Pixel number above threshold for different trials','Average
pixel number above threshold')
xlabel('Trial numbers');
```

```
ylabel('Number of pixels above the intensity threshold');

%% Plot Statistics Intensity_max
uncertainty_pos = mean(Intensity_max) + std(Intensity_max,0);
uncertainty_neg = mean(Intensity_max) - std(Intensity_max,0);
figure;
bar(0:length(c)-1,Intensity_max); %%% if the images start from 0->
0:length(c)-1, if start from 1-> 1:length(c)

hold on
plot([-1 length(c)],[mean(Intensity_max) mean(Intensity_max)]);
plot([-1 length(c)],[uncertainty_pos uncertainty_pos]);
plot([-1 length(c)],[uncertainty_neg uncertainty_neg]);

% title('Maximum intensity for ICCD images')
xlabel('Trial numbers');
ylabel('Intensity (AU)');
legend('Maximum intensity','Imax_{avg} Average maximum
intensity','Imax_{avg} + \sigma','Imax_{avg} - \sigma')
% grid on

% Statistical results on plot

txt1 = ['Average Maximum Intensity = ',num2str(mean(Intensity_max))];
txt2 = ['Std Dev of Max Intensity = ',num2str(std(Intensity_max,0))];
txt3 = ['Average Intensity of Background = ',num2str(mean2(B_3D_avg))];
txt4 = ['Average Standard Deviation of Background =
',num2str(mean(mean(B_3D_std)))];


%% Plot Statistics: Intensity_average for pixels above threshold
Intensity_AvgBright(isnan(Intensity_AvgBright)) = 0 ; % set NaN value
in the vector to 0
uncertainty_pos = mean(Intensity_AvgBright) +
std(Intensity_AvgBright,0);
uncertainty_neg = mean(Intensity_AvgBright) -
std(Intensity_AvgBright,0);
figure;
bar(0:length(c)-1,Intensity_AvgBright); %%% if the images start from 0-
> 0:length(c)-1, if start from 1-> 1:length(c)
hold on
plot([-1 length(c)],[mean(Intensity_AvgBright)
mean(Intensity_AvgBright)]);
plot([-1 length(c)],[uncertainty_pos uncertainty_pos]);
plot([-1 length(c)],[uncertainty_neg uncertainty_neg]);

% title('Maximum intensity for ICCD images')
xlabel('Trial numbers');
ylabel('Intensity (AU)');
legend('Average intensity for pixels above threshold in different
trials','I_{avg} mean of average intensity for pixels above
threshold','I_{avg} + \sigma','I_{avg} - \sigma')
```

```
% grid on

% Statistical results on plot

txt5 = ['Average Intensity for Pixels above Threshold =
',num2str(mean(Intensity_AvgBright))];
txt6 = ['Std Dev of Average Intensity for Pixels above Threshold =
',num2str(std(Intensity_AvgBright,0))];


mTextBox1 = uicontrol('style','text','Position',[200 500 200 40]);
mTextBox2 = uicontrol('style','text','Position',[200 470 200 40]);
% mTextBox3 = uicontrol('style','text','Position',[200 440 220 20]);
% mTextBox4 = uicontrol('style','text','Position',[200 410 280 20]);

set(mTextBox1,'String',txt5,'BackgroundColor',[1 1 1]);
set(mTextBox2,'String',txt6,'BackgroundColor',[1 1 1]);

%% Reference image with cavitation luminescence sites
cd('D:\Bionic Device Video\ICCD and hydro\Reference images\0923 ref');
I = imread('16_09_23_ICCD_expo20_delay800_gain900_ref.tif');

figure;
% imagesc(I);
imshow(flipud(I),RA,[0 4095]);
axis xy
set(gca,'box','off');
% daspect([1 1 1])
hold on

for i=1:length(A_xm2)
    if A_xm2(i) > 1000 && A_ym2(i) < 600
    plot(A_xm2(i)/1360*28.3629+5.6417,(1000-A_ym2(i))/1000*20.855-
15.1078,'rd');
    end
end
hold off
xlabel('Horizontal distance (mm)');
ylabel('Vertical distance (mm)');
OuterPosition = get(gca,'OuterPosition');
set(gca,'OuterPosition',[OuterPosition(1)+0.1 OuterPosition(2)+0.1
OuterPosition(3)-0.1 OuterPosition(4)-0.1]);

% % Get world coordinate on image
A1 = [find(A_xm2 > 1000)];
A2 = [find(A_ym2 < 600)];
A3 = intersect(A1,A2);
A4 = setdiff([find(A_xm2>0)],A3);
N = size(A3,2);
M = size(B_3D,3);
figure;
bins = linspace(-400,900,131);
```

```
histogram(Intensity_AvgBright,bins,'Normalization','probability');
hold on
histogram(B_3D_sub,bins,'Normalization','probability');
xlabel('Average intensity (counts)');
ylabel('Probability');
legend(['Air doping(N=',num2str(N),')'],['Background
(N=',num2str(M),')']);
xlim([-200 800])
ylim([0 0.25])
```